TIME-RESOLVED INTERFEROMETRY ON METALS AND DISORDERED SYSTEMS

Hendrikus Jacobus Kop

Time-resolved interferometry on metals and disordered systems

Time-resolved interferometry on metals and disordered systems

ACADEMISCH PROEFSCHRIFT

ter verkrijging van de graad van doctor
aan de Universiteit van Amsterdam
op gezag van de Rector Magnificus
prof. dr. J. J. M. Franse
ten overstaan van een door het college voor promoties ingestelde
commissie in het openbaar te verdedigen in de aula der Universiteit
op dinsdag 20 oktober 1998 te 11.00 uur

door

Hendrikus Jacobus Kop

geboren te Amsterdam

Amsterdam 1998

Promotor :	Prof. Dr. A. Lagendijk
Co-Promotor :	Dr. R. Sprik

Commissie :	Prof. Dr. G. 't Hooft
	Prof. Dr. A.W. Kleijn
	Dr. L.G. Suttorp
	Prof. Dr. H.B. van Linden van den Heuvell
	Prof. Dr. F.R. deBoer

Paranimfen :	Peter Kop
	Huub Kop

Faculteit Wiskunde, Informatica, Natuurkunde en Sterrenkunde (WINS)

The work described in this thesis has been supported by the
"Stichting voor Fundamenteel Onderzoek der Materie (FOM)",
which is financially supported by the
"Nederlandse Organisatie voor Wetenschappelijk Onderzoek (NWO)"
and was carried out at the

Van der Waals-Zeeman Instituut
Universiteit van Amsterdam
Valckenierstraat 65
1018 XE Amsterdam
The Netherlands

where a limited number of copies of this thesis are available.

Ontwerp omslag: Ronny Samuel

ISBN 90-74795-99-4

Contents

Chapter 1

Introduction

1.1 Spectroscopy

Spectroscopy is the term describing the study of spectra, spectrometry is the quantitative measurement of the form of a spectrum. Strictly speaking, spectroscopy implies the visual observation of a spectrum but the term is so widely understood in the more general sense to describe the subject as a whole, that it will be used with that meaning here. Generally, one speaks about spectroscopy if a study is performed in the frequency domain. However, it is also possible to perform spectroscopy in the time domain. In that case the measurements and analysis are performed in the time domain and one refers to that subject as time-resolved spectroscopy. In general, time and frequency measurements provide the same information and are connected by employing a Fourier transformation.

1.2 Fourier transform spectroscopy

The quantitative investigation of spectra involves the determination of precise information about the energies at which systems absorb or emit electromagnetic radiation. To be able to perform such an quantitative investigation it is possible to use a number of well-established techniques, like there is for instance the method of Fourier transform spectroscopy. In this technique one roughly divides a beam of radiation from a into two parts, introduce a variable path length of one beam relative to the other and then detect the resultant power when the two beams are recombined. This signal is recorded as function of delay and shows fluctuations that are basically periodic as function of the

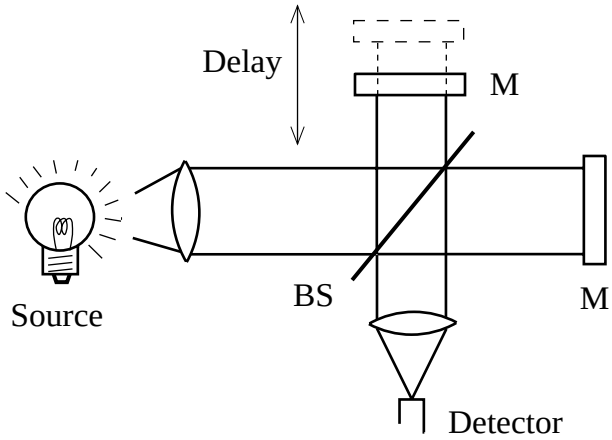

Figure 1.1: *The two-beam Michelson interferometer. BS: beam splitter, M: Mirror*

optical path-length difference. The instrument to perform such a measurement is called an interferometer.

The first interferometer to be applied to perform spectral analysis was the two-beam instrument that Michelson invented in 1882 and which now bears his name [1]-[3]. The interferometer used by Michelson is shown schematically in Fig.1.1. The phase delay between the two beams, is achieved in practice by dividing the incident radiation, with a beam splitter (BS) and then reflecting the two partial beams from the mirrors (indicated with M) back to the beam splitter where they recombine and proceed to the detector. Michelson showed, employing this apparatus, the presence of splitting in many interesting spectral lines that were too narrow to analyze by conventional prism or grating spectrometers. For instance, he showed that the red Balmer line of hydrogen is a doublet.

Michelson performed his measurements by observing the spatially displayed fringes obtained with an extended source. In the modern form of Michelson's method, Fourier transform spectroscopy, a detector is employed to record the intensity, as indicated in Fig. 1.1. Lets consider a Michelson interferometer which is ideal, meaning that it is lossless and that the intensity coming from both arms is equal. Suppose now that the spectral distribution of the source illuminating the Michelson interfrometer emits a spectral distribution $|B(k)|^2 dk$ in the wavenumber range k to $k + dk$. We assume that this spectral distribution is strongly peaked spectrum around a central wavenumber k_0. The interferometer introduces a path difference ΔL between the beams, so the phase difference is: $2\pi\Delta L/\lambda = k\Delta L$. The resultant intensity of the light

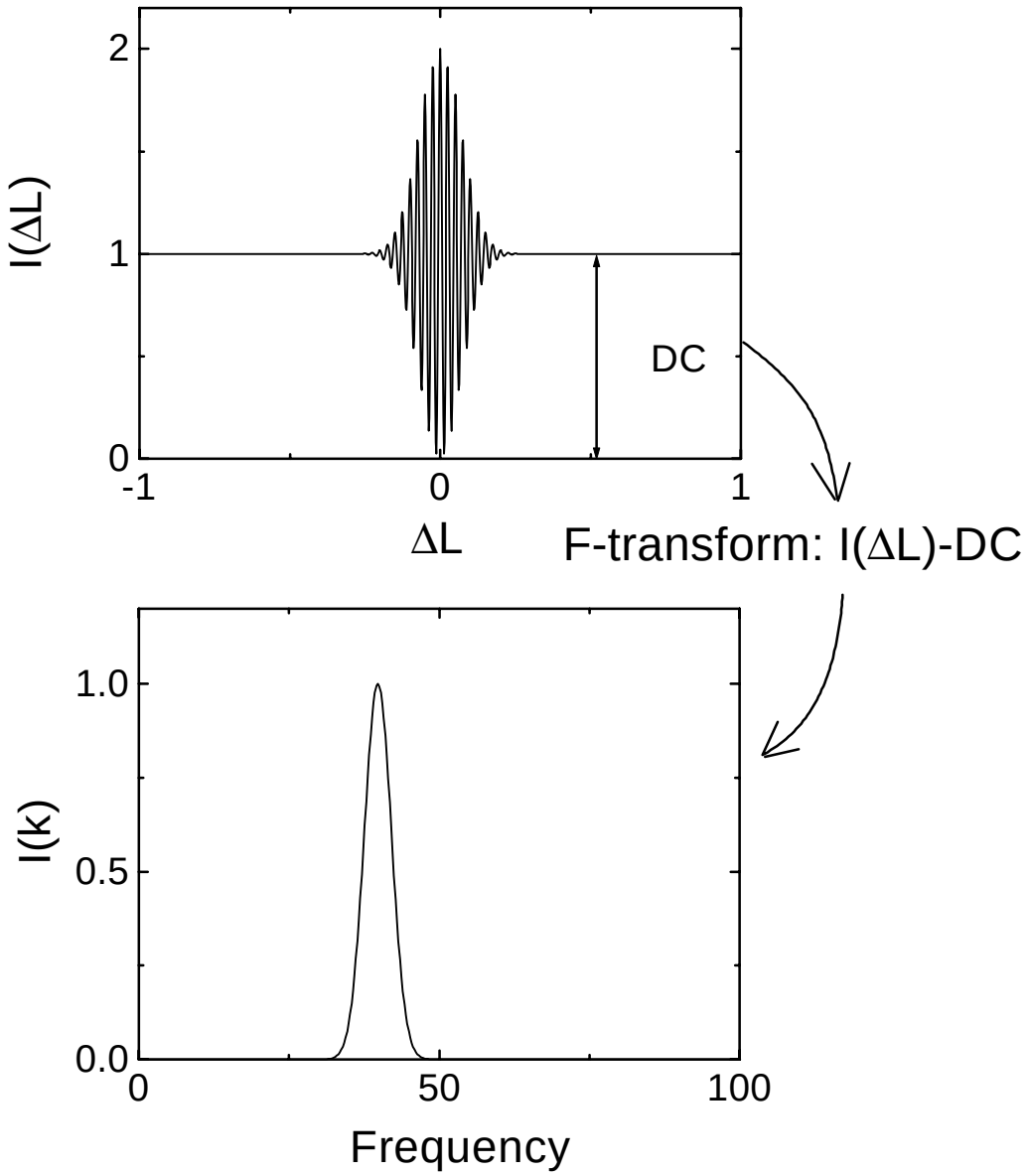

Figure 1.2: *Schematic representation (top figure) of the interference function (1.1), which would be produced by a Michelson interferometer Interferometer-Michelson Interferometer illuminated by the simple Gaussian spectrum shown at the bottom of this picture. The constant term in Eq. (1.1) is indicated with DC in this picture. The interferogram can be obtained from such a measurement by subtracting this DC level. After Fourier transforming the interferogram we obtain the spectrum of the source.*

at the detector can be found by summing the fields emitted by both arms and calculating the square, for which we find in the wavenumber range k to $k+dk$: $dI(\Delta L) = 2|B(k)|^2[1+\exp(ik\Delta L)]dk$. The total intensity as function of delay is simply the sum of the interference function from the various spectral regions so that:

$$I(\Delta L) = \int_{-\infty}^{\infty} dk\, |B(k)|^2 + \int_{-\infty}^{\infty} dk\, |B(k)|^2 \exp(ik\Delta L), \tag{1.1}$$

which is called the interference function. Since $I(\Delta L)$ represents the signal observed by the detector, the spectral amplitude $B(k)$ obeys the relation: $B(k) = B'(-k)$. Various properties in this interference function can be recognized. The first term is a constant, the second varies as the optical path difference ΔL varies. If we subtract the constant term the part that remains is the variable part and is called the interferogram. In this interferogram we recognize the spatial Fourier transform of the source of the interferometer and clearly shows why this technique is called Fourier transform spectroscopy: the spatial Fourier transform of the power spectrum of the source is recorded. This is demonstrated in Fig. 1.2 where we schematically show a calculated interference function representing the response of the detector in a measurement. In the upper plot of Fig. 1.2, a schematic representation of the interference function (1.1) is shown recorded by the Michelson interferometer as function of delay ΔL. The constant term in (1.1) is indicated by DC. The interferogram was obtained by subtracting the DC level. The spectrum of the source illuminating the Michelson can be calculated by Fourier transforming the interferogram, the result being shown at the bottom of Fig. 1.2, where we have plotted the intensity I as function of wave number k.

In the discussion above we did not specify anything about the source illuminating the Michelson interferometer. In practice, the source can be either a coherent source or incoherent source. In case of the an incoherent source, the width of the interferogram will be a measure of the coherence time of the source. An example of a coherent source is a pulsed laser and in this case the width of the interferogram will be a measure of the pulse duration. In principle there is no difference in using one of both but in this thesis we consider pulsed lasers as a source to perform spectroscopy.

Since high-speed computers were not available until the late 1950's, Fourier transform spectroscopy developed only slowly. From that time however, its growth has been rapid. High-speed computers are used to control the interferometer and to calculate the Fourier transform of the measured interferogram employing a fast-Fourier transform scheme. Several implementations

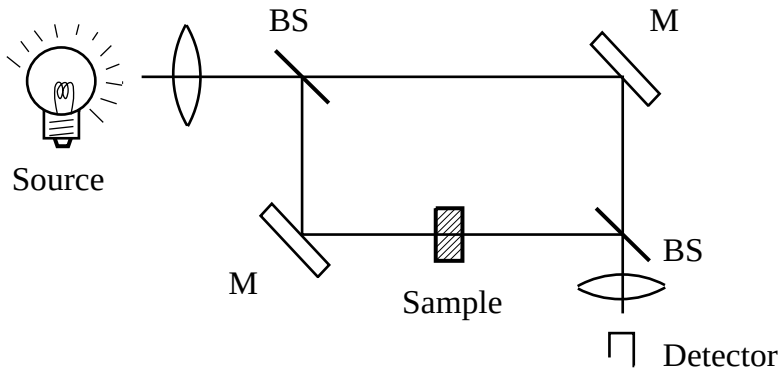

Figure 1.3: *The Mach-Zehnder interferometer. Abbreviations used: BS: beam splitter, M: mirror.*

have since been developed, like the slow-scan and step-scan interferometers, depending on the way of sampling by the detector. In the modern commercially available interferometers the movable mirror can be moved with subwavelength accuracy.

1.3 The Mach-Zehnder interferometer

Another type of interferometer which is important in this thesis is the so called Mach-Zehnder interferometer, schematically shown in Fig.1.3. The Mach-Zehnder interferometer is also a two-beam interferometer, where one of the beams is made to pass through the sample by means of a beam splitter (BS) and a mirror (M). If the arms of the interferometer are equal in length, a suitable adjustment of the mirrors gives fringes of the type that can be observed in the Michelson interferometer, showing that the instrument is related to the Michelson interferometer. Advantage of the Mach-Zehnder interferometer is that the beams are widely separated and this is a useful feature in the study of a sample which can be placed easily in one of the arms.

1.4 This thesis

The subject of this thesis concerns dynamics on ultrashort time scales. The properties we consider in this thesis are the dynamics of an electron gas and the time resolved propagation of light through a disordered strongly scattering

medium. The dynamics we study occur at sub-femtosecond time scales.

To be able to perform these studies we introduce a novel approach to time-resolved spectroscopy. The new method, is based on measuring the interferometric cross-correlation function between a pulse which has propagated through the sample we study and an undistorted reference pulse. In this approach we use a commercially available Fourier-transform interferometer in combination with a fixed Mach-Zehnder interferometer at the front end. The technique provides a reliable spectroscopic tool to do time-resolved inteferometry over a wide spectral range. The necessary stability and reproducibility to perform an interferometric measurement is provided by the commercially available Fourier-transform interferometer .

This thesis is organized as follows. In chapter 2 we discuss response functions relevant for our interferometers . These functions describe the response of a system to an external excitation. Usually, response functions of interferometers are called transfer functions. We describe difficulties to determine these functions experimentally and theoretically. The correct mathematical tools are presented to calculate these response functions. In chapter 3 we present the novel approach for measuring transfer functions. As an example we determine experimentally the transfer function of an etalon in transmission employing our new method and compare these results with the theoretically obtained transfer function. We also show that our approach has an unusual high time resolution. The method is then used to measure the time-resolved propagation through thin multiple scattering media, which is described in chapter 4. In chapter 5, experiments to study the relaxation of an non-equilibrium electron gas in gold at ultrashort time scales are presented. In the last chapter we discuss measurements to obtain the scattering properties of small particles on a substrate.

Chapter 2

Kramers-Kronig relations of an interferometer

In this chapter an introduction to response functions is given. These functions describe the response of a system to an external excitation. In general response functions are complex valued functions and the real and imaginary parts of these functions are related by a Kramers-Kronig (KK) relation. In experimental situations KK relations between amplitude and phase are often used. In this chapter we discuss KK relations between amplitude and phase and the modification of these Amplitude-Phase relations due to zeros of response functions. The treatment in the literature of response functions for interferometers does not allow for a proper use of the KK relations between amplitude and phase. As an example we formulate the proper response function for interferometers and show that this response function obeys the modified amplitude-phase relations.

2.1 Introduction

The Kramers-Kronig (KK) relations establish a connection between the real and imaginary parts of a response function. These relations, which are also known as dispersion relations, where first introduced by Kronig [4]. The dispersion relations are a direct consequence of causality, i.e. an effect does not precede its cause [5, 6] Response, usually called transfer functions in optics, describe the response of a system to an external perturbation and have to follow this causality principle. Any response function therefore satisfies a KK relation, provided that the response function are well behaved. These rela-

tions are very general and are very useful in experimental situations, where only part of the relevant information can be directly obtained. An example of the application of these relations in optics is the determination of the complex index of refraction. The real part of the index of refraction is difficult to measure as a function of frequency. Alternatively, the absorption is measured as a function of frequency. The real part of the complex index of refraction can then be calculated from the imaginary part using the KK relations.

A Gires-Tournois interferometer is an optical component very often used in ultrashort pulse generation and will be discussed in more detail in this chapter. As causality is a general principle, one expects that for interferometers appropriate KK relations can be formulated. Recently, it has been recognized [7] that the customary KK relations between amplitude and phase cannot be applied to the Gires-Tournois interferometer. We will show that this striking fact is due to an incomplete treatment of transfer functions. Similar incomplete descriptions of interferometers can be found in standard textbooks [8]. An important aspect lacking in formulating KK relations for amplitude and phase is the proper treatment of the zeros of transfer functions. This problem has also been discussed in the context of image reconstruction from a measurement of the amplitude of the object intensity in for instance astronomy [9]. Kramers-Kronig relations between amplitude and phase have been applied recently in the field of high-T_c superconducters [10], where the infrared response of these materials is determined by measuring the reflectivity (for details about this method see ref. [11]). Similar problems involving some particular problems in applying the KK relations to the Drude model have been discussed recently [12].

In this chapter, we will set up a systematic description of transfer functions satisfying properly formulated KK relations. We start by presenting KK relations for response functions of infinite media and discuss in particular the dielectric susceptibility and the complex index of refraction. KK relations for amplitude and phase are formulated and modifications and extensions due to some specific problems involved are given. Using the complex index of refraction for an infinite dielectric as a building block we develop a scattering description for semi-infinite or finite geometries such as an etalon or GT interferometer. We show that the usual transfer functions are elements of the total (scattering) S-matrix and satisfy KK relations if the full frequency dependence of all optical parameters is taken into account properly. We apply our light scattering formalism to an etalon and present numerical results for the phase

calculated from the amplitude of light reflected from an etalon. Finally, we will also briefly discuss the approach taken in Ref. [7].

2.2 KK relations and response functions for infinite media

In general response functions describe the linear response of a system to an external excitation. A good example of such a response function is the dielectric susceptibility $\chi(\mathbf{r}, \mathbf{r}', t, t')$, which relates the induced polarization in a dielectric to the applied electric field. For equilibrium response functions, which are translationally invariant in time, we write $\chi(\mathbf{r}, \mathbf{r}', t, t') = \chi(\mathbf{r}, \mathbf{r}', t - t')$. In a scalar description the total induced polarization density $P(\mathbf{r}, t)$ is given by

$$P(\mathbf{r}, t) = \int_{-\infty}^{t} dt' \int d\mathbf{r}' \chi(\mathbf{r}, \mathbf{r}', t - t') E(\mathbf{r}', t'), \tag{2.1}$$

where $E(\mathbf{r}, t)$ is the total electric field. The upper bound of the time integral reflects causality: an effect cannot precede its cause. This integral gives the total response at time t by integrating over the history, but not the future, of the interaction process. In Eq. (2.1) all functions are real-valued functions of t.

It is useful to Fourier transform the space variables into wavevectors $\mathbf{k}$

$$P_{\mathbf{k}}(t) = \int_{-\infty}^{t} dt' \int \frac{d\mathbf{k}'}{(2\pi)^3} \chi_{\mathbf{k}\mathbf{k}'}(t - t') E_{\mathbf{k}'}(t'). \tag{2.2}$$

In case of translational symmetry $\chi_{\mathbf{k}\mathbf{k}'} \equiv (2\pi)^3 \chi_{\mathbf{k}} \delta(\mathbf{k} - \mathbf{k}')$ and we obtain

$$P_{\mathbf{k}}(t) = \int_{-\infty}^{t} dt' \chi_{\mathbf{k}}(t - t') E_{\mathbf{k}}(t'). \tag{2.3}$$

The function $\chi_{\mathbf{k}}(t)$ is the general dielectric response function of a translationally invariant dielectric medium. The function $\chi_{\mathbf{k}}(t)$ is a real-valued function of time and can be calculated in principle using a microscopic theory. Generally, $\chi_{\mathbf{k}}(t)$ can be written as a correlation function of dynamical physical quantities (see for instance [13]), which is odd under time reversal $\chi_{\mathbf{k}}(t) = -\chi_{\mathbf{k}}(-t)$.

The time convolution can be disentangled by applying a Fourier transformation leading to

$$P_{\mathbf{k}}(\omega) = \chi_{\mathbf{k}}[\omega + i\varepsilon] E_{\mathbf{k}}(\omega), \tag{2.4}$$

where besides Fourier transforms of $P_{\mathbf{k}}(t)$ and $E_{\mathbf{k}}(t)$ one notes the appearance of the Fourier-Laplace transform of $\chi_{\mathbf{k}}(t)$, defined by

$$\chi_{\mathbf{k}}[\omega + i\varepsilon] \equiv \int_0^\infty dt\, \chi_{\mathbf{k}}(t)\, \mathrm{e}^{i(\omega+i\varepsilon)t}, \tag{2.5}$$

where ε is infinitesimally small and positive. Physically, the parameter ε may represent an adiabatic switching on of the coupling between the system and external fields. Throughout this thesis it is assumed that $\lim \varepsilon \downarrow 0$ has to be taken in formulas in which ε appears explicitly. The Fourier-Laplace transform is the result of the finite upper bound of the time integral in (2.3) and, therefore, implicitly represents causality. Often the wavelength of light is much larger than the characteristic spatial variations, in which case the dielectric susceptibility $\chi_{\mathbf{k}}$ does not depend on $\mathbf{k}$ and simplifies to $\chi_{\mathbf{k}}[\omega+i\varepsilon] \approx \chi[\omega+i\varepsilon] \equiv \epsilon[\omega+i\varepsilon]-1$. The dielectric constant $\epsilon[\omega + i\varepsilon]$ describes the interaction of an electric field with an infinite medium and is taken to have a Lorentz-type behavior

$$\epsilon[\omega + i\varepsilon] = 1 + \frac{\omega_0^2 \mathcal{F}}{\omega_0^2 - (\omega + i\varepsilon)^2 - 2i(\omega + i\varepsilon)/T_2}, \tag{2.6}$$

where ω_0 is a resonance frequency, T_2 the linewidth of the resonance and $\mathcal{F}$ a dimensionless parameter. This simple but nontrivial Lorentz-type behavior characterizes an interaction with a set of many identical harmonic oscillators. The dielectric susceptibility exhibits both dispersion and absorption, which is conventially written as

$$\chi[\omega + i\varepsilon] \equiv \chi'(\omega) + i\chi''(\omega), \tag{2.7}$$

where the real and imaginary part satisfy the KK relations (2.13) and (2.14) to be presented below.

Here we discuss the appropriate mathematical tools for analyzing response functions. For complex frequency z and Im $z > 0$ the Fourier-Laplace transform $H[z]$ of a real-valued function $h(t)$ is defined by

$$H[z] \equiv \int_0^\infty dt\, h(t) e^{izt}, \tag{2.8}$$

for Im $z < 0$ $H[z]$ is defined by

$$H[z] \equiv -\int_{-\infty}^0 dt\, h(t) e^{izt}. \tag{2.9}$$

For physical applications $h(t)$ is real and bounded as a function of t and odd under time reversal. It follows from Eqs. (2.8) and (2.9) that

$$H[\omega + i\varepsilon] - H[\omega - i\varepsilon] = \int_{-\infty}^{\infty} dt\, h(t)\, e^{i\omega t} \tag{2.10}$$

gives the Fourier transform of $h(t)$. Note that for odd $h(t)$ the Fourier transform (2.10) is imaginary. Defining the real functions $H'(\omega)$ and $H''(\omega)$ by

$$H[\omega + i\varepsilon] \equiv H'(\omega) + iH''(\omega), \tag{2.11}$$

from (2.9) one then finds for odd functions $h(t)$

$$H[\omega - i\varepsilon] = H'(\omega) - iH''(\omega). \tag{2.12}$$

$H'(\omega)$ and $H''(\omega)$ are respectively even and odd functions of frequency ω. Employing the inverse Fourier transform for $h(t)$ in (2.8) and (2.9) it follows from (2.11) and (2.12) that

$$H'(\omega) = P \int \frac{d\omega'}{\pi} \frac{H''(\omega')}{\omega' - \omega}, \tag{2.13}$$

where $P\int$ stands for a principal-value integral. The KK relation (2.13) enables one to calculate the real part of the complex function $H[\omega + i\varepsilon]$ from its imaginary part. The inverse KK relation is given by

$$H''(\omega) = -P \int \frac{d\omega'}{\pi} \frac{H'(\omega')}{\omega' - \omega}. \tag{2.14}$$

In the derivation of the KK relations (2.13) and (2.14) we only assumed that real-valued $h(t)$ are bounded functions of time and are odd under time reversal. For the frequency-dependent quantity $H[z]$, these assumptions translate into the following conditions. The response function $H[z]$ is analytic in the upper (lower) half frequency plane for Im $z > 0$ (Im $z < 0$). The function $H[z]$ converges to a constant $H[\infty]$ for $|z| \to \infty$ (Im $z \neq 0$). For $H[\infty] \neq 0$, KK relations should be formulated for $H[z] - H[\infty]$. An example is the complex index of refraction $n[\omega + i\varepsilon] \equiv \eta(\omega) + i\kappa(\omega)$ which is related to the dielectric constant by the Maxwell relation $n^2 = \epsilon$. Since $\eta \to 1$ for $\omega \to \infty$, KK relations should be formulated for $\eta(\omega) - 1$ and $\kappa(\omega)$ (see below). Note that for $\eta(\omega) \neq 1$ one cannot, as is usually done, approximate the index of refraction n by a constant without violating the KK relations for n.

2.3 KK relations for amplitude and phase

From an experimental point of view the KK relations given above are particularly useful for systems where either the in-phase or out-of-phase response can be measured directly as a function of frequency. This is for instance the case for low-frequency electromagnetic waves (up to the 1 THz region, see for instance [14]). At optical frequencies, however, one can usually measure the intensity and only with considerable difficulty the phase. For these situations one is interested in KK relations formulated for amplitude and phase [15].

In order to partition the response function $H[\omega + i\varepsilon]$ in amplitude and phase we consider

$$\ln H[\omega + i\varepsilon] = \ln \left(|H[\omega + i\varepsilon]| e^{i\phi(\omega)} \right) = \ln |H[\omega + i\varepsilon]| + i\phi(\omega), \tag{2.15}$$

where $|H[\omega + i\varepsilon]|$ and $\phi(\omega)$ are the amplitude and phase, respectively. KK relations for amplitude and phase seem to follow from (2.13) and (2.14) using $\ln |H[\omega+i\varepsilon]|$ and $\phi(\omega)$ as the functions of interest. However, in this formulation problems may be encountered, because for complex frequencies the response function might have zeros for which the logarithm is not defined. For real-valued and odd $h(t)$ one has $H[x + iy] = H[-x + iy]^*$, where x and y are real, and * stands for complex conjugation. Therefore, unless zeros of response functions $H[z]$ lie on the imaginary axis, zeros appear in pairs in the upper half frequency plane. In order for amplitude and phase to satisfy KK relations it is required that $\ln H[z]$ is an analytic function for Im $z > 0$. To properly account for the occurrence of zeros, the application of KK relations for amplitude and phase has to be modified.

We can distinguish between two different types of zeros: zeros for finite and zeros for infinite frequency, respectively. The problem of zeros for finite complex frequency has been discussed by van Kampen [16] and Toll [17]. Following Toll, we assume that the response function under investigation is analytic for Im $z > 0$ and has N zeros (including multiplicity) in the upper half frequency plane. With the so-called Blaschke product

$$B(z) \equiv \prod_n \frac{z - \mu_n}{\mu_n^* - z}, \tag{2.16}$$

where the complex constants μ_n are the zeros of $H[z]$ with positive imaginary part, we can then [18] construct a function $\widetilde{H}[z]$

$$H[z] \equiv \widetilde{H}[z] B(z), \tag{2.17}$$

which has no zeros for Im $z > 0$. The necessary and sufficient conditions [19] to write $H[z]$ as the product expansion (2.17) are that both the integral

$$\int_0^\infty \frac{\ln|H[\omega+i\varepsilon]|}{1+\omega^2}d\omega \tag{2.18}$$

and the Blaschke product over all zeros have to be finite. Van Kampen [16] has shown that the latter is the case if the zeros are distributed such that

$$\sum_{n=1}^{N}\frac{\mu_{ni}}{|\mu_n|^2} < \infty, \tag{2.19}$$

where μ_{ni} stands for the imaginary part of the n-th zero. Evidently, for finite N this condition is always satisfied. Since the amplitude of the function $|B(\omega)| = 1$, the functions $H[z]$ and $H[z] \equiv \widetilde{H}[z]B(z)$ yield the same amplitude in the neighborhood of the real frequency axis: $|H[\omega+i\varepsilon]| = \left|\widetilde{H}[\omega+i\varepsilon]\right|$. The amplitude of the functions $H[z]$ and $\widetilde{H}[z]$ differ in the complex frequency plane away from the real axis, because there $|B(z)| \neq 1$. Apparently, the amplitude $|H[\omega+i\varepsilon]|$ does not determine $H[z]$ uniquely.

By construction, the function $\widetilde{H}[z] \equiv \left|\widetilde{H}[z]\right|\exp(i\widetilde{\phi}[z])$, has no zeros in the upper half frequency plane. The KK relation for the phase $\widetilde{\phi}(\omega)$ reads

$$\widetilde{\phi}(\omega) = -P\int_{-\infty}^{\infty}\frac{d\omega'}{\pi}\frac{\ln|\widetilde{H}[\omega'+i\varepsilon]|}{\omega'-\omega}. \tag{2.20}$$

Note that Eq. (2.20) is a true KK relation, because $\ln\widetilde{H}[z]$ is analytic for Im $z > 0$. Since near the real frequency axis $|\widetilde{H}[\omega+i\varepsilon]| = |H[\omega+i\varepsilon]|$, we may write (2.20) as

$$\widetilde{\phi}(\omega) = -P\int_{-\infty}^{\infty}\frac{d\omega'}{\pi}\frac{\ln|H[\omega'+i\varepsilon]|}{\omega'-\omega}. \tag{2.21}$$

The phase $\phi(\omega)$ corresponding to $H[\omega+i\varepsilon]$ follows from [17]

$$\phi(\omega) = \widetilde{\phi}(\omega) + \arg\ B(\omega). \tag{2.22}$$

Hence, the modified KK relations connecting $\ln|H[\omega+i\varepsilon]|$ and $\phi(\omega)$ are [17]

$$\phi(\omega) = -P\int_{-\infty}^{\infty}\frac{d\omega'}{\pi}\frac{\ln|H[\omega'+i\varepsilon]|}{\omega'-\omega} + \arg B(\omega). \tag{2.23}$$

and

$$\ln\ |H[\omega+i\varepsilon]| = P\int_{-\infty}^{\infty}\frac{d\omega'}{\pi}\ \frac{\phi(\omega')-\arg B(\omega')}{\omega'-\omega}. \tag{2.24}$$

Suppose that the amplitude of the transfer function $H[\omega + i\varepsilon]$ has been measured. With only this information, it is still not possible to reconstruct the full transfer function, because such a measurement does not provide all information about the zeros with positive imaginary part. Therefore, to apply the Blaschke product the number and location of the zeros of $H[z]$ with positive imaginary part have still to be determined. If there are N such zeros the Blaschke product is given by $2N$ parameters; i.e. the real and imaginary part of the zeros (note that zeros generally appear in pairs). Evidently, in an experiment the behavior of $H[\omega + i\varepsilon]$ and $H[z]$ are usually not known in advance. The location of the zeros μ_n can be determined in the following way. As a rule of thumb, the real part μ_{nr} of the zeros lie close to frequencies where minima of the measured amplitude $|H[\omega + i\varepsilon]|$ occur. Note that minima in $|H[\omega + i\varepsilon]|$ do not necessarily imply the occurrence of a zero of $H[z]$ lying in the upper half frequency plane. Zeros can also lie in the lower half frequency plane. The latter zeros, however, are not to be included in the Blaschke product. Whether or not there is a zero with positive imaginary part ($\mu_{ni} > 0$) can be concluded by measuring the phase $\phi(\omega)$ at one particular frequency ω in the neighborhood of the real part μ_{nr} of the corresponding zero relative to the phase at $\omega = \mu_{nr}$. If the latter phase differs from the calculated phase $\widetilde{\phi}(\omega) - \widetilde{\phi}(\mu_{nr})$, there is a zero with positive imaginary part. Using Eq. (2.17) we can write:

$$\arg B(\omega) - \arg B(\mu_{nr}) = [\phi(\omega) - \phi(\mu_{nr})] - \left[\widetilde{\phi}(\omega) - \widetilde{\phi}(\mu_{nr})\right] \tag{2.25}$$

which can be used to determine the imaginary part $\mu_{ni} > 0$ of a zero contributing to the Blaschke product. A zero with positive imaginary part leads asymptotically to an increase in $\arg B(\omega)$ of π (unpaired zero) or 2π (paired zeros) for frequencies $|\omega - \mu_{nr}| >> 1$. If a phase measurement cannot be performed, it may be possible to use a theoretical model to obtain information about the location of zeros with positive imaginary part.

The other type of zeros of $H[z]$ may occur for infinite complex frequency. The presence of these zeros depends on the details of the specific physical system. Such a situation arises for instance in the case of light reflected from a surface. The corresponding reflection coefficient goes to zero as $1/|z|^2$ for $|z| \to \infty$. This particular problem has been analyzed in literature by Smith [20], who investigated the KK relation for the response function for reflection. The $\ln(1/|z|^2)$ divergence can be removed by considering the auxiliary function

for $\omega \neq \nu$

$$\mathcal{G}[z;\omega,\nu] \equiv \left\{\frac{1}{z-\omega} - \frac{1}{z-\nu}\right\} \ln \widetilde{H}[z], \tag{2.26}$$

which goes to zero for $|z| \to \infty$. Note that we have removed zeros for finite complex frequency using $\widetilde{H}[z]$. Employing this auxiliary function a so-called subtracted KK relation may be derived for the amplitude $\ln |H[\omega + i\varepsilon]|$ [20]

$$\begin{aligned} &\ln |H[\omega + i\varepsilon]| - \ln |H[\nu + i\varepsilon]| = \\ &\quad P \int_{-\infty}^{\infty} \frac{d\omega'}{\pi} \{\phi(\omega') - \arg B(\omega')\} \left\{\frac{1}{\omega' - \omega} - \frac{1}{\omega' - \nu}\right\}. \end{aligned} \tag{2.27}$$

The inverse relation is still given by Eq. (2.23). Equation (2.27) resembles the difference of two different KK relations. However, this difference cannot be disentangled because the integrals are individually divergent. The variables ω and ν cannot be separated in Eq. (2.27). In practice, for fixed ν the ratio $|H[\omega+i\varepsilon]|/|H[\nu+i\varepsilon]|$ can be determined from a measurement of the phase $\phi(\omega)$ and using Eq. (2.27), where the N zeros determining $\arg B(\omega)$ can be obtained from considering the π (unpaired zeros) or 2π (paired zeros) jumps in the measured phase $\phi(\omega)$. Thus, $H[\omega + i\varepsilon]$ would be known up to a multiplicative constant. This constant can be fixed employing either a theoretical argument or an absolute measurement of $|H[\omega + i\varepsilon]|$ for one fixed frequency ω [20].

2.4 Scattering formalism

2.4.1 Reflection and refraction at an interface

In an actual experiment the medium is always semi-infinite or finite and we have to consider the boundaries explicitly. In this section we consider a plane boundary at $z = 0$ between vacuum ($z < 0$) and a medium with index of refraction $n[\omega+i\varepsilon]$ ($z > 0$). When introducing an interface one has to relate the amplitudes and the directions of propagation $\mathbf{k}$ of the various fields on opposite sides. Scattering theory is ideally suited for this. In a scalar description one decomposes the field solutions as [21]

$$E(\mathbf{r},\omega) = \int d\mathbf{r}' S_{\mathbf{r}\mathbf{r}'}[\omega + i\varepsilon] E^{\mathrm{inc}}(\mathbf{r}',\omega) \tag{2.28}$$

defining the S-matrix. In the context of interferometers, matrix elements of S are usually called transfer functions. Note that the S-matrix relates the *total* field $E(\mathbf{r},\omega)$ to the *incoming* field $E^{\mathrm{inc}}(\mathbf{r}',\omega)$. Compare (2.28) with

(2.1), where the susceptibility relates two different *total* fields. We use an incoming monochromatic complex wave with frequency ω_0 and wavevector $\mathbf{k}^{\rm inc} \equiv (\omega_0/c)\hat{\mathbf{k}}^{\rm inc}$ ($\hat{\mathbf{k}}^{\rm inc} = \mathbf{k}^{\rm inc}/k^{\rm inc}$ and c is the speed of light)

$$E^{\rm inc}(\mathbf{r},\omega) = E_0\delta(\omega-\omega_0)\exp(i\mathbf{k}^{\rm inc}\cdot\mathbf{r}). \tag{2.29}$$

Substituting (2.29) in (2.28) gives the S-matrix with one space variable Fourier transformed

$$\begin{aligned} E(\mathbf{r},\omega) &= E_0\delta(\omega-\omega_0)\int d\mathbf{r}' S_{\mathbf{r}\mathbf{r}'}[\omega+i\varepsilon]\exp(i\mathbf{k}^{\rm inc}\cdot\mathbf{r}') && (2.30)\\ &= E_0\delta(\omega-\omega_0)S_{\mathbf{r}\mathbf{k}^{\rm inc}}[\omega+i\varepsilon]. && (2.31)\end{aligned}$$

In the following we restrict ourselves to normal incidence. The total field is decomposed into three parts: a transmitted part for $z>0$, a reflected part and the original (unperturbed) incoming wave for $z<0$. With this decomposition, the S-matrix can be written as

$$\begin{aligned} S^{z<0}_{\mathbf{r}\mathbf{k}^{\rm inc}}[\omega+i\varepsilon] &= r[\omega+i\varepsilon]\exp(-i\mathbf{k}^{\rm inc}\cdot\mathbf{r}) + \exp(+i\mathbf{k}^{\rm inc}\cdot\mathbf{r})\,, && (2.32)\\ S^{z>0}_{\mathbf{r}\mathbf{k}^{\rm inc}}[\omega+i\varepsilon] &= t[\omega+i\varepsilon]\exp(i\mathbf{k}^{\rm trans}\cdot\mathbf{r})\,, && (2.33)\end{aligned}$$

with $\mathbf{k}^{\rm trans} = n[\omega+i\varepsilon]\mathbf{k}^{\rm inc}$ and where we have used the Fresnel coefficients, which relate the amplitudes of the waves scattering at the interface. The Fresnel coefficients do not depend on the polarization and are given by [8]

$$\begin{aligned} r[\omega+i\varepsilon] &= \frac{n[\omega+i\varepsilon]-1}{n[\omega+i\varepsilon]+1}, && (2.34)\\ t[\omega+i\varepsilon] &= \frac{2n[\omega+i\varepsilon]}{n[\omega+i\varepsilon]+1}. && (2.35)\end{aligned}$$

Fourier transforming Eqs. (2.32) and (2.33) finally gives for the S-matrix elements

$$\begin{aligned} S_{\mathbf{k}\mathbf{k}^{\rm inc}}[\omega+i\varepsilon] = 4\pi^2\delta(\mathbf{k}_\perp)\Bigg(t[\omega+i\varepsilon]\frac{i}{k_z^{\rm trans}-k_z} &\quad +r[\omega+i\varepsilon]\frac{i}{k_z+k_z^{\rm inc}+i\varepsilon}\\ &\quad +\frac{i}{k_z-k_z^{\rm inc}+i\varepsilon}\Bigg), \end{aligned} \tag{2.36}$$

where the wavevectors have been decomposed into parts perpendicular (index $\perp$) and parallel (index z) to the incoming beam and we have used $k_\perp^{\rm inc}=0$ and $k_\perp^{\rm trans}=0$. For $n[\omega+i\varepsilon]\to 1+i\varepsilon$, $r[\omega+i\varepsilon]\to 0$ and $t[\omega+i\varepsilon]\to 1$ leading to

$$S_{\mathbf{k}\mathbf{k}^{\rm inc}}[\omega+i\varepsilon] = 8\pi^3\delta(\mathbf{k}_\perp)\delta(k_z-k_z^{\rm inc}), \tag{2.37}$$

as expected. From now on we only consider the reflection ($\mathcal{R}$) and transmission ($\mathcal{T}$) components of the S-matrix given by

$$\mathcal{R}_{\mathbf{k}\mathbf{k}^{\rm inc}}[\omega + i\varepsilon] \equiv 4\pi^2\delta(\mathbf{k}_\perp) r[\omega + i\varepsilon] \frac{i}{k_z + k_z^{\rm inc} + i\varepsilon}, \tag{2.38}$$

and

$$\mathcal{T}_{\mathbf{k}\mathbf{k}^{\rm inc}}[\omega + i\varepsilon] \equiv 4\pi^2\delta(\mathbf{k}_\perp) t[\omega + i\varepsilon] \frac{i}{k_z^{\rm trans} - k_z}. \tag{2.39}$$

We have already shown that the real and imaginary parts of the index of refraction satisfy KK relations. The index of refraction $n[\omega + i\varepsilon]$ is an analytic function in the upper half frequency plane, so both $r[\omega + i\varepsilon]$ and $t[\omega + i\varepsilon]$ are analytic functions of $\omega + i\varepsilon$. The same is true for $\mathcal{R}_{\mathbf{k}\mathbf{k}^{\rm inc}}[\omega + i\varepsilon]$ and $\mathcal{T}_{\mathbf{k}\mathbf{k}^{\rm inc}}[\omega + i\varepsilon]$. In physical applications one has $n[\omega + i\varepsilon] + 1 \neq 0$ for any frequency ω. Consequently, $\mathcal{R}_{\mathbf{k}\mathbf{k}^{\rm inc}}[\omega + i\varepsilon]$ and $\mathcal{T}_{\mathbf{k}\mathbf{k}^{\rm inc}}[\omega + i\varepsilon]$ each satisfy KK relations.

The use of the Amplitude-Phase relations for transmission through a single interface does not give rise to any problems, because the nominator of Eq. (2.35) is a nonzero function of frequency. The formulation of Amplitude-Phase relations for reflection however, does give rise to problems as has been shown by Clifford [22]. We will briefly describe Cliffords results in the context of the above formalism. For a certain combination of indices of refraction, it could happen that at certain frequencies the two complex indices of refraction match. In that case there is no reflection and we find one zero for the S-matrix (or transfer function $\mathcal{R}_{\mathbf{k}\mathbf{k}^{\rm inc}}$). One zero might also be found for fixed frequency and for a certain angle of incidence corresponding to the Brewster angle. Sometimes one finds the two above mentioned zeros occurring at the same time. It may happen that these zeros coincide, in which case we have one zero of second order. The case of one zero was worked out in detail by Clifford [22]. The phase of the reflected beam was calculated using KK relations and compared with the theoretical result. It was shown that the correct phase could be achieved by adding the phase of the Blaschke product in a manner as described above.

2.4.2 The transfer function of an etalon.

The real and imaginary part of transfer functions of an etalon satisfy KK relations. However, KK relations between amplitude and phase has given rise to confusion in literature, see for instance [7]. So, we will treat this case in detail.

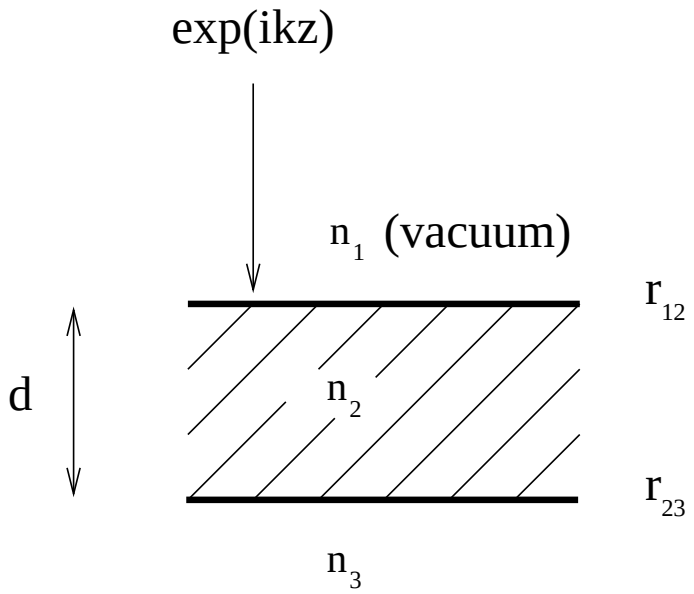

Figure 2.1: *Schematic picture of an etalon, with unequal reflection coefficients* $|r_{12}| \neq |r_{23}|$. *In a Gires-Tournois interferometer the third medium is a metal giving* $|r_{23}| \approx 1$. *The arrow indicates an incoming beam* $\exp(ikz)$.

We consider an etalon in which the two interfaces have different reflection coefficients. As indicated in Fig. 2.1 three different media are involved: vacuum ($n_1 = 1$) and two dielectric media with indices of refraction n_2 and n_3. For perpendicular incidence of a plane wave the S-matrix elements for reflection and transmission are respectively given by

$$\begin{aligned} \mathcal{R}_{\mathbf{k}\mathbf{k}^{\rm inc}}[\omega + i\varepsilon] &= 4\pi^2\delta(\mathbf{k}_\perp)\frac{i}{k_z + k_z^{\rm inc} + i\varepsilon} \times \\ &\quad \frac{r_{12}[\omega + i\varepsilon] + r_{23}[\omega + i\varepsilon]\exp(i\omega n_2[\omega + i\varepsilon]\delta)}{1 + r_{12}[\omega + i\varepsilon]r_{23}[\omega + i\varepsilon]\exp(i\omega n_2[\omega + i\varepsilon]\delta)} \end{aligned} \quad (2.40)$$

and

$$\begin{aligned} \mathcal{T}_{\mathbf{k}\mathbf{k}^{\rm inc}}[\omega + i\varepsilon] &= 4\pi^2\delta(\mathbf{k}_\perp)\frac{i}{k_z^{\rm trans} - k_z} \times \\ &\quad \frac{t_{12}[\omega + i\varepsilon]t_{23}[\omega + i\varepsilon]\exp(i\omega n_2[\omega + i\varepsilon]\delta/2)}{1 + r_{12}[\omega + i\varepsilon]r_{23}[\omega + i\varepsilon]\exp(i\omega n_2[\omega + i\varepsilon]\delta)}, \end{aligned} \quad (2.41)$$

where in both equations $\delta = 2d/c$ and d is the thickness of the interferometer. The Fresnel coefficients at the boundary between media with indices of

refraction $n_i[\omega + i\varepsilon]$ and $n_j[\omega + i\varepsilon]$ $(i, j = 1, 2, 3)$ are given by [8]

$$r_{ij}[\omega + i\varepsilon] = \frac{n_i[\omega + i\varepsilon] - n_j[\omega + i\varepsilon]}{n_i[\omega + i\varepsilon] + n_j[\omega + i\varepsilon]} \tag{2.42}$$

and

$$t_{ij}[\omega + i\varepsilon] = \frac{2n_i[\omega + i\varepsilon]n_j[\omega + i\varepsilon]}{n_i[\omega + i\varepsilon] + n_j[\omega + i\varepsilon]}. \tag{2.43}$$

The complex wavevector k_z^{trans} is given by $k_z^{\text{trans}} = n_3 k_z^{\text{inc}}$. Eqs. (2.40) and (2.41) describe both the etalon and the GT interferometer. For the GT interferometer the reflection coefficient $r_{23}[\omega + i\varepsilon] \approx 1$. This is usually achieved by incorporating absorption in medium 3. Note that we have used the full frequency dependence of the indices of refraction contrary to Refs. [7] and [8], where real and constant indices of refraction were used for the three media involved.

If we only measure in the backscattering direction and drop the wavevector $\mathbf{k}$ dependence we get for the S-matrix element

$$\mathcal{R}[\omega + i\varepsilon] = \frac{r_{12}[\omega + i\varepsilon] + r_{23}[\omega + i\varepsilon] \exp(i\omega n_2[\omega + i\varepsilon]\delta)}{1 + r_{12}[\omega + i\varepsilon] r_{23}[\omega + i\varepsilon] \exp(i\omega n_2[\omega + i\varepsilon]\delta)}, \tag{2.44}$$

which in optics is called the transfer function for reflection. Similarly, we find the usual form of the transfer function for transmission

$$\mathcal{T}[\omega + i\varepsilon] = \frac{t_{12}[\omega + i\varepsilon] t_{23}[\omega + i\varepsilon] \exp(i\omega n_2[\omega + i\varepsilon]\delta/2)}{1 + r_{12}[\omega + i\varepsilon] r_{23}[\omega + i\varepsilon] \exp(i\omega n_2[\omega + i\varepsilon]\delta)}, \tag{2.45}$$

when we detect directly behind the etalon in medium 3.

To show that a KK relation exists for $\mathcal{R}[\omega + i\varepsilon]$ and $\mathcal{T}[\omega + i\varepsilon]$ we assume that the dielectric media 2 and 3 exhibit a Lorentz-type behavior, see Eq. (2.6). Media 2 and 3 are described by different parameters ω_0, $\mathcal{F}$, and T_2. Transfer functions (2.44) and (2.45) are both functions of Fresnel coefficients. As the Fresnel coefficients are analytic in the upper half frequency plane, both transfer functions are analytic functions of $\omega + i\varepsilon$, provided that there are no zeros in the denominators of (2.44) and (2.45). The Fresnel coefficients $r_{12}[\omega + i\varepsilon]$ and $r_{23}[\omega + i\varepsilon]$ always have an amplitude smaller than one and the exponent $\exp(i\omega n_2[\omega + i\varepsilon]\delta)$ is a decreasing function of $\omega\kappa_2(\omega)$, where the odd function $\kappa_2(\omega)$ is the imaginary part of $n_2[\omega + i\varepsilon]$. We conclude that no zeros occur for these denominators in the upper half frequency plane. Hence, the real and imaginary parts of (2.44) and (2.45) satisfy KK relations (2.13) and (2.14). In the limit $\omega \to \infty$, the transmission transfer function goes to unity. Therefore,

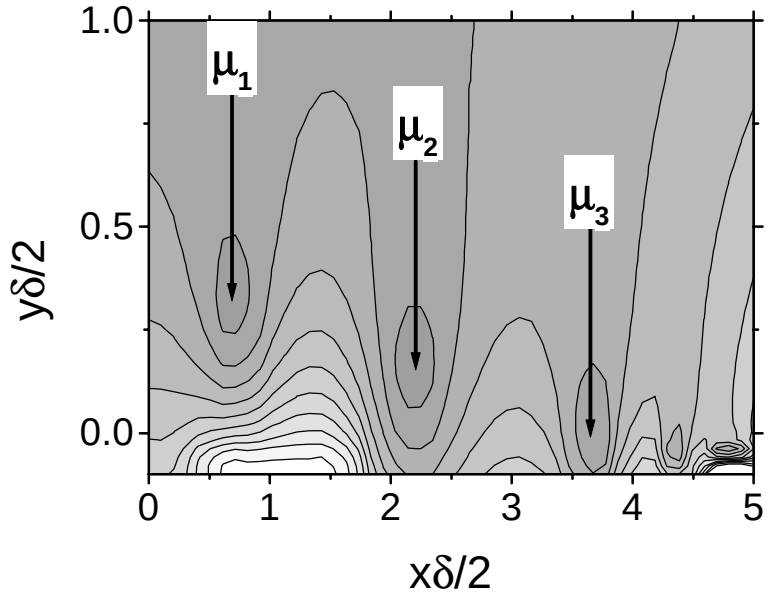

Figure 2.2: *The amplitude of a reflection transfer function $\mathcal{R}$ for the etalon of Fig. 2.1 as a function of dimensionless complex frequency $x\delta/2 + iy\delta/2$ with $\delta = 2d/c$ and d being the thickness of the etalon. The contour map of $|\mathcal{R}|$ shows the location of zeros (μ_n) of $\mathcal{R}$ in the upper half frequency plane. $\mu_1 = 0.733 + 0.35i$, $\mu_2 = 2.158 + 0.192i$ and $\mu_3 = 3.591 + 0.024i$. The indices of refraction of the three media involved are calculated from dielectric constants exhibiting Lorentz-type behavior and employing the particular parameter set (2.46) and (2.47) as described in the text.*

a KK relation should be formulated for $\mathcal{T}[\omega + i\varepsilon] - 1$. In literature this is sometimes written as $\mathcal{T}[\omega + i\varepsilon] - \mathcal{T}[\infty]$.

Because zeros for the transmission transfer function (2.45) do not occur, amplitude-phase KK relations exist. For reflection, however, we may find zeros for complex frequencies. If the reflection transfer function is analytic in the upper half frequency plane, it is possible to employ a product expansion like (2.17). Summarizing, the reflection and transmission transfer functions satisfy amplitude-phase KK relations.

2.5 Numerical application

In this section we apply the amplitude-phase KK relations (2.23) and (2.27) to light reflected from the etalon described in the preceding section. We numerically calculate the phase from the amplitude and vice versa. We compare the numerical results we get from the numerical evaluation of the integrals with results directly calculated from the transfer function (2.44). In both calculations, we employed the generic dielectric constant (2.6) for the two dielectric media with the following parameter set. For medium 2:

$$\omega_0\delta/2 = 5,\ \mathcal{F} = 1,\ 2T_2/\delta = 100, \tag{2.46}$$

and for medium 3:

$$\omega_0\delta/2 = 0.5,\ \mathcal{F} = 10,\ 2T_2/\delta = 100. \tag{2.47}$$

The frequencies are measured in units of $2/\delta$. For these parameter values in (2.44) we found three pairs of zeros lying in the upper half frequency plane: $\mu_1 = \pm 0.733 + 0.35i, \mu_2 = \pm 2.158 + 0.192i$ and $\mu_3 = \pm 3.591 + 0.024i$. For the chosen values of $2T_2/\delta$, these zeros give *sharp* minima in the amplitude of (2.44). Note that these minima do not lie at the material resonances $\omega_0\delta/2$. These zeros determine the Blaschke product for this particular case. In Fig. 2.2 we plotted $|\mathcal{R}[x + iy]|$ as a function of frequencies $x\delta/2$ and $y\delta/2$. The zeros of Eq. (2.44) in the upper half frequency plane are indicated by arrows. In Fig. 2.2 there is a zero at $\mu_{nr} \approx 4.3$ with $\mu_{ni} < 0$, which therefore should not be included in the Blaschke product, despite the fact that it will give a minimum for the amplitude of (2.44) for real frequency.

2.5.1 Amplitude-phase relations

In order to calculate the phase we have used (2.23). The amplitude is obtained by taking the absolute value of Eq. (2.44). To numerically evaluate the frequency integral in Eq. (2.23), we used a 3-point trapezoidal rule. In Fig. 2.3 the calculated phase $\phi(\omega)$ (solid line) is given as function of frequency ω. The phase (dashed line) excluding the contribution of the Blaschke product is shown for comparison. The difference Δ (solid line) between the calculated phase $\phi(\omega)$ (dashed line) and the exact phase following from the transfer function (2.44) is depicted in Fig. 2.4. Despite the presence of sharp resonances excellent agreement is obtained using a simple integration scheme.

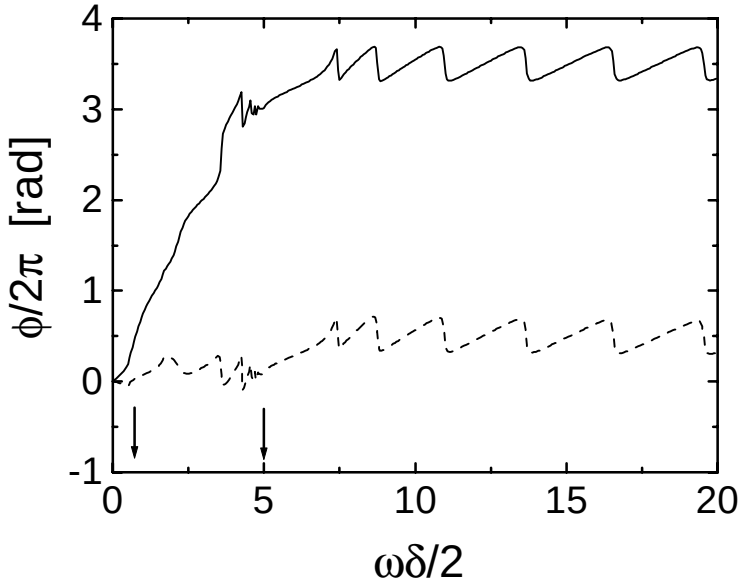

Figure 2.3: *The phase $\phi(\omega)$ (solid line) of a reflection transfer function $\mathcal{R}$ for the etalon of Fig. 2.1 as a function of dimensionless frequency $\omega\delta/2$ with $\delta = 2d/c$. The phase $\phi(\omega)$ is numerically calculated from $|\mathcal{R}(\omega)|$ using an amplitude-phase KK relation including the contribution from the Blaschke product, determined by the zeros of $\mathcal{R}$ in the upper half frequency plane, and employing the same set of parameters as in Fig. 2.2. The phase (dashed line) excluding the contribution from the Blaschke product is shown for comparison. The arrows indicate the location of the resonances of media 2 and 3 ($\omega_0\delta/2 = 0.5$ and $\omega_0\delta/2 = 5$, respectively).*

The argument $\arg B(\omega)$ of the Blaschke product determined by different numbers of pairs of zeros is shown in Fig. 2.5 as a function of frequency. The arrows indicate the location of the zeros with positive real part. The solid line represents the full Blaschke product used in the calculation described above. The phases of the Blaschke products excluding one (dotted line) and two (dashed line) pairs of zeros, respectively, are also shown in Fig. 2.5. One observes that there is an increase of 2π in $\arg B(\omega)$ in the neighborhood of $\omega \approx \mu_{nr}$ (for unpaired zeros the increase would be π). For smaller values of μ_{ni} the increase in $\arg B(\omega)$ at $\omega \approx \mu_{nr}$ is faster. Note that $\arg B(\omega)$ is a nondecreasing function of frequency as it should be. One can conclude from the behavior of $\arg B(\omega)$ that large differences between the calculated and measured phases can occur if insufficient zeros have been taken into account.

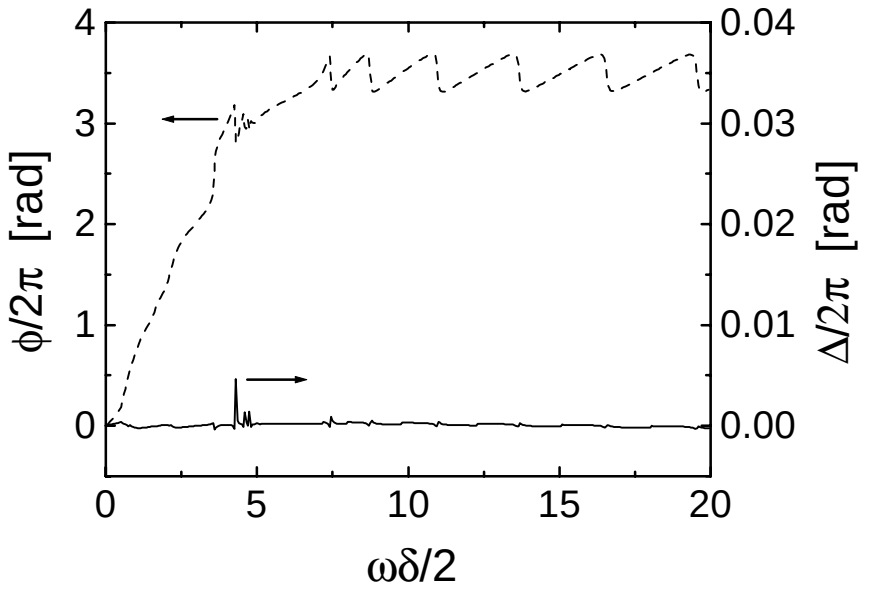

Figure 2.4: *The difference Δ (solid line) between the numerically calculated phase and the exact phase of a reflection transfer function $\mathcal{R}$ for the etalon of Fig. 2.1. The numerically computed phase (dashed line) results from an amplitude-phase KK relation. The same parameter set as in Figs. 2.2 and (2.3) is employed.*

For $0 < \omega < 2$, the difference between the full $\arg B(\omega)$ determined by all three pairs of zeros (solid line) of (2.44) and $\arg B(\omega)$ determined by the first two pairs of zeros with $\mu_{nr} < 2$ (dashed line) is only 10^{-2}.

We have simulated the experimental situation of having measured the amplitude as function of frequency and the phase at particular frequencies near minima of the obtained amplitude. With this information, the location and the number of zeros were determined as described in section 3. The position of the real part (μ_{nr}) of the zeros is given by the minima of the amplitude. If $[\phi(\omega)-\phi(\mu_{nr})]-[\widetilde{\phi}(\omega)-\widetilde{\phi}(\mu_{nr})] = 0$ the zero does not contribute to the Blaschke product (i.e. $\mu_{ni} < 0$). The imaginary parts of the contributing zeros are determined by using an iteration scheme. We started with the lowest frequency minimum. An estimate of the imaginary part of the corresponding (paired) zero can be made by assuming only one contributing zero. For the next zero the same method is used, but now the estimate for the first zero is included. We proceed in this fashion until all contributing zeros are found. With these estimates for the location of the contributing zeros we again calculated the

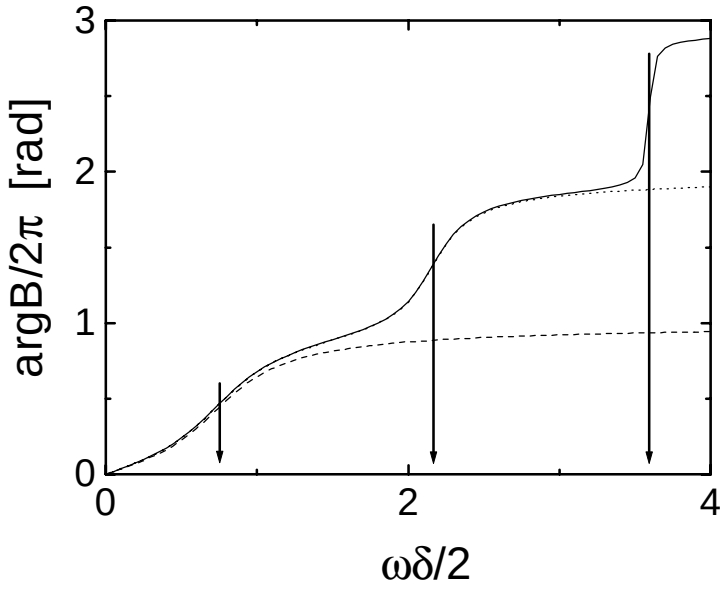

Figure 2.5: *The phase of the Blaschke product* $\arg B(\omega)$ *is shown as a function of frequency* $\omega\delta/2$*. The Blaschke product is determined by the (paired) zeros in the upper half frequency plane of a reflection transfer function of the etalon of Fig. 2.1. The arrows indicate the location of the real part* ($\mu_{nr} > 0$) *of the zeros:* $\mu_1 = 0.733 + 0.35i$*,* $\mu_2 = 2.158 + 0.192i$ *and* $\mu_3 = 3.591 + 0.024i$*. The same parameter set as in Figs. 2.2 and 2.3 is employed. The solid line represents* $\arg B(\omega)$ *using all three paired zeros. The phases* $\arg B(\omega)$ *determined only by* μ_1 *and* μ_2 *(dotted line) and* μ_1 *(dashed line), respectively, are also shown.*

location of the first zero and so on. In two iteration steps, we are able to locate the complex parts of the zeros with an error smaller than 1% compared to the exact values.

2.5.2 Phase-amplitude relations

We also calculated the amplitude from the phase using (2.27). To calculate the phase we have used (2.44). The modified KK relation between phase and amplitude is a subtracted relation. Therefore, we need a value for the amplitude at a single frequency. In our calculations we used the amplitude at zero frequency calculated with (2.44). To numerically evaluate the frequency integral in Eq. (2.27), we again used a three-point trapezoidal rule.

In Fig 2.6 we have plotted the numerical calculated amplitude (dashed

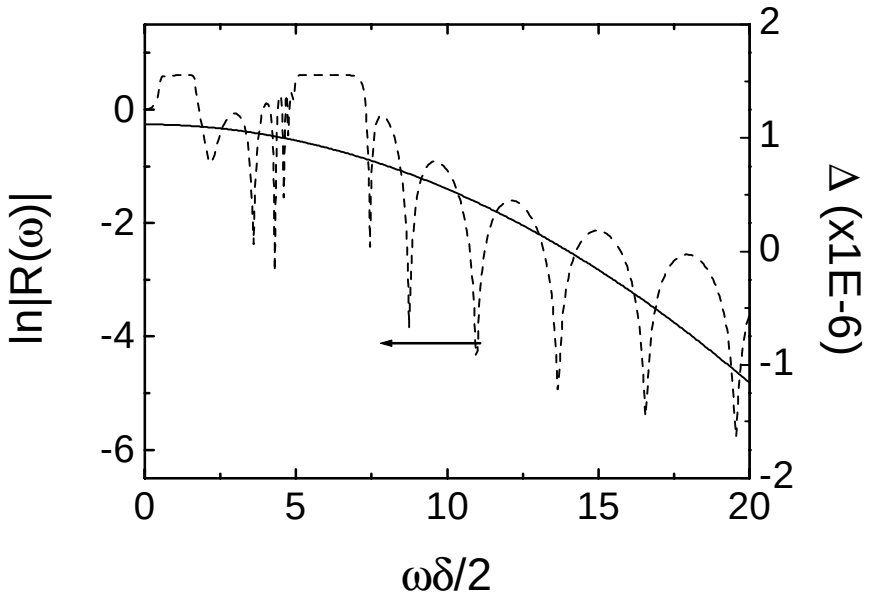

Figure 2.6: *The difference Δ (solid line) between the numerically calculated amplitude and the exact amplitude of a reflection transfer function $\mathcal{R}$ for the etalon of Fig. 2.1. The numerically computed amplitude (dashed line) results from a subtracted amplitude-phase KK relation. The same parameters are used as in the preceding figures.*

line) as function of frequency. To compare the result with the true amplitude calculated using the transfer function (2.44), we also plotted the difference Δ between the numerical result and the true amplitude (solid line). From the difference we see that we obtained excellent agreement to within 10^{-6}. In fact, the agreement is four orders of magnitude better than the calculations for the phase described in the previous section.

2.6 Transfer functions for interferometers in literature

Transfer functions formulated in literature often do not satisfy KK relations between amplitude and phase. As an example, Beck et al. [7] claimed that the GT interferometer does not satisfy a KK relation between amplitude and phase. They consider an etalon with a non-absorbing film with real index of refraction $n(\neq 1)$ and a high reflectivity mirror ($r_{23} = 1$). The transfer

function studied, is given by

$$H_B(\omega) = \frac{-r_{12} + \exp(-i\omega n\delta)}{1 - r_{12}\exp(-i\omega n\delta)}. \tag{2.48}$$

This expression can also be found in many standard textbooks [8]. As the optical parameters r_{12}, r_{23} and n do not depend on frequency, they individually do not obey a KK relation and therefore (2.48) does not represent a physical transfer function. (Besides, note that the sign convention used here is such that (2.48) is analytic in the lower half frequency plane.) The amplitude of this transfer function $|H_B(\omega)| = 1$, but the phase shows a strong frequency dependence. Beck et al. concluded that no KK relation holds between amplitude and phase, because the transfer function (2.48) has zeros in the lower half frequency plane. We have described above how to properly account for the occurrence of zeros of transfer functions in order to correctly apply KK relations. In addition, we have shown by example that using the full frequency dependence of the index of refraction n and the Fresnel coefficients r_{12} and r_{23} one will obtain a physical transfer function.

2.7 Conclusions

We have clarified that KK relations between the amplitude and phase of transfer functions exist for both the etalon and the GT interferometer. Comparing our description of transfer functions with the ones given in literature, the full frequency dependence of all relevant optical parameters has to be incorporated in order to apply KK relations. In addition, we have demonstrated how to properly account for the presence of zeros in transfer functions. However, we have also elucidated the complications in the use of KK relations in experimental situations. To be able to use these relations the real or complex part of the response function has to be known over a large frequency interval and some information on the presence of the zeros. In experimental situations, often this information is not available. Therefore, an experimental technique to measure the full complex response function would be far more superior. In the next chapter, a method which enables us to measure this will be described.

Chapter 3

Phase-sensitive interferometry with ultrashort optical pulses

In the previous chapter we discussed the determination of full response functions, i.e. the determination of the real and imaginary parts of response functions. In this chapter we report a novel method, from which the full response function, usually called transfer functions in optics, of the system under study is directly obtained. In this method use is made of a commercially available Fourier-transform spectrometer operating from infrared up to the UV part of the spectrum in combination with a fixed Mach-Zehnder at the front end. The technique provides a reliable spectroscopic tool to perform phase-sensitive time-resolved interferometry over a wide spectral range, which will be demonstrated experimentally in this chapter by measuring the full transfer function of an interferometer.

3.1 Introduction

Our approach for measuring transfer functions is similar to the method already used by Michelson [3]. In this method the transfer function is measured by using a Michelson interferometer with the sample under investigation in one of the arms. In an experiment, the interferometric cross-correlation signal between the light fields of both arms is recorded as function of path-length difference between both arms in the interferometer. From this cross-correlation signal, both the real and imaginary parts of the transfer function are obtained simultaneously.

Long after Michelson, this method became a field of interest again in

Fourier Transform Infrared spectroscopy [23]. The renewed interest is in the field of ultrashort pulse generation [24]-[29], because the method allows for a precise pulse evaluation of both intensity and phase, after the pulse has traveled through optical components. The phase is related to the chirp, a quantity often used in the field of ultrashort pulse generation. The chirp $\omega(t)$ is a measure for the instantaneous frequency of the pulse and can be calculated from the phase using $\omega(t) = d\phi(t)/dt$ (see for instance [25]).

Generally, in a pump-probe type of set-up the time resolution is determined by the time duration of the pulses and the shortest reliable time scale in these type of experiments is in the order of the pulse width. However, in the novel method we attain a time resolution which is an order of magnitude better than the pulse duration as we will discuss in more detail later on in this chapter. In itself it is not surprising that using this method such a short time resolution can be achieved. An example which demonstrates this very clearly are the experiments performed by Naganuma et al. [27]-[29] who used white-light sources to perform time resolved interferometry. In these experiments a time resolution of 5 fsec was achieved, equal to to correlation time of the source, although the source was continuous. This example shows that it is possible to obtain a time resolution which is very much shorter than the actual time duration of the "pulses" of the light source.

3.2 Experimental

3.2.1 The spectrometer

The experimental set-up to measure the interferogram of a double pulse is depicted in Fig. 3.1. As a light source to generate the ultrashort-optical pulses we used two different types of lasers in this thesis. The first type of laser we used is a colliding-pulse mode-locked (CPM) laser producing pulses with a duration of 60 fs at a fixed wavelength (630 nm). The day-to-day average value of the bandwidth-time interval product varied between 1.0-1.3 which results in a bandwidth of approximately 20 nm. The bandwidth-interval depends on the alignment of the laser and the DODCI dye used to modelock the laser. The alignment was very difficult to reproduce from day-to-day and DODCI dye appeared to be very sensitive to aging. The other laser we used was a Ti:Sa-laser, which is a solid-state laser and did not exhibit to above mentioned disadvantages. The central wavelength at which the pulses are generated is not

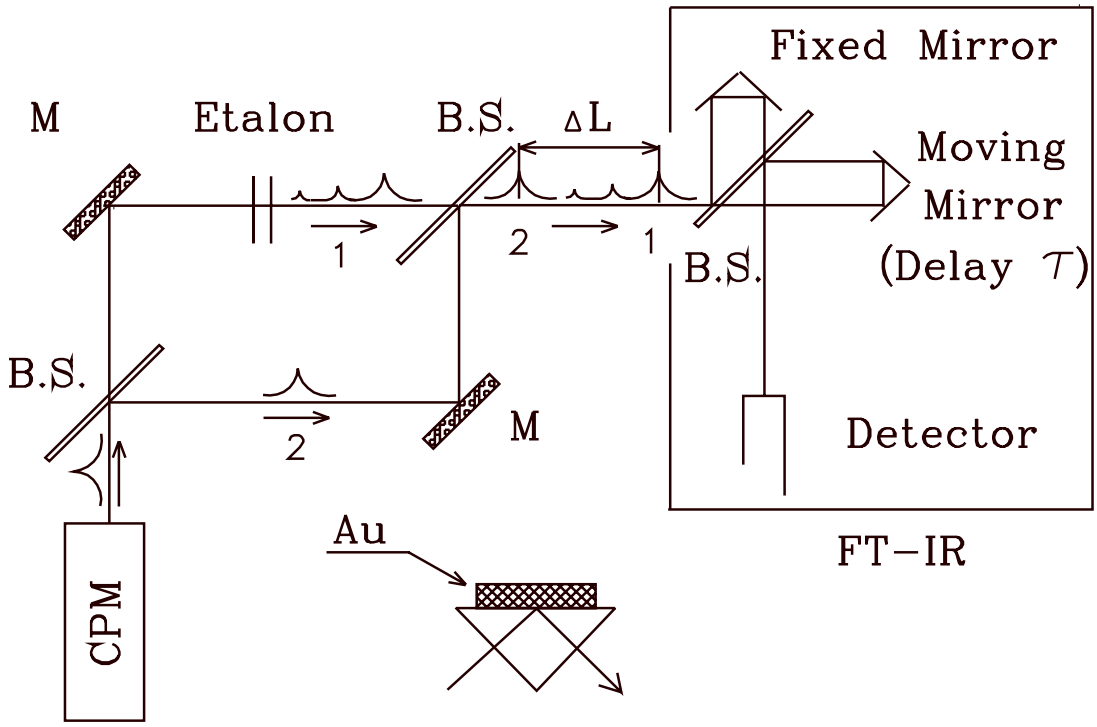

Figure 3.1: *Experimental set-up for time-resolved measuring of pulse distortion. It consists of a fixed Mach-Zehnder interferometer and a scanning Michelson interferometer. CPM: colliding pulse modelocked dye laser, B.S.: beamsplitter, M: mirror, FT-IR: Fourier-transform spectrometer.*

fixed but could be adjusted between 750-950 nm. Another advantage of the Ti:Sa-laser is that it appeared to be much more stable in intensity compared to the CPM laser for a much longer time. Last but not least is the very high power of the Ti:Sa-laser (upto 1 Watt) compared to the CPM-laser (30 mWatts). The experiments we describe in this chapter are performed using the CPM-laser simply because at the time of these experiments the Ti:Sa-laser was not available.

In an experiment a pulse from the laser is sent through a *fixed*-length Mach-Zehnder interferometer to create a double pulse. The difference in path length ΔL in the Mach-Zehnder interferometer is chosen such that, $\Delta L/c > T$, where T is the typical time duration of the pulses.

Both pulses are sent into a *scanning* Michelson interferometer and we record the interferometric autocorrelation function, which contains three peaks,

as will be shown in the next section. Two of these peaks are the cross-correlation functions between the first and second peak and vice versa. In the experiments we use a commercially available spectrometer as a scanning Michelson interferometer. In this section we explain our set-up.

As the spectrometer we use a Biorad FTS 60 A FT-IR spectrometer. In normal operation the spectrometer is used to perform absorption spectroscopy using an internal light source. In order to measure an interferometric auto-correlation function of the double pulse the source is disabled and pulses are coupled into the spectrometer through an emission port. The Michelson interferometer in this spectrometer is sealed. Therefore we cannot put the sample in the Michelson interferometer and simply measure the cross-correlation trace between an undistorted and distorted pulse. This is one of the reasons for using the Mach-Zehnder interferometer at the front end to be able to measure the cross-correlation function. The other reason is that in this way it is possible to use the extremely high time resolution of the spectrometer, which is difficult to achieve in a home-build set-up.

In the interferometer one mirror is fixed and the other travels over a maximum distance of 8 cm. A He-Ne laser beam which is sent through the interferometer in order to be able to measure the traveled path length of the moving mirror. The traveled path length is measured by counting the He-Ne laser fringes. The distance between the fringes is known and used as calibration of the traveled path length of the moving mirror. The highest resolution of the spectrometer is a step of the moving mirror of 1/8 of the He-Ne laser wavelength, which corresponds with a time resolution of 0.26 fs.

The He-Ne beam which passes through the interferometer is expanded before entering the Michelson interferometer. After passing the interferometer the He-Ne beam is detected by three detectors at three different positions in the beam profile. If the moving mirror is traveling at a constant speed, the three detectors detect a modulated light beam, and the electric output of the detectors are cosine waves. If the interferometer is accurately aligned, the phases of the cosine waves are the same. If the phases are not the same, piezoelectric actuators on the fixed mirror in the interferometer align the fixed mirror to lock the phases on the three detectors. This process, known as dynamic alignment, keeps the interferometer accurately aligned during a scan and makes the measurements highly reproducible. Therefore it is possible to average over several scans.

3.2.2 Mathematical formulation of the technique

In an experiment, the sample under investigation is placed in one of the arms of the fixed Mach-Zehnder interferometer. Therefore one of the two pulses coming out of the Mach-Zehnder interferometer is distorted by the sample under investigation, and is referred to as the signal pulse. In general this pulse can be written as a convolution as shown in the previous chapter (see Eq. (2.3)). The pulse from the other arm remains unaltered and will be referred to as the reference pulse. The field leaving the Mach-Zehnder interferometer is given by:

$$E(t, \Delta L/c) = P_r(t) + P_s(t + \Delta L/c). \tag{3.1}$$

Here $P_r(t)$ and $P_s(t)$ describe the field of the reference and signal pulse respectively. These two pulses are sent into a Michelson interferometer. Using the Michelson interferometer the autocorrelation function is recorded, as function of delay τ in the interferometer. The field on the detector behind the Michelson as function of time is given by:

$$\begin{aligned} E(t, \Delta L/c, \tau) &= P_r(t) + P_s(t + \Delta L/c) + \\ &\quad P_r(t + \tau) + P_s(t + \Delta L/c + \tau), \end{aligned} \tag{3.2}$$

where the first line in the right hand side describes the two pulses from the fixed arm of the Michelson interferometer and the second line in the right hand side the pulses from the moving arm at delay τ. Here we used that both interferometers in the set-up are balanced. This balancing means that the intensities coming out of both arms of one of the interferometers are equal. Therefore, no factors resulting from the beamsplitters in the interferometers appear in the above equation. Eq. (3.2) describes be the situation for one pulse, which is sent into the set-up. In reality, the CPM-laser produces pulses at a repetition rate of 90 Mhz. So a whole pulse train is sent into the Mach-Zehnder interferometer, where the separation of the pulse is $T_{rep} \approx 10$ ns, so the total field resulting on the detector is given by:

$$\begin{aligned} E_{tot}(t, \Delta L/c, \tau) &= \sum_{n=-\infty}^{\infty} P_r(t + n\Delta t) + P_s(t + \Delta L/c + nT_{rep}) + \\ &\quad P_r(t + \tau + nT_{rep}) + P_s(t + \Delta L/c + \tau + nT_{rep}). \end{aligned} \tag{3.3}$$

The sum in this equation represents the repetition rate of the laser. The total field generated by the laser is a sum over identical pulses.

The signal detected by the detector is an intensity. This intensity can be calculated from Eq. (3.3) to be:

$$\begin{aligned} I(\Delta L/c,\tau) &= \frac{1}{\Delta t}\int_{-\Delta t/2}^{\Delta t/2} dt |E_{tot}(t,\Delta L/c,\tau)|^2 = \\ & \sum_{n,m=-\infty}^{\infty} \frac{1}{\Delta t}\int_{-\Delta t/2}^{\Delta t/2} dt \Big\{ P_r(t+nT_{rep}) + P_s(t+\Delta L/c+nT_{rep}) + \\ & P_r(t+\tau+nT_{rep}) + P_s(t+\Delta L/c+\tau+nT_{rep}) \Big\} \\ & \Big\{ P_r(t+mT_{rep}) + P_s(t+\Delta L/c+mT_{rep}) + \\ & P_r(t+\tau+mT_{rep}) + P_s(t+\Delta L/c+\tau+mT_{rep}) \Big\}^*, \end{aligned} \tag{3.4}$$

where $*$ stands for complex conjugation. We have to integrate the intensity $|E_{tot}(t,\Delta L/c,\tau)|^2$ over time, because for one delay τ the intensity detected is an average over the integration time of the detector. To calculate this average intensity, applying a time interval of the integration time of the detector or a time interval equal to the time between two pulses coming out of the laser will lead to the same result.

Eq. (3.4) can be simplified by making an estimation of the different time scales involved. The scan length of the Michelson interferometer is of the order of cm, which corresponds to a typical time scale τ of picoseconds. This is very much shorter than the repetition rate of the laser so $\tau < T_{rep}$. But the scan length is long enough to resolve the full signal pulse, which has a typical width T which is in the order of femtoseconds, so $T < \tau < T_{rep}$. All the terms in the integrand of Eq. (3.4) are products of two pulses and only contribute to the integral if both pulses in this product overlap in time. Together with our estimation of the time scales, we can conclude that only terms with $n = m$ contribute to the integral. Using this knowledge we will find an expression if we write out all contributing terms, which consists out of correlation functions and squared single pulses. The correlation functions are the terms containing terms: $P(t)P^*(t+\tau)$ and the squared pulses are the terms: $P(t)P^*(t)$. The latter contribute a DC component to the recorded signal, whereas the correlation functions contribute a slow modulation in the average intensity on the DC component as function of delay in the Michelson interferometer. If we collect all terms contributing to the DC component into a

term referred to as DC and expand the correlation functions, we finally obtain:

$$\begin{aligned} I(\Delta L/c,\tau) \quad \propto \quad & DC + 2\frac{1}{\Delta t}\int_{-\Delta t/2}^{\Delta t/2} dt \\ & \Big\{ P_r(t)P_r^*(t+\tau) + P_s(t)P_s^*(t+\tau) + \\ & P_r(t)P_s^*(t+\Delta L/c+\tau) + P_s(t+\Delta L/c)P_r^*(t+\tau) \Big\}. \end{aligned} \tag{3.5}$$

Let us discuss the several terms in the above integral. The first two terms are field autocorrelation functions of the signal and the reference pulse. These autocorrelation functions are centered around zero delay ($\tau = 0$). The remaining two terms are cross-correlation functions between the reference pulse and signal pulse, and are centered around $\tau = \pm\Delta L/c$. The two cross-correlation functions contain the same information. The difference is in the time delay ($\Delta L/c$) and the time direction. This can easily be seen by substituting $t = t' - \tau$ in one of the cross-correlation functions, which shows that the time direction τ, is opposite in both cross-correlation functions.

The cross-correlation functions and autocorrelation functions are separated in time, because the delay introduced by the Mach-Zehnder interferometer is larger than the typical time duration of the pulses. Due to this separation in time of the different correlation functions it is easy to distinguish between autocorrelation and cross-correlation functions in a measurement. In the argumentation up to now, the situation is discussed when ultrashort optical pulses are used. However, the same arguments also apply to incoherent light sources [27]-[28]. For our method to be applicable it is necessary that the coherence length of the incoherent light source is shorter than $\Delta L/c$ otherwise it would not be possible to make the distinction between cross-correlation and autocorrelation functions.

In the experiments the signal is DC filtered, so we only record the AC component. Fig. 3.2, shows schematically how a result of such a measurement should look. The response of the detector $I(\Delta L/c,\tau)$ is indicated as a function of time delay in the Michelson interferometer. As expected the interferogram contains three peaks. The central peak corresponds to the sum of the autocorrelation functions, while the most left and most right peaks in Fig. 3.2 correspond to the cross-correlation functions.

Let us consider one of the cross-correlation functions:

$$C(\Delta L/c,\tau) \propto \frac{1}{\Delta t}\int_{-\Delta t/2}^{\Delta t/2} dt P_s(t)P_r^*(t+\Delta L/c+\tau), \tag{3.6}$$

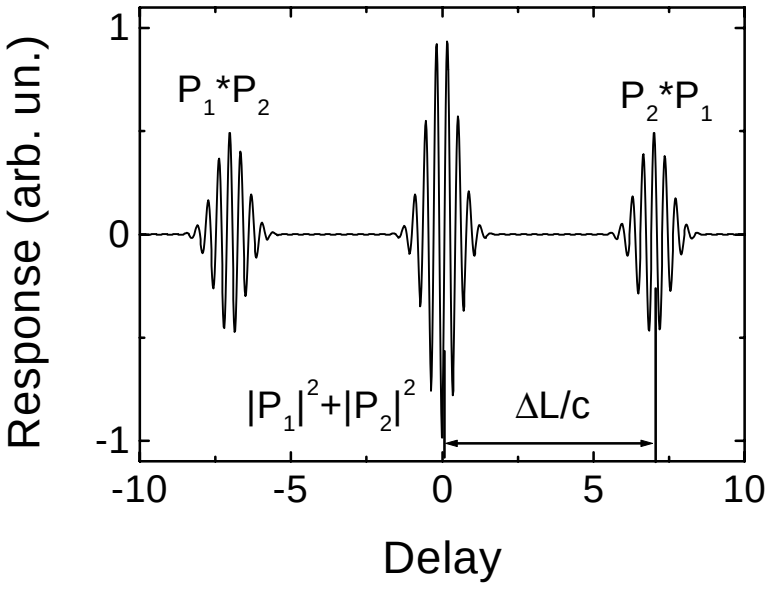

Figure 3.2: *A schematic plot of the response of the detector as function of time delay in the Michelson interferometer. The distance between the center of a cross-correlation trace and the center of the autocorrelation trace is given by the time delay between the two pulses ($\Delta L/c$) introduced by the fixed Mach-Zehnder interferometer.*

where the signal pulse is given by a convolution (see Eq. (2.3)). Substituting the convolution in (3.6) we find:

$$C(\Delta L/c,\tau) \propto \frac{1}{\Delta t}\int_{t=-\Delta t/2}^{\Delta t/2}\int_{-\infty}^{t} dt'dtH(t-t')P_r(t')P_r^*(t+\Delta L/c+\tau), \quad (3.7)$$

where $H(t-t')$ is the (amplitude) transfer function, describing the response of the sample placed in one of the arms of the interferometer. For simplicity we have dropped the wavevector dependence in our derivation similar to the derivation of the transfer function of the etalon in Chapter 2. To get more insight in this correlation function, we Fourier transform Eq. (3.7), which consists out of a correlation function of the reference pulse with the convolution integral. If we use the fact that a Fourier transform of an autocorrelation function is given by the amplitude squared of the Fourier transform of the underlying function, we obtain:

$$C(\omega,\Delta L/c) = |P_r(\omega)|^2 H[\omega+i\varepsilon]e^{-i\omega\Delta L/c}. \quad (3.8)$$

Here we see the appearance of the Fourier-Laplace transform of the transfer function. The Fourier-Laplace transform comes in by employing Eq. (2.4).

Apart from the constant factor $\exp(i\omega\Delta L/c)$, Eq. (3.8) is the product of the power spectrum of the reference pulse $|P_r(\omega)|^2$ and the transfer function $H[\omega + i\varepsilon]$ which describes the pulse distortion. Once $P_r(\omega)$ is known by for instance analyzing an undisturbed pulse, the full transfer function of the sample can be reconstructed from the measured cross-correlation signal. This is similar to the conventional practice of using a Fourier transform technique where two measurements are required in order to obtain the wavelength-dependent transmission of a sample. One measurement has to be performed to know the power spectrum of the source, a second measurement is needed to record the wavelength-dependent transmission. The difference between the common practice for measuring the wavelength-dependend transmission of a sample and our technique is in the obtained information about the transfer function. In a conventional transmission measurement, only information is obtained about the amplitude of the transfer function: $|H[\omega + i\varepsilon]|$ and no direct information about the dispersion of the sample. However, using the technique introduced in this chapter, one obtains the full complex transfer function, i.e. both the absorption and dispersion in one measurement.

In principle, both the phase and the amplitude of the transfer function of a sample are determined using this method. Practically, the reconstructed phase has a trivial uncertainty. The measured phase is the phase difference between the phases of the pulses from both arms of the interferometer. In the ideal case the phases resulting from the pulses $P(t)$ and $P^*(t)$ cancel exactly and we are only sensitive to the phase of the transfer function. In case of a slight unbalance in the Mach-Zehnder interferometer there will be an arbitrary offset in the phase.

The separation $\Delta L/c$ introduced by the Mach-Zehnder interferometer results in the factor $\exp(i\omega\Delta L/c)$ in Eq. (3.8). This factor represents an apparent additional phase which depends linearly on the frequency. This additional phase is independent of the sample, but only depends on the path length difference in the Mach-Zehnder interferometer. For an accurate determination of the phase induced by the sample, we have to know the center of the cross-correlation function which defines $\Delta L/c$. The transfer function of the sample also contains a phase which depends linearly on frequency and is related to the optical path length of the sample. The change in distance between the center of the interferogram and the center of the cross-correlation function of

a measurement with and without a sample in one of the arms of the interferometer is a measure for the change in the optical path length due to the sample. From this optical path length together with the length of the sample, we can determine the introduced group velocity and the index of refraction. The above described procedure for measuring the index of refraction, has been used to determine the index of refraction of supercritical CO_2 as function of pressure of the gas [30]. It appeared that the center of the cross-correlation function $\Delta L/c$ could be determined with an uncertainty as small as 10 fs. The error in the determination of the index of refraction using the above described procedure was shown to be in the order of 10^{-4}. Of course, the error in the determination of the index of refraction strongly depends on the error in the determination of the length of the sample.

In our discussion in chapter 2 of the Amplitude-Phase relations we considered the case that no absorption anomalies, as indicated in the literature [18] are present in the transfer function. These anomalies would give rise to extra terms in the phase and cannot be ruled out on mathematical grounds but more on physical grounds (see for instance [31]). One of the terms due to these anomalies which we did not include in our discussion is a term linear in frequency. In the literature it was already recognized that this term is due to a delay [32] and is exactly the term linear in frequency as discussed above.

3.2.3 Time resolution

In general, to obtain qualitative information about about the time resolutionTime resolution of an instrument, the response to an exponentially damped cosine is studied. This exponentially damped cosine is a physical transfer function, which has two relevant parameters. One parameter is the decay time of the exponent, the other the frequency of the cosine. Therefore there are two types of time resolution which can be defined for the method discussed in this chapter: a time resolution related to the amplitude of the light field and a frequency resolution as customary in normal spectroscopy.

The latter resolution is set completely by the spectrometer. The smallest wavelength one can detect using the spectrometer can be calculated from the smallest step of the moving mirror using so called Nyquist critical frequency (see for instance [33]). The Nyquist critical frequency defined by $\lambda_c = 1/2\Delta\tau$, gives the smallest wavelength (λ_c) that can be detected given a smallest step size of the moving mirror ($\Delta\tau$). For the used spectrometer the smallest wave-

length one can detect is $\lambda_c \approx 350$ nm.

The resolution related to the amplitude of the field appeared to be dependent on the functional form of the pulses used in the experiments. Below we will show experimentally that the pulse amplitude is a sech function with a decay time of 20 fs and that the long time behavior of the autocorrelation function of the sech function is exponential with a decay time of 20 fs.

To calculate analytically the response of the instrument to an exponentially damped cosine is to complicated. Therefore we studied the resolution by performing numerical calculations of Eq. (3.7). In these calculations we performed the convolution in the frequency domain (Eq. 3.8) and used a fast Fourier transform scheme to calculate the response of the instrument in the time domain. For the pulse $P(t)$ we used a measured pulse profile. To find the time resolution we varied the decay time of the exponentially damped cosine. As a definition for the time resolution we used the shortest decay time of the exponent for which we can see a elongation of the response of 10% (defined in FWHM fashion) compared to the response on a delta function in time. The time resolution found in this way was 5 fs which is in the order of the correlation time of the source. The decay time observed in an experiment is longer and the actual constant of the decay can be found by deconvoluting the measured instrumental response function. We found that if the decay time of the exponent is longer that the decay time of the sech function, that no deconvolution is necessary and the decay time observed in the instrumental response is the actual decay time of the exponent.

3.3 Experimental results

3.3.1 Interferometric autocorrelation function

To know the spectral content of the pulses, the interferometric autocorrelation function of an undistorted CPM pulse is recorded as function of time. Data points are measured at every 80 nm mirror displacement, which corresponds to a time resolution of 0.3 fs. The software provided with the spectrometer measures the time resolution relative to the He-Ne fringes. The parameter to set the time resolution is called under sampling rate (UDR), which is set in our case to 0.25, meaning that four points are measured in between two zero crossings of the He-Ne laser. The total scan range of the moving mirror of the spectrometer is set by the inverse scan range, the reason being that this

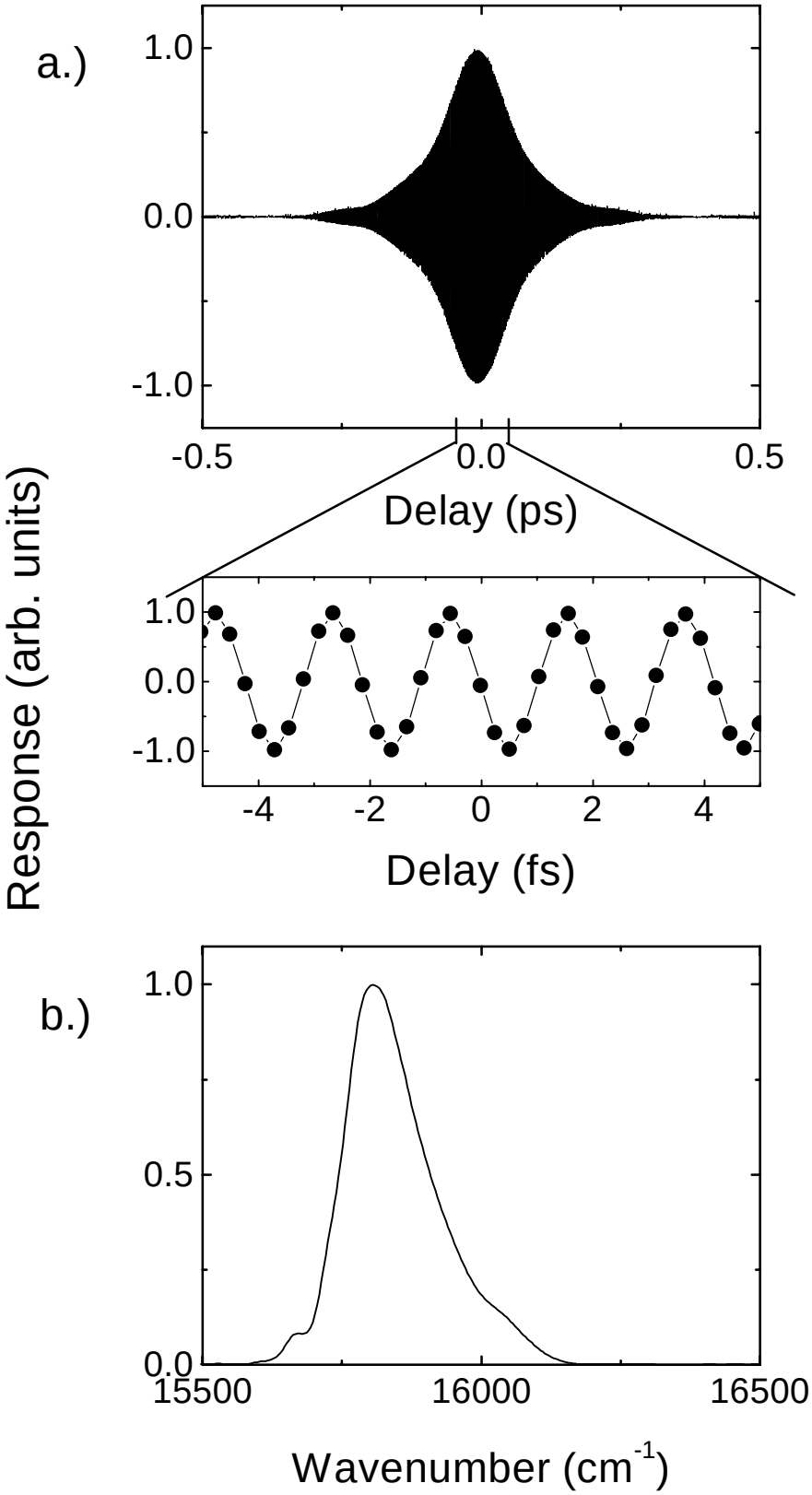
a.)
1.0
0.0
-1.0
-0.5
0.0
0.5
Delay (ps)
1.0
0.0
-1.0
-4
-2
0
2
4
Delay (fs)
Response (arb. units)
b.)
1.0
0.5
0.0
15500
16000
16500
Wavenumber (cm-1)

Figure 3.3: *a.) A typical result of a measurement of the autocorrelation function of an undistorted pulse. An enlarged part of the measured autocorrelation function is plotted, showing the resolved fringes in the sampled autocorrelation function. The dots in this figure correspond to data points sampled by the interferometer, the solid line is a guide to the eye. (b) The spectrum of the pulse, which is the Fourier transform of the interferometric autocorrelation function.*

parameter sets the resolution in the frequency domain. The interferometric autocorrelation function was measured with an inverse scan range of 32 cm^{-1} and an average of 256 scans is recorded.

A typical result of an interferometric autocorrelation function of an undistorted CPM pulse is shown in Fig. 3.3a. In this figure the response of the detector is plotted as function of the delay in the Michelson interferometer between the pulse and its copy. The inset shows a small part of the interferogram and illustrates the optical fringes in the interferogram. The points in this figure are the measured data points, and the solid line is a guide to the eye. The Fourier transform of the pulse is shown in Fig. 3.3b, where we plotted the response as a function of wavenumber.

From the interferometric autocorrelation function we can also gain information about the pulse functional form in the time domain. However, it is not possible to calculate the original pulse profile form an autocorrelation function uniquely. Therefore, a pulse profile must be assumed, and fitted to the measured autocorrelation function. We performed this fit procedure on the amplitude of the autocorrelation function showed in Fig. 3.3, where we first calculated the amplitude of the autocorrelation function by Fourier transforming the autocorrelation function, shift it to zero frequency and Fourier transforming it back to the time domain. The result of this is shown in Fig. 3.4 (solid line) where we have plotted the amplitude of the autocorrelation function logarithmically as function of time. To find the pulse profile we tried two functional forms: a Gaussian pulse profile and a sech function (respectively the dotted and the dashed lines in Fig. 3.4). We clearly see that the autocorrelation function can be described very accurately over almost four orders of magnitude by assuming a sech function for the pulse profile, whereas the fit assuming a Gaussian pulse profile is much poorer. The autocorrelation shown for the sech function in Fig. 3.4 was calculated numerically, using a decay time of 40 fs in the sech function. The pulse duration found from this sech function was 200

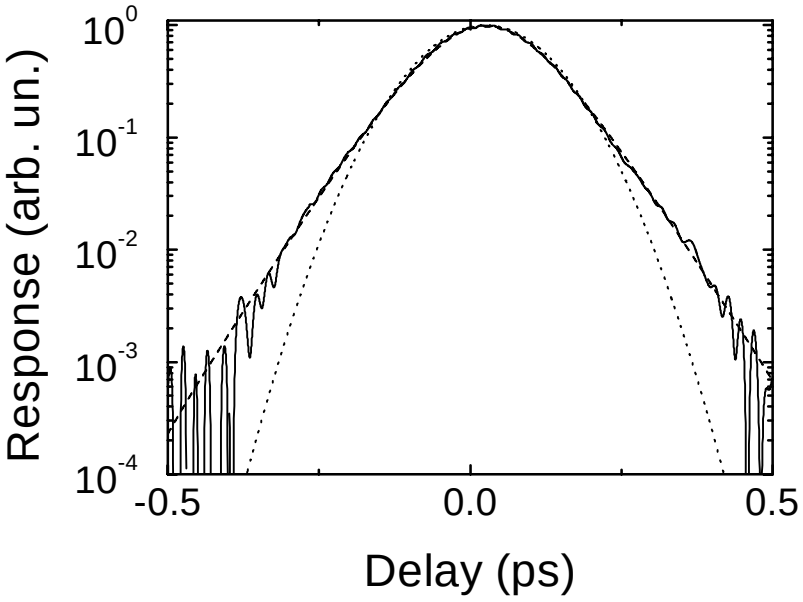

Figure 3.4: *The amplitude of the autocorrelation function shown in Fig. 3.3 plotted logarithmically as function of time (solid line). We fitted the autocorrelation function assuming a Gaussian (dotted line) and a sech function (dashed line).*

fs (FWHM).

An analytic expression for the autocorrelation function of a sech function is not available to our knowledge. So we cannot analyze the autocorrelation function analytically to gain for instance information on the long time behavior. However, from Fig. 3.4 we clearly observe that the autocorrelation function exhibits exponential behavior for long times. The decay time appeared to be equal to the decay time of the sech function.

3.3.2 Etalon

The transmission characteristics of an etalon is well-known and understood (see previous chapter), therefore we could check the accuracy of the technique introduced in this chapter by measuring the total transfer function of an etalon in transmission. The etalon was placed in one of the arms in the Mach-Zehnder interferometer, and the light from the Mach-Zehnder interferometer was sent into the spectrometer through its emission port. We measured the interfer-

ogram with a time resolution of 0.3 fs (UDR=0.25). The total inverse scan range of the moving mirror was 8 cm^{-1}.

A typical result of the autocorrelation function of the double pulse with one of the pulses transmitted through the etalon is shown in Fig. 3.5a. In this figure we see the three peak structure mentioned earlier. The left and right peak are the cross-correlation functions between the chirped pulse and the undistorted pulse. The central peak is the sum of the autocorrelation functions of the chirped pulse and the undistorted pulse.

In Fig. 3.5b we show the Fourier transform of one of the cross-correlation functions. If we look at the spectral content of the cross-correlation function and compare this to Fig. 3.3b, we see a sharply peaked spectrum. The sharply peaked spectrum is a manifestation of the wavelength-dependent transmission through the etalon. We can extract the separation between the reflecting surfaces in the etalon from the separation between the copies of the pulse in the cross-correlation function and find it to be $\delta = 73 \pm 5$ μm. The estimated error of $\pm$ 5μm agrees with the estimated accuracy of 10 fs estimated in the earlier mentioned experiments where the index of refraction of supercritical CO_2 was measured [30]. From the ratio of the height of the peaks we estimate the reflection coefficient of one reflecting surface in the etalon to be $r = 0.6 \pm 0.02$.

To check the obtained parameters using the introduced method, we also performed an independent measurement. In this independent measurement we recorded the transmission through the etalon using the FT-IR spectrometer in normal operation. The etalon was placed in the sample compartment, and an interferogram is measured of the transmitted light through the etalon. From the height of the peaks in this interferogram the reflection coefficient r was obtained and found to be: $r = 0.6 \pm 0.02$. From the distance of the peaks in the Fourier transform of the interferogram. the spacing of the etalon was determined for which we found: $\delta = 74 \pm 5$ μm. These values are in excellent agreement with those found earlier using the cross-correlation technique.

In Fig. 3.5b the argument of the complex Fourier transform of the measured cross-correlation function is also shown. This argument is the phase difference between the two pulses of the Mach-Zehnder interferometer, as shown in the previous section and determines the phase of the transfer function. The only unknown quantity is the arbitrary off-set in the measured phase. This result is directly obtained from the measured cross-correlation transform, so no use is made of the Kramers-Kronig relations between amplitude and phase.

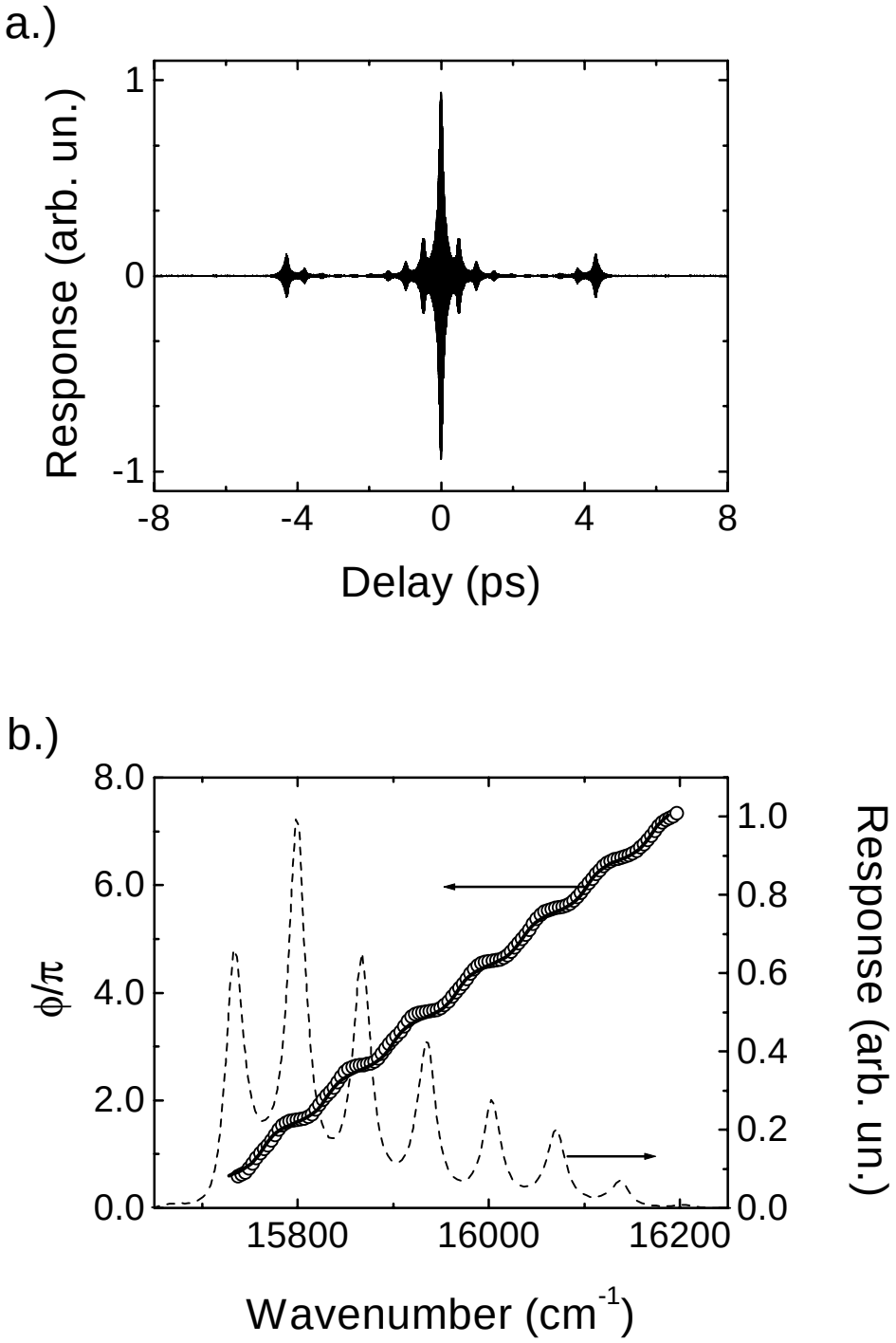

Figure 3.5: *(a) Measured autocorrelation function of the double pulse with an etalon as a dispersive medium. (b) The spectrum of the right cross-correlation function indicated by the dashed line (right axis). The solid line in this figure is the theoretical prediction of the phase (left axis). The circles are the measured data.*

The time direction of the phase on the pulse was determined by keeping track which path in the Mach-Zehnder interferometer is longer.

To be able to make a unbiased comparison between argument of the transfer function obtained experimentally and results found based on a calculation using the transfer function (2.45), we performed a fit procedure using only two parameters. One parameter is the arbitrary off-set for the phase. The center of the cross-correlation function ($\Delta L/c$) was determined by calculating the geometrical 'center of mass' of the cross-correlation function with respect to the center of the interferogram. The other fit parameter is a correction to the slope which comes from the uncertainty in $\Delta L/c$. The transfer function and the experimentally obtained parameters obtained from both measurements described above enables us to calculate the complex valued transfer function of the etalon. The solid line in Fig. 3.5b is the result of the best numerical fit of the phase using the above described procedure. If we compare the experimental result with the result obtained from theory, we see an excellent agreement. The mean difference between the obtained experimental results and the solid line is used as an estimate for the accuracy in the determination of the phase and is found to be be 0.15 rad. Often in experimental situations the transfer function is not known in advance and we can only rely on the experimentally obtained complex valued transfer function.

In the previous chapter we have shown that the transfer function of an etalon can exhibit zeros. We discussed that from an experimental point of view, it is very difficult to obtain the complete transfer function by measuring the amplitude of the transfer function as function of wavelength and applying amplitude-phase relations. Besides the fact that we have to know the location of the zeros of the transfer function on fore hand, we have to know the amplitude over a large frequency interval. With the introduced method in this chapter, the total transfer function can be measured even in a limited frequency interval. Contrary to the methods discussed in the previous chapter, no information about the transfer function is needed on forehand.

3.4 Discussion and conclusions

We have introduced a novel method, based on a commercially available Fourier Transform spectrometer, to perform phase-sensitive time-resolved interferometry. The method is similar to the method introduced by Michelson [3] and Naganuma [27]-[29]. With this method it is possible to measure the spectrum

and the detailed phase dependence, introduced by an absorbing and dispersive sample. This is demonstrated using ultrashort laser pulses in the visible range of the spectrum.

Advantage of the method is the simplicity of the experimental set-up. The dynamic alignment of the spectrometer makes the method highly reproducible and enables averaging over many scans.

In normal operation the spectrometer is used with an internal light source to perform e.g. absorption and transmission spectroscopy in the infra red and visible part of the spectrum. In order to measure an interferometric autocorrelation function, the internal source is disabled and pulsed light is coupled into the spectrometer through an emission port.

We have introduced a novel spectroscopic tool measure the full transfer function, that is the real and imaginary part of a transfer function. This can be done over a limited frequency interval and no information is needed in advance about the transfer function.

In the here presented example of phase-sensitive interferometry, not all the possibilities of the method are used. For instance, it is also possible to do time resolved measurements. The time resolution in such a measurement is limited by the correlation time of the source. This correlation time is very much shorter then the time duration of the pulses, as we have shown. In the example presented in this chapter the time resolution was 5 fs whereas the time duration of the pulses was 70 fs. The method enables us to do measurements with much higher time resolution than obtainable with pump-probe based measurements. Time-resolved measurements at ultrashort time scales will be the subject of the study in the next chapter.

For very intense laser pulses, when non-linear optical effects start to play a role, a straight forward Fourier analysis of pulse propagation breaks down. A more elaborate analysis of the pulse distortion is required than, which should include a model to describe the non-linear part of the pulse dynamics. An example of this will be given in Chapter 5 of this thesis.

Chapter 4

Observation of breakdown of diffusion for propagation of light in random media

We present results of experiments on the transport of light through thin random media. Measurements of total transmission and time-resolved propagation were performed using strongly scattering samples of varying thickness L. The time-resolved measurements were performed, employing the new interferometric technique introduced in chapter 3. For $L/\ell < 8$, where ℓ is the transport mean free path, the observed decay times from the long-time exponential behavior exhibit strong deviations from diffusion theory and radiative transport theory, whereas the total transmission measurements do not. For the thinnest sample ($L/\ell \simeq 2$) a reduction of the diffusion coefficient with a factor of two was observed.

4.1 Introduction

The interest in the field of multiple scattering of classical waves in random media was initially led by the analogy with electron scattering in disordered metals. The observation of the counterpart for light of Anderson localization [34] was the ultimate goal and a lot of effort has been put to reach the experimental parameters to attain this effect. Very recently, in a paper by Wiersma et al [35] it was reported that localization of light was observed. During the search for localization of light, many other interesting phenomena in light scattering have since been investigated and observed, among others

weak localization and universal conductance fluctuations in light transmission [36, 37]. Recently, interest has arisen in medical imaging applications to determine optically the location of objects in strongly scattering biological tissues. Optical imaging may serve as an important substitute for X-ray based techniques as optical radiation is non-ionizing. Pulse transmission measurements on very short time scales already give promising results [38].

An exact description of propagation of light through a medium that scatters and absorbs is quite complicated. A tremendous simplification is obtained if the propagation can be described with radiative transfer theory, where all interference effects are neglected. If the sample size (L) is considerably larger than the transport mean free path ℓ, there will be no coherent beam left and the equation of radiative transfer reduces to a diffusion equation [39, 40]. The study of localization of light is concerned with the breakdown of diffusion theory and radiative transport theory for strongly scattering thick samples.

In this chapter we report on an observed breakdown of radiative transfer theory for relatively thin ($L/\ell < 8$) strongly scattering samples. For large thicknesses these samples behave according to diffusion theory. Using the new interferometric technique described in chapter 3 we studied the dynamics of light propagation in thin disordered samples and found surprisingly large deviations from time-dependent diffusion theory and radiative transfer theory. The diffusion coefficient following from the long-time exponential decay of the transmitted pulse appears to depend on the sample thickness and is considerably reduced for $L/\ell \simeq 2$.

4.2 Theory

4.2.1 Diffusion

Light propagating through disordered media is multiple scattered. An exact description of the transport of light through these media is very difficult. For instance, one has to include interference effects. If the disordered media are strongly scattering, the phase of the light is scrambled and interference effects can be neglected. Exception to this appeared to be the cones of enhanced backscattering from strongly scattering disordered media. These cones are due to interference exactly in the backscattering direction [42]. However for the transport through these samples, it was shown that it is a good approximation to neglect interference and a simplification can be achieved by describing the

transport of light through strongly scattering slabs by a diffusion equation [41]. In such a description, we assume that the light diffuses through the multiple scattering medium as particles through a random structure. The transport of light through these strongly scattering media will obey a diffusion equation. If we assume that the medium is translationally invariant in two directions, the diffusion equation will reduce to the one-dimensional case, in the direction that is not translationally invariant. This is similar to the transport of a layered medium, where the medium is translationally invariant in the layers and not perpendicular to the layers. We consider the case were this direction is the z-direction, in which case the diffusion equation is given by:

$$\frac{\partial I(z,t)}{\partial t} - D\frac{\partial^2 I(z,t)}{\partial z^2} = -T_{abs}^{-1} I(z,t), \tag{4.1}$$

where $I(z,t)$ is the diffuse intensity at place z and time t, D the diffusion constant and the term $T_{abs}^{-1} I(z,t)$ accounts for absorption.

To solve this equation, usually the imposed boundary conditions are $I(z=0,t)=0$ and $I(z=L_{\text{eff}},t)=0$, where the thickness L_{eff} is an effective slab thickness. This effective slab thickness is thicker than the actual thickness of the sample. The difference between L_{eff} and the physical thickness of the sample is the so called extrapolation length, describing the fact that the diffusive intensity is nonzero at the boundaries. Using these boundary conditions an exact solution to Eq. (4.1) can be found which we will not reproduce here. We will only discuss some characteristic features of the solution of interest for the experiments we performed. For the stationary case it follows from this solution that the transmission through a slab scales with ℓ/L. The time-resolved transmission, which can be calculated using the solution of (4.1), is an exponential decay [41] for the long-time tale behavior of a transmitted pulse.

4.2.2 Extrapolation length

When applying diffusion theory to finite samples, some refinements are required. To describe the fact that the diffusive intensity is actually nonzero at a boundary an extrapolation length [40, 43] $z_0 \sim \ell$ is introduced defining the effective slab thickness:

$$L_{\text{eff}} = L + 2z_0 \tag{4.2}$$

to be used in diffusion theory. To account for the influence of internal reflection due to the refractive index mismatch at the boundaries [44], the extrapolation

length has to be modified according to [45]:

$$z = z_0 \frac{1+\overline{R}}{1-\overline{R}}, \tag{4.3}$$

where $\overline{R}$ is the angle-averaged reflection coefficient at each boundary. The extrapolation length can also be incorporated in diffusion theory by modifying the boundary conditions of the diffusion equation [40, 44, 45]. For the stationary case and for isotropic scattering, solutions of the classical equation for radiative transfer also known as the Milne equation show [43] that the value of z_0 for an semi-infinite medium becomes smaller by only a few percent for slab thicknesses $2 \leq L/\ell \leq 16$. Comparison of numerical simulations with diffusion theory has shown [46] that the total transmission for varying L and $\overline{R}$ is very well described by the diffusion theory result

$$T = \frac{\ell + z}{L + 2z}, \tag{4.4}$$

in which $z_0 = 2\ell/3$ is to be used [40, 45].

For the time-resolved transmission similar arguments hold. Assuming that the light propagating through the disordered sample can be described by a diffusion process, the long-time exponential decay of the transmitted pulse is characterized [41] by a decay time τ_D:

$$1/\tau_D = \pi^2 D/L_{\text{eff}}^2, \tag{4.5}$$

where the effective sample size is given by $L_{\text{eff}} = L + 2z$. To obtain this solution, we neglected absorption. That this is a good approximation in our experiments will be discussed below.

4.2.3 Time-resolved intensity

The problem we face in describing our time-resolved experiments is that no explicit theoretical expression was known for the dynamic quantity we measure. Another problem is that using our interferometric approach, we measure field correlation functions and diffusion theory is a theory describing the transport of intensity. We will derive an expression in the time-place domain which represents the signal recorded with our new interferometric approach. It will be shown that the measured quantity in this chapter is an intensity which can be compared with diffusion theory. In the derivation we will use the

diffusion result based on a microscopic theory. To calculate the intensity inside the disordered medium we consider the intensity tensor $\langle G(t : \mathbf{r}, \mathbf{r}')G^*(t' : \mathbf{R}, \mathbf{R})\rangle$ averaged over disorder. The averaging over disorder is indicated by the brackets $\langle..\rangle$. If we neglect first-order scattering and only consider the ladder contributions it can be shown [47, 42] that the tensor has the following structure:

$$\langle G(t; \mathbf{r}, \mathbf{r}')G^*(t'; \mathbf{R}, \mathbf{R})\rangle = \Phi(t, t'; \mathbf{r}, \mathbf{r}')\delta(\mathbf{r} - \mathbf{R})\delta(\mathbf{r}' - \mathbf{R}'), \tag{4.6}$$

where $\Phi(t, t' : \mathbf{r}, \mathbf{r}')$ is a function to be determined below. If we consider infinite media, the averaging over the positions of the scatterers restores the translational symmetry in coordinate space. In that case we can write:

$$\Phi(t, t'; \mathbf{r}, \mathbf{r}') = \Phi(t, t'; \mathbf{r} - \mathbf{r}'). \tag{4.7}$$

We performed our measurements in the time domain.. Since time dependence is more easily handled in the frequency domain, we will introduce a frequency dependence $\Phi(\omega + \Omega/2, \omega - \Omega/2; \mathbf{q})$ analogous to [48]-[50], for which we can write the well known diffusion result for $\Omega \to 0$ and $\mathbf{q} \to 0$:

$$\Phi(\omega + \Omega/2, \omega - \Omega/2; \mathbf{q}) = \frac{1}{-i\Omega/v_E + \frac{1}{3}lq^2}, \tag{4.8}$$

where v_e is the effective velocity of light in the medium. The final step is to substitute this result into Eq. (4.6) and calculate the result in the time domain. We assume that Eq. (4.8) does not depend on frequency ω. Using this assumption, the Fourier transform of (4.6) with respect to ω contributes a delta function in time. So finally we are left with:

$$\langle G(t; \mathbf{r}, \mathbf{r}')G^*(t'; \mathbf{R}, \mathbf{R}')\rangle \propto$$

$$\delta(r - R)\delta(r' - R')\delta(t - t') \int\int d\Omega \; d\mathbf{q} \frac{1}{-i\Omega/v_E + 1/3lq^2} \mathrm{e}^{\mathrm{i}(\mathbf{r}-\mathbf{r}')\mathbf{q}} \mathrm{e}^{-\mathrm{i}\Omega \mathrm{t}}. \tag{4.9}$$

Calculating the integrals will give:

$$\langle G(t; \mathbf{r}, \mathbf{r}')G^*(t'; \mathbf{R}, \mathbf{R}')\rangle \propto$$

$$\delta(\mathbf{r} - \mathbf{R})\delta(\mathbf{r}' - \mathbf{R}')\delta(t - t') \frac{1}{(4\pi Dt)^{3/2}} \mathrm{e}^{-|\mathbf{r}-\mathbf{r}'|^2/(4\mathrm{Dt})}. \tag{4.10}$$

Summarizing we have calculated the diffusion result in the place-time domain, which we are going to use in the next section to calculate the recorded signal.

4.2.4 Pulse transmission measurements

In the dynamic measurements the transport of an ultrashort light pulse through a multiple scattering sample is studied employing the time-resolved technique described in chapter 3. The interferometrically measured cross-correlation function is related to a spatial amplitude-amplitude correlation function valid *inside* the sample, which can be written as:

$$C_{\mathbf{r}}(\Delta L/c) = \frac{1}{\Delta t}\int_{-\Delta t/2}^{\Delta t/2} dt P_{\mathrm{s}}(t;\mathbf{r})P_{\mathrm{r}}(t+\Delta L/c;\mathbf{r}), \tag{4.11}$$

where $\Delta L/c$ is the variable delay in the Michelson interferometer of the FT spectrometer, Δt is the integration time, and P_{r} and P_{s} are the reference and signal amplitudes, respectively. We use Eq. (4.11) as a starting point in our derivation of an expression representing the measured signal. For the signal amplitude we can write, using multiple scattering theory:

$$P_{\mathrm{s}}(t;\mathbf{r}) = \int\int_{-\infty}^{t} d\tau d\mathbf{r}' G(\tau;\mathbf{r},\mathbf{r}')S(\tau - t;\mathbf{r}'), \tag{4.12}$$

where $S(t,\mathbf{r})$ is a source term for which we will use a point source $S(t,\mathbf{r}) = j(t)\delta(\mathbf{r}-\mathbf{r}_{\mathrm{source}})$ with j having a Gaussian profile. This Gaussian profile represents the pulse from the Ti:Sapphire laser and is a good approximation for our experiments as will be shown. The amplitude P_{s} exhibits strong fluctuations as a function of position $\mathbf{r}$, which is a behavior known as speckle. The correlation function $C_{\mathbf{r}}(\Delta L/c)$ oscillates with a period of $\Delta L/c$. To eliminate both the speckles and the fringes, we have averaged the square of the cross-correlation function using 50 to 100 measurements by focusing the impinging pulse at different positions of the sample. In our experiments the measured object is:

$$C^{(2)}_{\mathbf{r}\mathbf{r}'}(\Delta L/c) \equiv C_{\mathbf{r}}(\Delta L/c)C_{\mathbf{r}'}(\Delta L/c),$$

For this average it can be shown using Eq (4.10) that it can be written as:

$$\left\langle C^{(2)}_{\mathbf{r}\mathbf{r}'}(\Delta L/c)\right\rangle \propto \frac{1}{\Delta t}\int_{-\Delta t/2}^{\Delta t/2} dt \exp\left\{-2\left(\frac{t+\Delta L/c}{\Delta\tau}\right)^2\right\} F(t;\mathbf{r},\mathbf{r}'), \tag{4.13}$$

with

$$F(t,\mathbf{r},\mathbf{r}') \propto \int_{-\infty}^{t} d\tau \exp\left\{-2\left(\frac{t-\tau}{\Delta\tau}\right)^2\right\}\Phi(\tau;\mathbf{r},\mathbf{r}'), \tag{4.14}$$

where the width of the incoming Gaussian pulse is $\Delta\tau$ ($\approx$ 70 fs in our experiments). From Eq. (4.14) we see that the signal intensity is a convolution of the incoming intensity with the average of the squared Green's function. The latter is a slowly varying function which can be related directly to results from diffusion theory [40, 41] and is the signal we measure in our experiments. Especially it follows that the long-time behavior, which is the function of interest in our experiments, can be described by Eq. (4.5).

4.3 Experimental

4.3.1 Sample preparation

The experiments were performed on strongly scattering samples made of TiO_2 particles (n $\approx$ 2.8) on the basis of commercial available rutile pigment. The particles have a size distribution of $d = 220 \pm 70$ nm. We prepared samples with a thickness ranging from 1.43 μm to 18 μm, covering a range where we expect that diffusion theory holds (thick samples) and strong deviations from diffusion theory can be expected (thin samples). The thickness of the samples was determined using a microscope and was measured on ten different positions. From these measurements both the thickness (mean value) and the uncertainty in the thickness (standard deviation) is determined. For all samples the estimated standard deviation of L was 0.3 μm.

4.3.2 Dynamic measurements

The set up used to perform the measurements is depicted schematically in Fig. 4.1. The set up is similar to the setup described in the previous chapter, with some minor modifications. As a light source we used a Ti:Sapphire-laser, which produced pulses with a duration of 70 fs and a central wavelength of 781 nm. These pulses are send into the *fixed* Mach-Zehnder interferometer. In one of the arms of this interferometer the disordered sample is placed between the two lenses (L1 and L2 in Fig. 4.1) that acts as a telescope. The first lens (L1) of this telescope has a focal length of 10 cm, the second (L2) which is used to collect the scattered light has a focal length of 2.5 cm. Using this telescope the coherent beam is collimated and compressed with a factor 4 in diameter. A large acceptance angle is also achieved, because of the small focal length of the second lens. In the other arm a Hinds photo-elastic modulator (PEM)

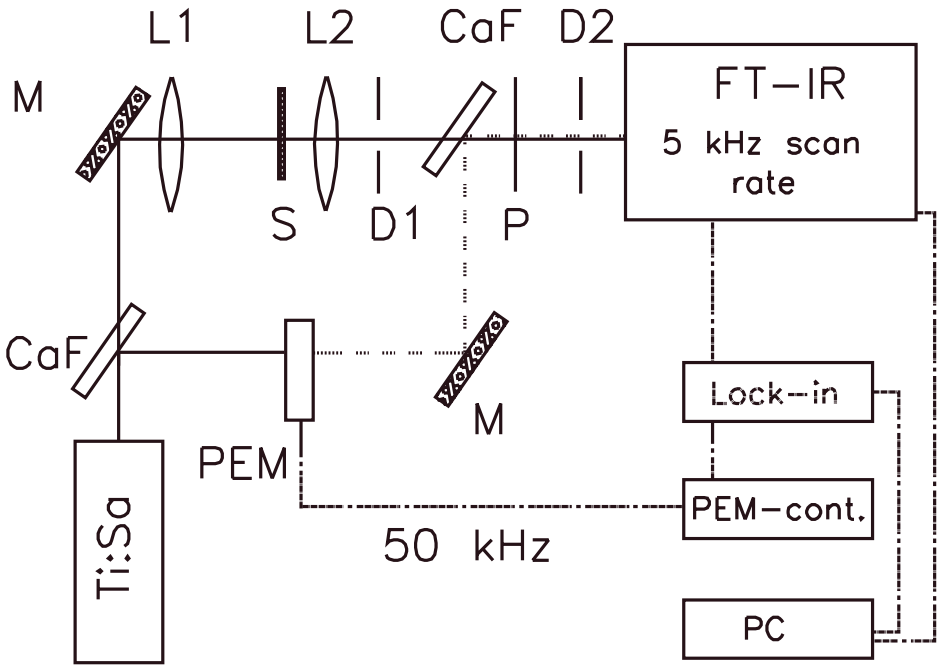

Figure 4.1: *The time-resolved pulse transmission set up. A 70 fs pulse train from a Ti:Sapphire laser is sent through a fixed Mach-Zehnder interferometer ¡ with the sample (S) in one of the arms. The cross-correlation function is recorded with a rapid scanning Fourier transform spectrometer (FT-IR). The reference beam is modulated with a photo-elastic modulator (PEM) and demodulated using a lock-in amplifier. The demodulated signal is stored in the computer (PC) and averaged over many sample configurations to obtain the cross-correlation function. Meaning other abbreviations used: CaF: Calcium Fluorite window, M: mirror, L: lens, D: diaphragm, P: polariser.*

is placed which modulates the linear polarized light into circular polarized at a modulation frequency of 50 kHz. Emanating from the Mach-Zehnder interferometer are a scattered pulse referred to as the signal pulse and an unscattered modulated pulse referred to as the reference pulse, separated by a time τ. This separation in time is chosen such that $\tau > T$, where T is the typical time duration of the signal pulses.

Behind the Mach-Zehnder interferometer a polarizer aligned parallel to the incoming polarization is placed. Due to this polarizer, the circularly modulated reference pulse becomes an amplitude modulated pulse at a frequency

of 100kHz. Furthermore this polarizer selects the polarization channel of the scattered light parallel to the polarization of the incoming light. A spectrometer (Bio-rad FTS 60A) is used to measure the interferometric autocorrelation function of this pulse pair, which is basically a *scanning* Michelson interferometer. The necessary stability and reproducibility to perform an interferometric measurement is provided by this sealed and dynamically aligned scanning spectrometer enabling us to do time-resolved measurements as shown in chapter 3.

Between the Mach-Zehnder interferometer and the spectrometer two diaphragms are placed with an opening of 0.5 mm, corresponding to an area of approximately ten speckle spots of the scattered light. The distance between the diaphragms is 1 m, and are used to select a small fraction of the scattered light. The diaphragms are placed such that the coherent (unscattered) beam is in the middle of the diaphragm opening, so both the coherent and scattered beam are detected. In the alignment procedure great care is taken that the scattered and unscattered beam coincide over a length of 20 m.

A measurement consists out of an average of 50 to 100 configurations. For each configuration an average of 50 scans is recorded, with a time resolution of 0.5 fs, at a sampling rate of 5 kHz of the spectrometer. This sampling rate is much lower than the modulation frequency of the lock-in technique, so no beating effects between sampling frequency and modulation frequency are expected. After recording one configuration, the sample is moved 5 μm to measure a new configuration. Before starting a new recording of a configuration, we waited 60 seconds. In these 60 seconds the sample heats up, and an almost thermal equilibrium between heating by the laser and cooling by the environment is achieved in these 60 seconds. A complete measurement as described above takes about 8 hours.

A typical result of the time-resolved transmission of a sample of 1.43 μm is shown in Fig. 4.2 where we have plotted the intensity on a logarithmic scale as function of time (thick solid line). In this figure an exponential decay for long times over three orders of magnitude (five orders of magnitude for the thickest samples) is observed. The large peak is the coherent (unscattered) pulse, while the exponential decay is due to scattering in the sample. Apparently not all the fringes of the cross-correlation function have yet disappeared in our averaging procedure. The remaining fringes were removed by Fourier filtering. In Fig. 4.2 the intensity of this filtered signal is also presented as a function of time. This filtered signal is the source for an exponential fit, the result being shown in

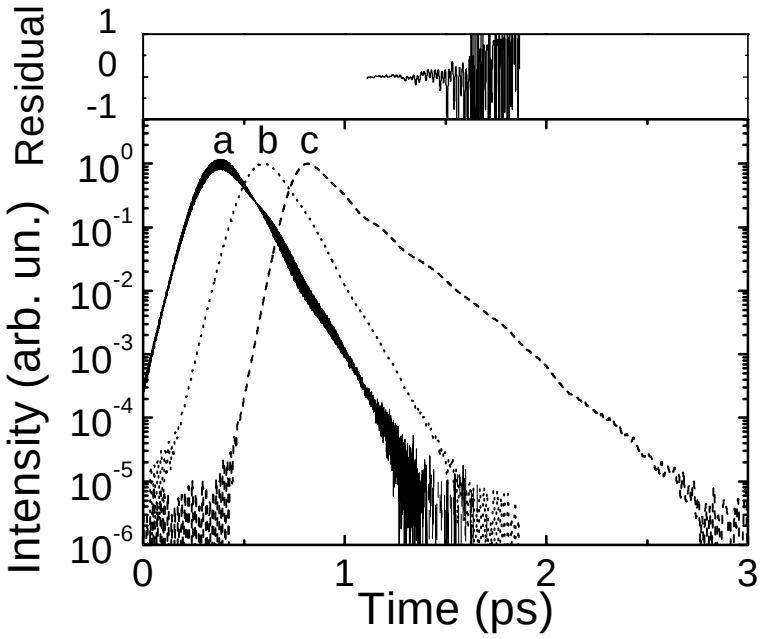

Figure 4.2: *Typical result of a time-resolved measurement of the scattered pulse on a 1.43 μm sample. The measurement is a result of an average over 50 configurations. The intensity of the pulse is plotted as function of time. We clearly see the coherent unscattered peak and an exponential decay over approximately three orders of magnitude due to propagation through the multiple scattering disordered sample. Note also that the fringes of the laser are not averaged out. The dotted line (b) shifted in time, represents the Fourier filtered cross-correlation function. To this filtered line, an exponential decay was fitted on the time interval* $1.1ps < t < 1.75ps$*, with as result a decay time of 70 fs. The relative residual between the determined and measured decay time is also shown. The dashed line (c) shows the result of a measurement on a 4.4 μm sample, demonstrating the exceptionally high dynamic range of almost six orders of magnitude.*

Fig. 4.2. To demonstrate the quality of the fit, we also present the relative residual in this figure. This procedure was repeated for all samples. To test the reproducability of the method, we measured one sample twice, and used the two independent data sets to estimate the error in the decay time for which we found 1 fs.

A deviation due to the dependence on the statistics of speckle spots might influence the measured decay time. To study the effect of this theoretically is far too complicated. Therefore we checked the influence of the number of speckle spots by measuring the decay time as function of the number of speckle

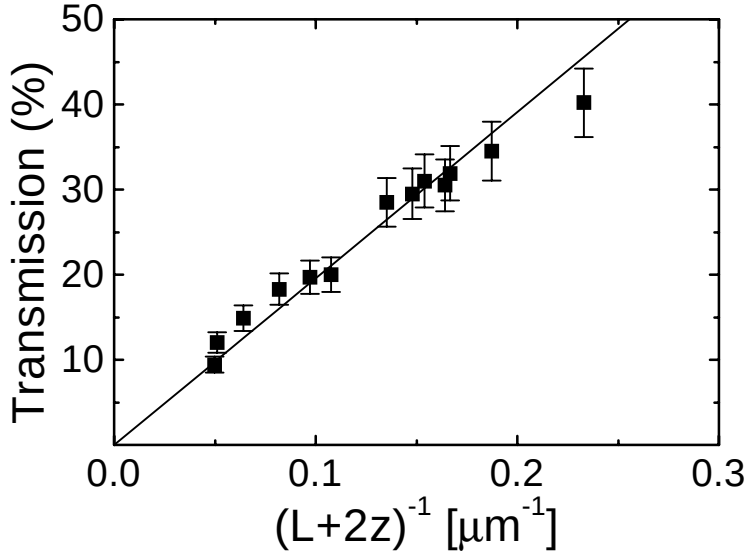

Figure 4.3: *Measured total transmission as function of sample thickness. The thickness of the sample is corrected for internal reflection with an extrapolation length* $2z = 2.3\ell$. *The solid line is the theoretical description of the total transmission for a transport mean free path* $\ell = 0.9\mu m$, *based on diffusion theory. The theoretical description of the total transmission is based on diffusion theory. From this picture we can conclude that this static measurement can be described by diffusion theory.*

spots by varying the opening of the diaphragms. From these experiments we concluded that the observed decay time does not exhibit a dependence on the opening area of the diaphragm.

4.3.3 Stationary measurements

We performed time-independent experiments to characterize our samples further. The transport mean free path of the samples was determined by recording the total transmission at the wavelength of interest ($\lambda = 781$ nm). In the setup the sample is illuminated at one side and all the transmitted light is collected using an integrating sphere. In Fig. 4.3 the results are presented, where the recorded total transmission is plotted as function of thickness of the sample.

Our samples are prepared on a quartz substrate ($n = 1.46$) leading to two boundaries with different reflection coefficients: $\overline{R}_{\rm as}$ (air-sample) and $\overline{R}_{\rm sq}$ (sample-quartz substrate) giving rise to two extrapolation lengths $z_{\rm as}$ and $z_{\rm sq}$.

Experiments performed to study the effect of refractive index contrast [51] showed that Mie theory in the independent scattering approximation gives reliable results for the mean index of refraction of the sample. We estimated for the mean index of refraction $n_{\text{eff}} = 1.34$ leading to $\overline{R}_{\text{as}} = 0.4$ and $\overline{R}_{\text{sq}} = 0.02$. The total transmission data were fitted employing results from diffusion theory with extrapolation length $z = (z_{\text{as}} + z_{\text{sq}})/2$. The fit for the total transmission is shown in Fig. 4.3 for the obtained value for the transport mean free path: $\ell = 0.95 \pm 0.1$ μm. In our experiments $k\ell \approx 8$ so our samples are indeed strongly scattering.

Close inspection of Fig. 4.3 for the very thin samples shows that the measured transmission is slightly lower than predicted by diffusion theory. It can be shown that the measured transmission for the very thin samples in our measurements is slightly too low [52] due to reflection at the surface-air interface of the substrate. Light reflected at this interface is injected in the sample again and it can be shown that this effects is relatively large for the very thin samples.

The transport mean free path can also be determined by another, independent, stationary experiment. Measuring enhanced backscattering cones [53] for thick samples yields a value for the scattering mean free path 0.65 ± 0.1 μm. This is in good agreement with the value obtained from the total transmission data and therefore gives an independent consistency check on both the measured sample thickness and transport mean free path. The absorption length has been determined and was found to be $\ell_{\text{abs}} \approx 80$ μm. The maximum thickness of our samples was 18 μm, so absorption plays no role in our experiments. All our stationary experiments could be interpreted with conventional stationary diffusion theory.

4.4 Discussion and conclusions

We will now try to interpret our dynamic results with time-dependent diffusion theory focusing on the *long-time* behavior of the transmitted pulses as described in section 4.2.2. For extremely thin disordered samples ($L/\ell \leq 1$) diffusion theory will clearly break down. Although for $L/\ell \leq 10$ deviations in the short-time behavior of transmitted pulses have been shown experimentally [54] one expects for long times diffusion theory still to hold. In conventional diffusion theory, the decay time τ_D exhibits a length dependence according to Eq. (4.5). The diffusion constant D follows from (4.5) and the experimen-

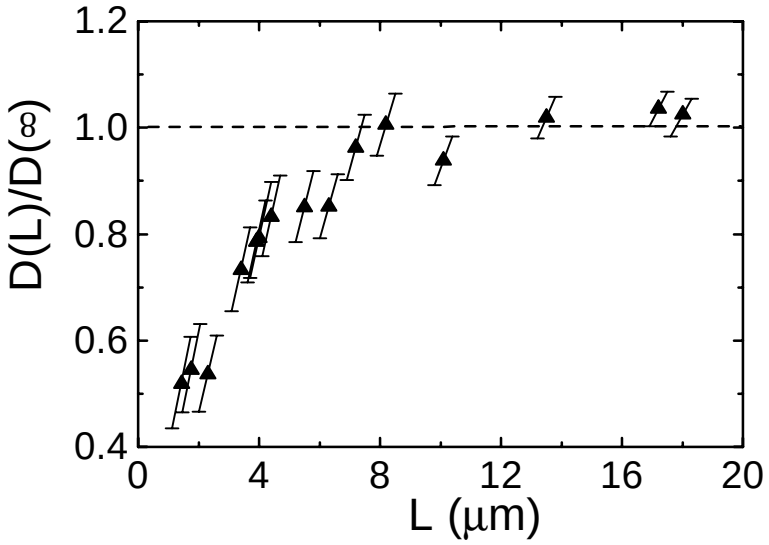

Figure 4.4: *The normalized measured diffusion constant (triangles) as function of sample thickness. The normalization is on the mean value of the four last data points (indicated with $D(\infty)$ and dashed line), for which we expect that the transmission can be described with diffusion. We clearly see a deviation of about 30% for the thinnest sample from a constant diffusion constant for all samples. ¡ The error bars are tilted, because the error in the diffusion constant is mainly due to the uncertainty in the thickness of the sample. The thickness of the sample is used to calculate the diffusion constant, which gives a dependent error resulting in these tilted error bars.*

tally obtained decay times and thicknesses of the samples, where we used an extrapolation length is discussed in the previous section (4.3.3). The results are presented in Fig. 4.4, where the diffusion constant is plotted as a function of sample thickness. We observe a strong dependence on sample thickness of the apparent diffusion constant for $L/\ell < 8$. The thick samples ($L/\ell > 8$) are characterized by the diffusion constant $\overline{D}$ that does not depend on thickness. We found $\overline{D} = 32 \pm 2$ m^2/s. Using this value as a reference one observes a deviation in the diffusion constant of about 50% for the thinnest sample. Obviously, $1/\tau_D$ does not obey the diffusion result (4.5).

We now try to explain our experimental results with radiative transfer theory that goes beyond the diffusion description. To investigate the length dependence of $1/\tau_D$ numerical calculations have been performed on the time-

resolved Bethe-Salpether (BS) equation [37, 55] for the intensity of multiple-scattered light for several slab thicknesses. Previous theoretical work [55] indicates that the transition of transport by coherent waves to transport obeying the diffusion equation can be studied as a function of slab thickness employing the time-resolved BS equation. For thick samples the BS equation can be shown to be equivalent to the classical equation of radiative transfer for $k\ell > 1$ [39, 40]. Refractive index mismatches can be introduced in the BS equation quite straightforwardly [56]. We solved the wave equation in particular for finite slabs using the complex propagation constant $K = \omega/c + i/(2\ell)$ (assuming isotropic scattering for simplicity). In these calculations we accounted for refractive index mismatches at the boundaries. One then obtains finite-size corrections depending on $\overline{R}$ to: a) the inhomogeneous or source term in the BS equation and b) the BS integral kernel described by the Green's function of the wave equation. For $L/\ell > 2$, our computed long-time exponential behavior gave values for $1/\tau_D$ which agreed within numerical accuracy with results from diffusion theory. Hence, no length dependence of $1/\tau_D$ differing from Eq. (4.5) was found in this extended approach and our numerical results do not explain our experimental data for $L/\ell < 8$.

As is the standard practice in this field we assumed isotropic scattering in all the above calculations. The influence of anisotropic scattering in the stationary case have been studied [43] showing that this affects the transmission properties of the samples and can be accounted for by modifying the extrapolation length. Our stationary measurements did not show any effect of this, however, we expect a stronger influence on the time-resolved propagation through the samples. Taking into account anisotropic scattering may possibly explain our experimental data. To numerically study dynamic finite-size effects for anisotropic scattering, however, is rather involved since one probably also has to focus on the specific intensity which also depends on the solid angle [40].

An alternative explanation for the length dependence of $1/\tau_D$ may lie in a renormalization of D related to a proper formulation of the scattering properties of TiO_2 particles in a finite geometry. When L, ℓ and λ are of the same order of magnitude, the scattering amplitude depends on the position of the scatterer in the slab, which may result in a modulation of the speed of light giving an effective reduction of the diffusion coefficient.

Chapter 5

Electron dynamics in gold

In this chapter we present measurements performed to study relaxation dynamics of a non-thermal electron gas in gold. The typical time scales involved with the relaxation of a non-thermal electron gas is expected to be in the order of femtoseconds. The method we employ to drive the electron gas out of equilibrium and to detect the non-equilibrium properties of the gas is to record an ultrashort optical pulse which is reflected from a gold film as described in Chapter 3. From the detailed structure of the cross-correlation function, information can be obtained about the non-equilibrium properties of the electron gas.

5.1 Introduction

Since the introduction of lasers which can generate ultrashort laser pulses, it is possible to study ultrafast relaxation dynamics. In these studies, it is the common practice to use a so called pump-probe technique. Often, in this technique a very strong laser pulse (pump pulse) creates a population, in the excited state. This induced population will change the optical properties of the sample. A second weak pulse (the probe pulse) is used to measure this pump-induced change of the optical properties. The probe pulse can be delayed with respect to the pump pulse and in this way it is possible to follow in time the relaxation to equilibrium. With these type of experiments the shortest time scale one can measure is in the order of the pulse length.

A subject which has been studied extensively, is the relaxation of a hot electrons in noble metals [57]-[64]. A reason for studying electrondynamics may be the realization that almost all modern high speed electronic contacts

are thin gold films. With the approach of the optical computer, the switching time will approach the femtosecond time domain and therefore the regime of nonequilibrium particle transport in the contacts. In these relaxation measurements, using an ultrashort laser pulse the electrons are excited to high-energy states. A general accepted scheme for the relaxation is that first the electrons thermalize. The hot electrons collide with cold electrons and redistribute their energy. In this way the hot electrons heat up the cold electron gas and at the end of this first relaxation step we have a Fermi-Dirac distribution of electrons which is not in equilibrium with the lattice. The typical time scale of this first relaxation step is generally believed to be very short, in the order of several femtoseconds. The next relaxation step is the cooling of the electron gas. The mechanism responsible for this step is electron-phonon scattering. This mechanism is much slower than the electron-electron scattering and is in the order of picoseconds. The last step is cooling of the lattice.

One conclusion can be already made from this scheme. The electron-electron scattering and the electron-phonon scattering are separated in time. First the electrons redistribute, until a Fermi-Dirac distribution is achieved, after which the electron-phonon scattering is responsible for further cooling of the electrons.

One of the first studies of this relaxation mechanism is that of Easley [59]. In these experiments the electron-phonon coupling constant in copper was measured, by a study of the relaxation of hot electrons. A theory to describe these measurements is the so called Two-Temperature Model. Because of the separation in time of the electron thermalizationand the electron-phonon coupling two temperatures are important: the temperature of the electron gas (Fermi-Dirac distribution), and the temperature of the lattice. The first femtosecond studies on gold [60] and copper [61] date from 1987.

Experiments performed by Groeneveld et al. [62] on silver showed deviations from this general accepted two-temperature model. The experiments could only be described satisfactory, if it was assumed that the first relaxation step was slower than generally accepted. This slow first relaxation step was later confirmed by Fann et al [63, 64], who observed thermalization times up to $\approx$1 ps in gold. This long thermalizationtime is consistent with Fermi-liquid theory, where the relaxation time for an electron with energy E above the Fermi energy E_F is proportional to $1/(E - E_F)^2$. In experimental situation a distribution in energy E of electrons is induced, leading to a whole range in relaxation times, where the longest relaxation times hold for the electrons

with an energy close to the Fermi energy. Due to the very long thermalization the electron-electron scattering time and electron-phonon scattering are not separated in time. Numerical simulations of the relaxation [62] showed that this very slow first relaxation step is indeed the case.

We have introduced a new technique, with which it is possible to look on time scales as short as 5 fs as we have shown in chapter 3. Up to now in this thesis we only considered systems where the response function, which relates the incoming and outgoing fields, was linear. The experiments described in this chapter are performed at high intensities, resulting in a nonlinear response of the system. The nonlinear relation between the fields is due to the changing dielectric constant which is a signature of the nonthermal distribution of the electrons . The main goal of the experiments described in this chapter is to study the electron dynamics very short time scales employing the new technique.

5.2 Theory

5.2.1 Band structure of gold

In the pump-probe measurements as discussed in the previous section, changes in optical properties are measured. One of the optical properties which change due to the excited electrons is the dielectric constant. In this chapter we discus measurements on gold. Because all the noble metals have a similar type of band structure, resulting in similar optical properties for all the noble metals, the results presented here are representative for all noble metals.

The reddish color of copper and yellowish color of gold indicates that the dielectric constant has a strong dependence on frequency. Band-structure calculations for noble metals pointed out that the Fermi surface is almost contained to within the first Brillouin zone [65]. The Fermi surface only points through the zone into the next in the <111> directions. This is why the band structure is sometimes referred to as the 'Belly and Neck' structure, a structure that is confirmed by the Haas-van Alphen measurements [66]. The described structure resembles a free-electron picture, so we expect a mainly free-electron or Drude-like contribution to the dielectric constant. The Drude-like contribution to the dielectric constant will give a relatively structureless contribution as function of frequency. Therefore the dielectric constant does not describe the observed characteristic threshold that appears in the reflectivity in the

noble metals responsible for the reddish color. Another contribution to the dielectric constant comes from the bound electrons in the noble metals. The bound electrons will result in an extra band in the band structure, as shown in Fig. 5.1 where we have plotted contributions of these bands to the filled density of states for gold indicated by the shaded areas. The filled density of states is given by the product of the density of states $D(E)$, indicated by the dashed lines in this figure, times a distribution function $f(E,T)$ which is in general a function of temperature T and accounts for the fact if a state at energy E will be occupied. The free-electron band, the p-band, gives a Drude-like contribution to the dielectric constant, indicated by the light shaded area in Fig. 5.1. The other band, the d-band, is due to the bound electrons and lies 2.5 eV below the Fermi surface [67]-[69] and is indicated by the dark shaded area. The reddish color of copper and gold are due to the interband transition from the p to the d-band.

In our experiments we use a Colliding-Pulse Modelocked (CPM) laser. The photons of this laser have an energy of 2 eV, so with these photons it is not possible to excite interband transitions from the d-band to the p-band. However, intraband transitions in the free electron band are possible. Due to the excited electrons new interband transitions are possible with the laser photons (see Fig. 5.2). These new transitions will give a change in the the dielectric constant. The change in the dielectric constant gives us a spectroscopic tool to detect excited electrons. For instance, a time resolved reflection measurement would give information on the relaxation of the electron gas.

5.2.2 The Surface Plasmon Polariton Resonance

The relaxation of the electron gas can be studied with a time-resolved reflection measurement, for instance a pump-probe technique. The pump pulse excites the electrons, which results in a change of the dielectric constant. However, the induced change is very small. In the experiments of Groeneveld et al.[62] on silver, an estimation was made of the change of the real part of the dielectric constant and they found this to be $2.66 \times 10^{-6} K^{-1}$. We also need a efficient way to excite the electrons. The experiments of Groeneveld et al. [62] showed that the Surface Plasmon Resonance (SPP), can be used for both efficient excitation of the electrons and as a efficient detection of small changes in the dielectric constant.

In the bulk of a metal one can excite electron-density fluctuations, also

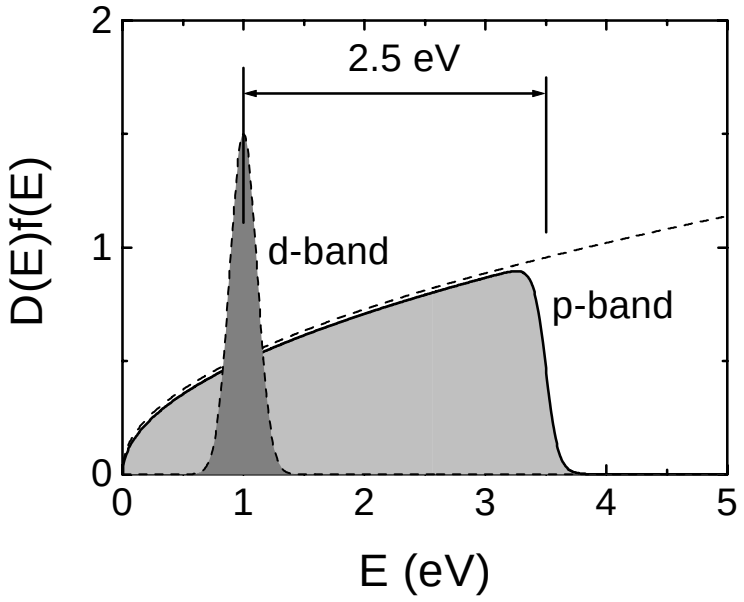

Figure 5.1: *Contributions to the filled density of states for gold. The light shaded area represents the filled states in the p-band at room temperature, given by $D(E)f(E,T)$, where $D(E)$ is the density of states and $f(E,T)$ the Fermi-Dirac distribution function at time T. The dark shaded area is the completely filled d-band. The d-band lies 2.5 eV below the Fermi energy of the p-band.*

known as plasmons. If an interface is present between two different metallic media, the electric field perpendicular to the surface will be discontinuous, giving rise to surface charges. Therefore, at the interface one can excite a special kind of plasmon mode, known as the SPP. The fields associated with the SPP can be calculated by solving the Maxwell equations near the interface of a metal, when using appropriate boundary conditions. Let us consider a metal at the negative side of the $z = 0$ plane. At the positive side of the $z = 0$ plane we consider a transparent dielectric. The appropriate boundary conditions at the $z = 0$ plane are: a) a continuous tangential component of the electric field ($= E_{//}$) and b) a continuous normal component of the displacement vector $\mathbf{D}$ ($= \epsilon E_{\perp}$). The electric field associated with the SPP

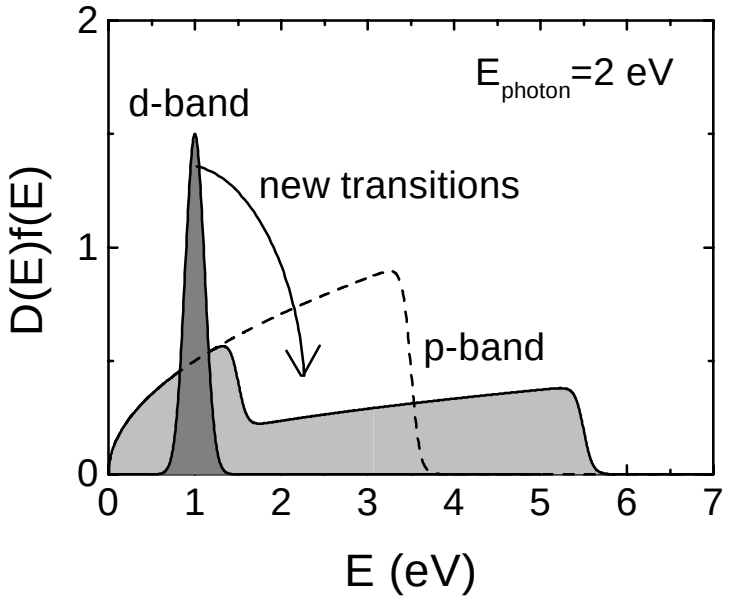

Figure 5.2: *Schematic plot of the non-equilibrium distribution of the electron gas. In equilibrium (dashed line), no interband transitions are possible simply because there are no states available in the p-band. In case of a strong pulse the electron gas is driven out of equilibrium and new states become available (light shaded area), resulting in a change of the dielectric constant of the metal film.*

are [70]:

$$\mathbf{E}(z,t) = E_0 \begin{pmatrix} 1 \\ 0 \\ ik_{spp}/q3 \end{pmatrix} e^{i(k_{spp}x-\omega t)} e^{-q_3 z} + c.c. \qquad \text{dielectric(z} > 0); \quad (5.1)$$

$$\mathbf{E}(z,t) = E_0 \begin{pmatrix} 1 \\ 0 \\ -ik_{spp}/q2 \end{pmatrix} e^{i(k_{spp}x-\omega t)} e^{+q_2 z} + c.c. \qquad \text{metal(z} < 0). \quad (5.2)$$

The given fields lie in the x-z plane. From the boundary conditions we find a relation between wave vectors for the SPP in the metal and the dielectric:

$$\epsilon_3 q_2 = -\epsilon_2 q_3. \quad (5.3)$$

Together with the wave equation

$$\nabla^2 \mathbf{E} = \epsilon(z) k_0^2 \mathbf{E} \quad (5.4)$$

with $k_0 = \omega/c$ this will lead to the following expressions for the wave vectors:

$$q_3 = \sqrt{k_{spp}^2 - \epsilon_3 k_0^2}; \quad q_2 = \sqrt{k_{spp}^2 - \epsilon_2 k_0^2}. \tag{5.5}$$

Where in the dielectric (z>0) the dielectric constant is indicated by $\epsilon(z) = \epsilon_3$, and in the metal (z<0) with $\epsilon(z) = \epsilon_2$. From the wave vectors, and Eq. (5.3) we find for the wavevector of the SPP:

$$k_{spp} = k_0 \sqrt{\frac{\epsilon_2 \epsilon_3}{\epsilon_2 + \epsilon_3}}. \tag{5.6}$$

The above calculation shows some features of the SPP. From the field equations we can conclude that the SPP is a transverse magnetic (TM) mode. The associated magnetic field is perpendicular on the direction of propagation. The dielectric constant of a metal is complex valued and has a negative real part. The negative real part is essential because only then the electromagnetic waves are bound to the interface due to the fact that electromagnetic waves cannot propagate. The large imaginary part of the dielectric constant gives the light enough momentum to be able to excite the SPP. The wavevector of the SPP is complex because the dielectric constant of the metal is complex. The imaginary part reflects the decay of the SPP in the direction of propagation. This decay of the SPP is due both absorption and scattering by electrons, which reflects the plasmon character, and is the process responsible for the excitation of the electrons. We also see that the wavevector of the SPP is strongly dependent on the dielectric constant of the metal. This dependence shows that the SPP can be used to measure changes in the dielectric constant.

5.2.3 Excitation of the SPP

The SPP is a TM mode showing that the SPP can only be excited by p-polarized light. Incident light impinging on metal-dielectric interface does not have enough momentum available to excite the SPP, which can be seen from Eq. (5.6). Several geometries have been proposed in the past to excite the SPP, and in this section I would like to discuss the so called Kretschmann geometry, proposed by Kretschmann in 1971 [71] and shown in the inset in Fig. 5.3.

A way for creating a light field with enough momentum to excite the SPPis to use total internal reflection in a prism. At the rear side of the prism in which the light is reflected, the light falls of exponentially with distance and has to much momentum to excite the SPP. This exponentially decaying

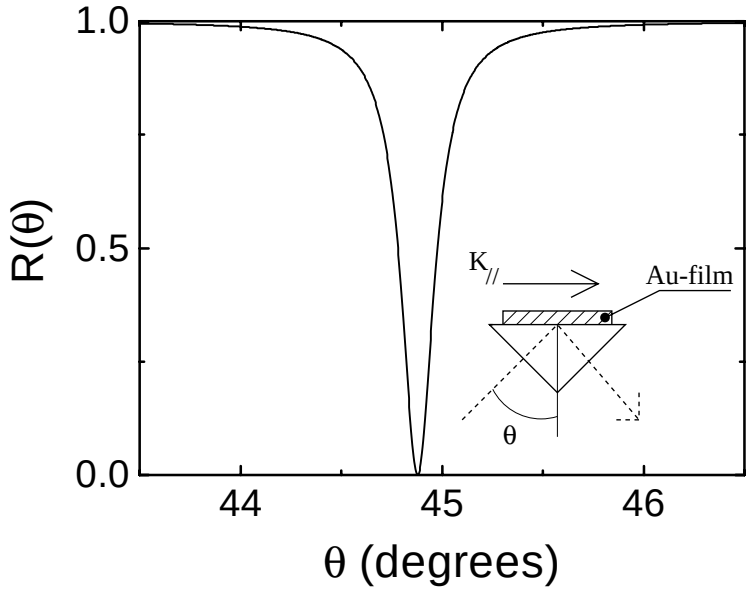

Figure 5.3: *Reflection R of the Kretschmann geometry as function of angle θ. The Kretschmann geometry is shown in the inset. By tuning the angle the wavevector of the light $k_{//}$ is matched with the wavevector of the the SPP resonance. At resonance ($\theta \approx 49^o$) all the light is absorbed by the SPP, and no light is reflected.*

light is known as the "evanescent wave". For p-polarized light the wavevector of this evanescent wave is: $k_{//} = (\omega/c)\sqrt{\epsilon_1}sin(\theta)$, where ϵ_1 is the dielectric constant of the prism. The parameter θ is the angle of incidence. If a thin layer of gold is placed on the rear side of the prism, we can excite the SPP resonantly in the gold film by tuning the angle of incidence with respect to the hypotenuse face of the prism. In this way we match the wavevector $k_{//}$ and the wavevector k_{spp}. This is shown in Fig. 5.3, where we have plotted the result of a calculation of the reflection of the Kretschmann geometry as function of angle. The Kretschmann geometry in this calculation consists out of a 51 nm gold film on a quartz prism. The wavelength of the incident light was 633.8 nm, the HeNe-laser wavelength. At the angle where the wavevector of the light is matched with the wavevector of the SPP ($\theta \approx 49$), the SPP is excited resonantly and no light is reflected. This is the Kretschmann geometry [71] and was used in our experiments.

5.2.4 Response function of the Kretschmann geometry

In the previous section we discussed the Kretschmann geometry used in the experiments to excite the SPP resonance. Besides the excitation of the SPP resonance which distorts the incoming pulse, the light also travels through a prism which also distorts the pulse. If we denote the response function of the prism with $H_{prism}[\omega + i\varepsilon]$, the total response function is given by:

$$H_{tot}[\omega + i\varepsilon] = H_{SPP}[\omega + i\varepsilon]H_{prism}[\omega + i\varepsilon], \tag{5.7}$$

where $H_{SPP}[\omega + i\varepsilon]$ is the response function of the SPP, which will subject of discussion in the next section. Now we will treat the response function of the prism.

The prism is made of BK7 glass, and the traveled path length through the glass is approximately 1 cm. For the CPM wavelength (630 nm) the absorption of the prism is negligible, but because of the large bandwidth of the laser the dispersion can not be neglected. This wavelength-dependent index of refraction results in a phase relation, which must be included in the total response function of the Kretschmann geometry, for which we write:

$$H_{prism}[\omega + i\varepsilon] = \exp\{i\beta(\omega)z)\}, \tag{5.8}$$

where $\beta(\omega)$ is the propagation parameter, depending on the type of material through which the light has propagated and z the traveled path length through the glass. The parameter $\beta(\omega)$ can be expanded in a Taylor series around the central frequency of the CPM laser. In catalogs of manufacturers of optical components [72], the wavelength dependence of the index of refraction of materials is often given in formulas similar to the Sellmeir's dispersion formula [8]. A more useful form based on a fit on the dispersion formula is [73]:

$$\beta(\Delta\omega) = 0.3323 \times 10^{-2}\Delta\omega^2 + 0.1907 \times 10^{-4}\Delta\omega^3, \tag{5.9}$$

for BK7 glass. Where $\Delta\omega = \omega - \omega_0$, with ω_0 the central frequency of the CPM laser measured in units 10^{-13}. This formula is experimentally verified to give reliable results [73].

5.2.5 Calculation of the resonance condition of the SPP

In this section we will derive a approximate expression for the SPP resonance condition as found by Kretschmann [71]. In this derivation use is made of the

finite thickness of the metal film, which is the active medium supporting the SPP. The derivation is similar as that given by van Exter [74].

The response function of the Kretschmann geometry is identical to the response function of an etalon in reflection Eq. (2.44). If the light in the Mach-Zehnder interferometer is p-polarized, the **k**-vector of the light parallel to the hypotenuse face is angular dependent. For the angle dependent reflection at an interface we can write similar to Eq. (2.42):

$$r_{ij} = \frac{\epsilon_i k_j - \epsilon_j k_i}{\epsilon_i k_j + \epsilon_j k_i}, \tag{5.10}$$

with k_j the perpendicular component of the wavevector in medium j, defined by $k_j = \sqrt{(\omega/c)^2\epsilon_j - k_{//}^2}$, where $k_{//}$ is the parallel wavevector. This parallel wavevector will be continuous at the boundary according to the first boundary condition above Eq. (5.1) (continuous $E_{//}$).

The resonance condition of the SPP corresponds to an extremum in Eq. (2.44), which can be found by setting the denominator to zero:

$$\frac{1}{r_{23}} + r_{12}\exp(ik_2 d) = 0 \tag{5.11}$$

Up to now, we did not make any assumptions, and the given formulas are exact. An approximate expression of (5.11) in the neighborhood of the pole can be found easily by using the fact that the thickness of the metal film is thin and the transmissivity of the film is small. In that case $\exp(2ik_2 d)$ is small, and the finite thickness of the metal film only weakly perturbs the surface-plasmon character. In this case the resonance condition reduces to $1/r_{23} = 0$, which occurs if $k_{//}$ is matched with the SPP wavevector. We can expand $1/r_{23}$ around $k_{spp} = k_{//}$ in $1/r_{23} = \alpha(k_{//} - k_{spp}) + ...$ and only keep the first term, where α is defined through this expansion. The small perturbation of the surface-plasmon due to the finite thickness can be found by substituting this approximation in the denominator (5.11), and we find that the SPP resonance condition is shifted by an amount:

$$\Delta k_{spp} = \frac{1}{\alpha} r_{12} e^{2ik_2 d}. \tag{5.12}$$

If we account for this small shift of the SPP resonance, we can write for Eq. (2.44):

$$H_{SPP}[\omega + i\varepsilon] = \frac{\alpha(k_{//} - k_{spp}) + (1/r_{12})e^{2ik_2 d}}{\alpha(k_{//} - k_{spp}) - \alpha\Delta k_{spp}}. \tag{5.13}$$

We can derive for this equation a much simpler form if we use the fact that the reflection at the prism-metal interface is almost unity ($|r_{12}|^2 \approx 1$), thus $1/r_{12} \approx r_{12}^*$. Furthermore we know that the wavevector k_2 is dominantly imaginary so that $(1/r_{12})\exp(2ik_2d)$ can be rewritten into αk_{spp}^* and we finally find for the reflectivity:

$$H_{SPP}[\omega + i\varepsilon] = r_{12}\frac{k_{//} - k_{spp} - \Delta k_{spp}^*}{k_{//} - k_{spp} - \Delta k_{spp}}. \tag{5.14}$$

So we have found an approximate expression for the amplitude reflection coefficient in case of the Kretschmann geometry, near the resonance angle. In this expression all the physical properties of the SPP resonance are incorporated. The parameter $k_{//}$ is the wavevector of the light parallel to the interface for p-polarized light, which is a real quantity. The parameters k_{spp} and Δk_{spp} are both complex quantities. The minimum of reflectivity is found for $k_{//} = k_{spp}^{'} + \Delta k_{spp}^{'}$, where the single prime means real part. This minimum drops to zero if $\Delta k_{spp}^{''}$ equals $k_{spp}^{''}$, where the double prime stands for imaginary part. The parameter Δk_{spp} reflects the deviation from SPP character in SP character. The imaginary parts of both the parameters k_{spp} and Δk_{spp} describe the damping of the SPP. Radiative damping is described by the imaginary part of Δk_{spp}. This mechanism can simply be seen as photons that leak back into the prism, and can be considered as the reflected light. The imaginary part of k_{spp} describes the damping of the SPP by electron-hole excitation. Earlier we have seen that for the photons we use in our experiment, which have an energy of 2 eV, this damping mainly arises from interband transitions.

Up to now in this thesis we only considered systems where the response function, which relates the incoming and outgoing fields, was linear. The experiments described in this chapter are performed at high intensities, resulting in a nonlinear response of the system. The nonlinear relation between the fields is due to the changing dielectric constant. During the reflection of the pulse, the dielectric constant changes depending on the intensity of the pulse, resulting in a nonlinear relation between the incoming and outgoing fields. In case of this nonlinear relation, a more elaborate analysis of the pulse distortion is required. One difference with the straightforward Fourier analysis is the time dependence of the response function. Due to absorption of light, intraband transitions will create a non-equilibrium distribution of the electrons in the p-band (see Fig. 5.2). This distribution will result in new resonant transitions for the wavelength we use in our experiments. Finally these new resonant states are responsible for the change in the dielectric constant of the metal.

The deposited energy in the metal will depend on time during the reflection of the pulse and therefore the dielectric constant will be a function of time. Using this fact, we approximate the response function of the SPPSurface-Plasmon Polariton by:

$$H[\omega + i\varepsilon] = H[\omega + i\varepsilon; T(t)], \tag{5.15}$$

where $T(t)$ represents the dependence of the response function on the heating of the electron gas at time t. The dependence of the response function on the temperature of the electron gas will be discussed in more detail in section 5.4.

5.3 Experimental

5.3.1 The SPP resonance

According to Eq. (5.7), the response of the Kretschmann geometry consists out of a product of the response of the bare SPP resonance and the response function of the prism. In our experimental situation the prism in the Kretschmann geometry is made out of BK7, and the traveled path length of the light through the prism is approximately 25 mm. In a first experiment, we studied the response function of a piece of BK7 glass with a thickness of 25mm, the result being shown in Fig. 5.4a. In this figure we have plotted the amplitude (dashed line) and phase (circles) of the response function (5.8) as function of wavenumber. When we compare the spectrum of this measurement with the spectrum of the CPM laser (Fig. 3.3b), we see that the absorption by the glass is negligible, as we had anticipated. The phase is fitted with a parabola, the result being shown in this figure (solid line) and is in excellent agreement with the experiment and we conclude that third order effects in frequency in (5.9) play no role for the given bandwidth of the CPM laser. From (5.8) together with (5.9) we found a thickness of 22 mm for the BK7 glass which is in reasonable agreement with the experimental situation.

The next step was to record the cross-correlation function, with the Kretschmann geometry at SPP resonance conditions in one of the arms in the Mach-Zehnder interferometer. We first studied the SPP resonance at low intensities and we expect that the obtained results can be described by Eq. (5.7).

The result of the measurement is shown in Fig. 5.4. The long dashed line in this figure is the Fourier transform of one of the measured cross-correlation functions. If we compare the measured spectrum with the spectrum of the CPM laser (see Fig. 3.3b), we observe a sharp dip at approximately 15850

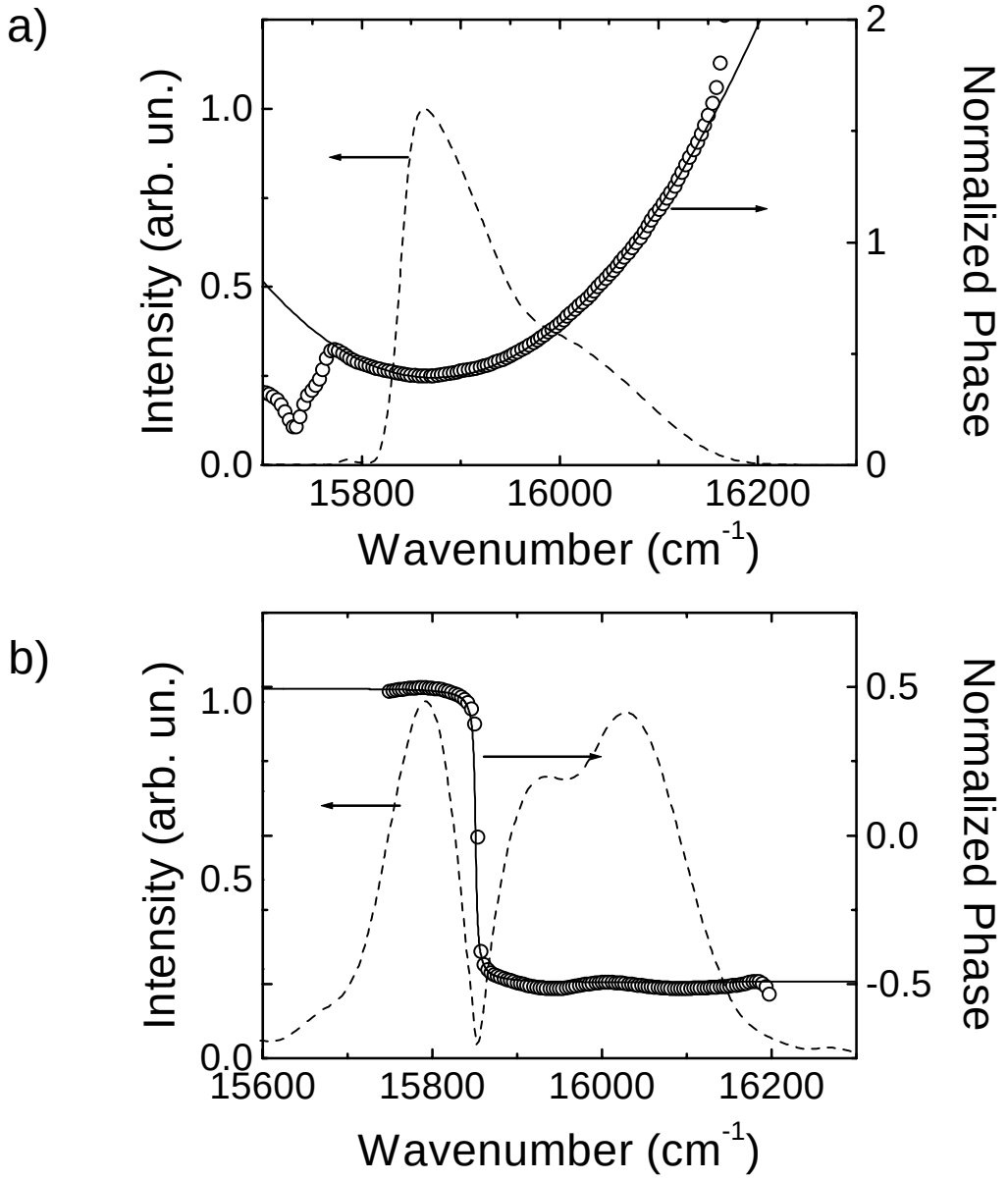

Figure 5.4: *(a) Measured response function of 25 mm glass (BK7) as function of wavenumber. The dashed line represents the spectral content of the pulses after traveling through the glass. Comparing the measured spectrum to the CPM spectrum (Fig. 3.3b) we see that absorption is negligible. The circles represent the observed phase. This phase is fitted with the response function* H_{prism} *(Eq.5.9), the result also being shown in this figure (solid line). (b) The spectrum of a phase-sensitive interferometric measurement of the chirp introduced by a SPP indicated by the long-dashed line in (right axis). The measured phase relation is indicated with the circles (left axis) and the solid line is theoretical prediction of the phase relation. The error in these figures is approximately the symbol size.*

cm^{-1}. This dip is due to absorption of the SPP-resonance. The circles in Fig. 5.4b are the data points of the measured phase relation of the pulse. These points are corrected for the phase introduced by the BK7 prism, with parameters found from the experiment described above and the only contribution in this figure is from the SPP resonance solely. The solid line in Fig. 5.4b is the best numerical fit of the argument of the response function of the SPPSurface-Plasmon Polariton resonance (5.14). The same fit procedure is used as in the experiments with the etalon (chapter 3). The parameters used in the calculation of the reflectivity are the same as those used in reference [62] for a gold film with a thickness of 42 nm ($\epsilon_{prism} = 2.28, \epsilon_{gold} = -13 + 1.8i, \theta = 43.76^{\circ}$). The error in Fig. 5.4b, which approximately the size of the symbols, is the uncertainty found from the experiments performed with the etalon (chapter 3). Within the experimental errors, the experimentally found phase relation is in agreement with theory

5.3.2 Electron dynamics

To be able to see any effects due to the non-equilibrium distribution of the electrons, we have to focus the beam to achieve high enough intensities in a small volume. Only then we induce a large distortion of the electron gas, which enables us to study non-equilibrium effects of the electrons. An unavoidable disadvantage of focusing is that the sample heats up, due to which the SPP resonance will shift (see appendix A). In a measurement we must be able to distinguish between heating effects and effects due to the non-equilibrium distribution of the electron gas. Besides the fact that one does not precisely understand the heating effect yet (see appendix A), measuring very accurately the temperature rise due to energy dissipation is very difficult.

We start with describing a setup with which it is possible to account for the temperature rise of the metal film, without measuring the actual temperature. The experimental set-up is shown in Fig. 5.5. The detailed structure of a weak and strong pulse are measured as described in Chapter 3. The weak pulse measures the SPP resonance of the heated sample and this resonance is used as a reference. Approximately 1 ps after the weak pulse a very strong pulse reflecting from the Kretschmanngeometry, drives the electron gas out of equilibrium. The intensity of the strong beam is about 3 mW, whereas the weak beam was about 0.15 mW. The weak pulse is so weak that the change of the dielectric constant it causes can be neglected. Within the pulse duration of

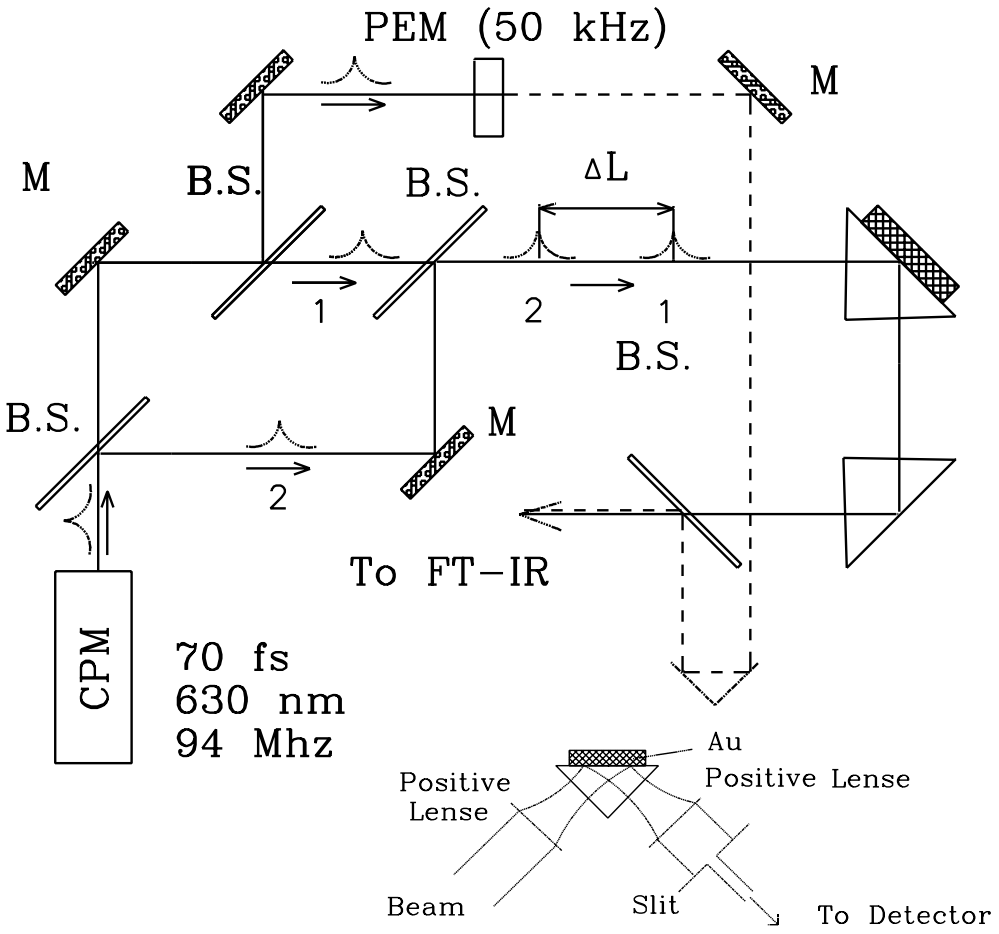

Figure 5.5: *The experimental set-up for measuring electron dynamics. A strong and weak pulse are used to excite the SPP at resonance conditions. The reference pulse is modulated with a photo-elastic modulator. The auto-correlation function pulse of the three pulses is measured with the FT-IR at the modulation frequency, using a lock in amplifier.*

the pulse used in the experiments the electron gas is driven out of equilibrium, resulting in a change of the dielectric constant. Comparison of the weak and strong pulses gives information of the change of the dielectric constant due to the non-equilibrium distribution of the electron gas.

The autocorrelation function is measured for three pulses. The weak and strong pulse, which probe the SPP resonance and a third undistorted pulse which will be considered as the reference pulse. The autocorrelation function would contain more than just the cross-correlation functions between the undistorted and reference pulses but also cross-correlation functions between

Figure 5.6: *Next page. a) Typical result of a measurement of the autocorrelation function with three pulses. We have plotted only one side of the autocorrelation function as function of time delay. The difference between the two cross-correlation functions is due to the non-equilibrium distribution of the electron gas. b) Deconvoluted full response function. We have plotted the amplitude and phase of the response function as function of wavenumber. The dashed line is the weak pulse, the solid line the strong pulse.*

the two distorted pulses. However, if we modulate the reference pulse, and measure the autocorrelation function at the modulation frequency, the autocorrelation contains only cross-correlation functions between the distorted and reference pulses. To modulate the pulses we used a photo-elastic modulator (model Hinds I/FS50) together with a polarization filter. We used photo-elastic modulator instead of an acousto-optic modulator because the latter lengthens the pulse by introducing a chirp, whereas the photo-elastic modulator we used is made of fused silica, which does not have this side effect. The photo-elastic modulator modulates the polarization at 50 kHz. Together with the polarization filter, we have a 100 kHz amplitude modulation. This beam is sent into the FT-IR and the signal is modulated with a frequency of 5 kHz. This beam is demodulated at the 100 kHz frequency using an EG&G (model 5210) lock-in amplifier and at the slow frequency with the internal lock-in amplifier of the FT-IR. A measurement consists of an average over 1024 scans recorded with a resolution of 0.25.

A result of a measurement is shown in Fig. 5.6a. We have plotted the response of the detector as a function of time delay in the Michelson interferometer. Only one side of the autocorrelation function is shown. We clearly see the autocorrelation peak of the modulated undistorted pulse, and the cross-correlation peaks between the weak and strong distorted pulses with the undistorted pulse. In the two insets in this figure, we zoom in on the measured cross-correlation functions. These insets clearly demonstrates that the recorded cross-correlation functions differ for the weak (left cross-correlation function) and strong (right cross-correlation function) pulse.

In Fig. 5.6b we present the deconvoluted amplitude and the phase of the Fourier transforms of both cross-correlation functions as function of wavenumber. The solid line represents the strong pulse, the dashed line the weak pulse. Also here the measured data exhibit a significant difference between the pulses in both the amplitude and the phase, which is probably due to the

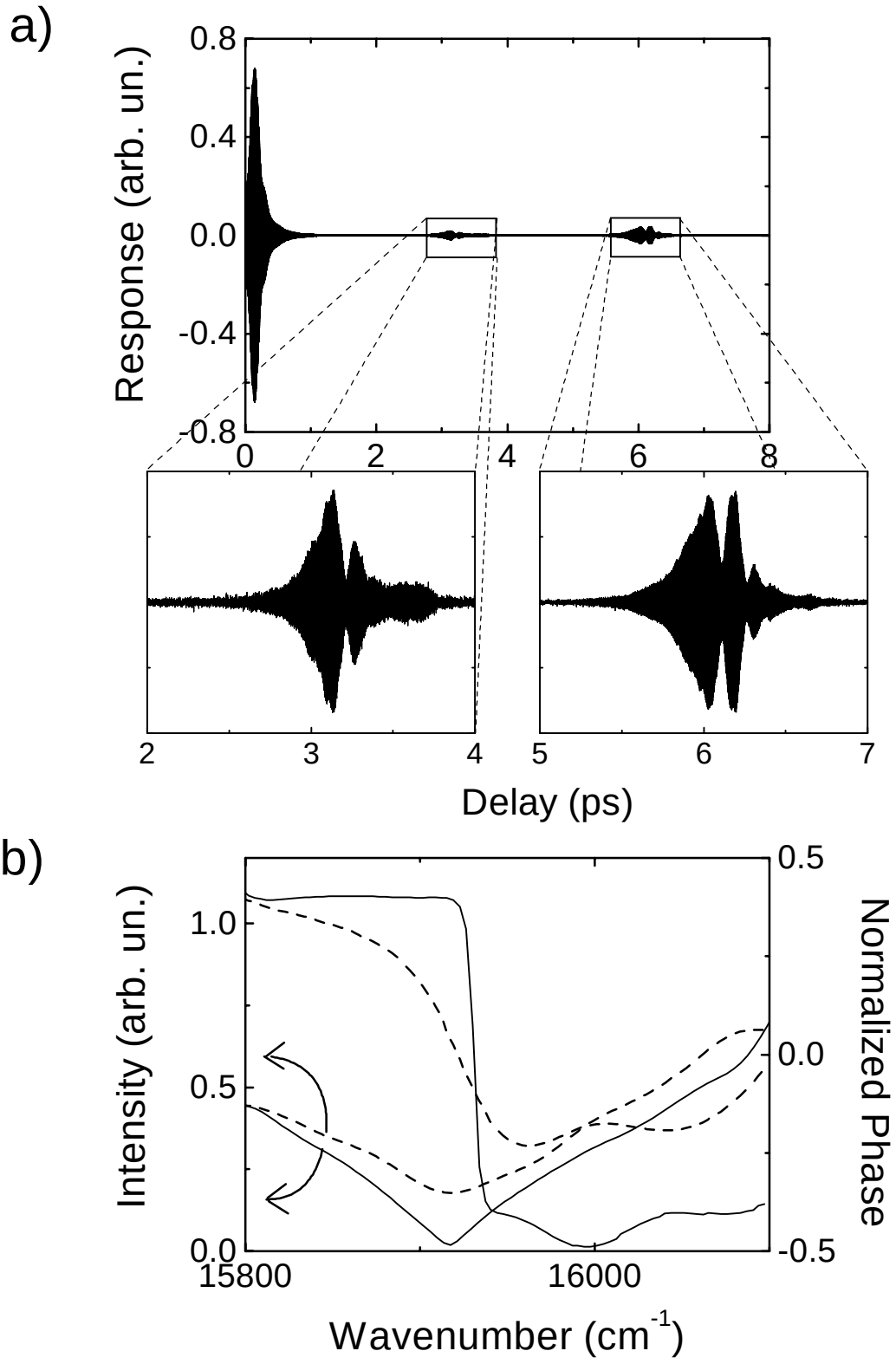
a)
Response (arb. un.)
0.8
0.4
0.0
-0.4
-0.8
0
2
4
6
8
2
3
4
5
6
7
Delay (ps)
b)
Intensity (arb. un.)
1.0
0.5
0.0
0.5
0.0
-0.5
15800
16000
Normalized Phase
Wavenumber (cm-1)

non-equilibrium electron gas.

5.4 Numerical calculations

If we compare the weak and strong pulse in our measurements, we see a significant difference. We expect that the difference is due to the electron gas being driven out of equilibrium by the strong pulse. The non-equilibrium electron gas results in a change in the dielectric constant of the gold and a corresponding change of the SPP resonance is finally responsible for the difference between the reflected weak and strong pulse. The change in the response function was indicated by $H[\omega + i\varepsilon; T(t)]$ in section 5.2. To extract qualitative information about the non-equilibrium distribution electron gas from our experimentally obtained data is difficult. It is for instance out of the question to find an analytic expression for this response function with a non-equilibrium electron gas. To tackle the problem of interpreting our data, we performed numerical calculations to describe our measurements in a more quantitative way, which will be the subject of this section.

In section 5.2 we calculated the reflectivity of the Kretschmann system at SPP resonance condition (Eq. (5.14)). This equation, describing the reflectivity, enables us to calculate the response function of the system in the frequency domain. To compute the reflection with a dielectric constant which changes during reflection of the pulse, we first have to know the change in the dielectric constant.

In the experiments of Groeneveld et al [62], the change of the dielectric constant as function of time could be described by Fermi-level smearing. The obtained expressions are based on experiments and calculations of Rosei [68] for silver. Rosei used an approximation for the band structure around the L-points in the zone scheme (silver has an fcc structure) with parabolas, because the interband transitions of silver are located at that point. With this approximation an expression for the Joint Density of States of all allowed interband transitions (JDOS) can be found in closed form. Using this it can be shown that the change of the real part of the dielectric constant is proportional to the change in temperature of the electron gas:

$$\epsilon_2'(t) = \epsilon_2' + \frac{d\epsilon_2'}{dT_e}\Delta T_e(t), \tag{5.16}$$

where ϵ_2 is the dielectric constant of the metal, and ΔT_e the change in temperature of the electron gas, which is a function of time as we will show later.

Gold also has an fcc structure, but there are two main differences compared to silver. The first is in the location of the interband transitions of gold. Band-structure calculations [76] predicted that the absorption edge is due to two contributions, a contribution located at the L-point and one located at the X-point. Ellipsometric experiments done by Guerrisi [77] confirmed this prediction of the composite nature of the absorption edge. Temperature dependent experiments and calculations which include the splitting of the interband transitions where done by Winsemius [78], who concluded that the change in the dielectric constant with temperature is linear, as already found for silver. The other difference with silver is the energy difference between the Fermi surface of the free-electron band and the bound electron band, which is 2.5 eV in case of gold and 4.03 eV in case of silver [79]. The measurements by Groeneveld et al. were performed at the same wavelength as we used in our experiments. The difference in the interband splitting for this wavelength makes the contribution in the change in the dielectric constant different. In case of gold, the interband splitting (2.5 eV) is small compared to the energy of the photons and a non-equilibrium distribution of the electron gas will result in new resonant states. These new states give rise to extra absorption, which mainly contribute an imaginary change to the dielectric constant. For silver the interband splitting (4.03 eV) is large compared to the energy of the photons (2 eV). A non-equilibrium distribution of the electron gas therefore, does not induce new resonant states. If no new resonant states are induced the effects are mainly due to the tails of the dispersive part of the induced resonance which falls of with $1/\omega$, if we assume that the resonance is a Lorentz line shape. This $1/\omega$ behavior of the tails of the dispersive part has to be compared with a $1/\omega^2$ behavior for the absorptive part, which shows that at the wavelengths we use in the experiments the influence of the absorptive part is negligible. The dispersive part contributes a purely real change in the dielectric constant. These arguments can be used to distinguish between two different situations. If we would assume now that the thermalization of the electrons is much slower than the pulse duration the change in the dielectric constant will be mainly imaginary. If the electron gas thermalizes much faster than the pulse duration of the pulses in our experiments, the change in the dielectric constant will be dominantly real.

In the calculations we present here, we assume that the change in the dielectric constant is proportional to the change in temperature of the electron gas in case of it is thermalized (Eq. (5.16)). This assumption of a thermal-

ized electron gas corresponds to the two-temperature model. In this model one describes the metal by two subsystems, one for electrons and one for the phonons. Each subsystem is in thermal equilibrium, so the electrons are described by a Fermi-Dirac distribution characterized by a temperature and the phonons are described by a Bose-Einstein distribution characterized by the lattice temperature. The two-temperature model describes the relaxation of electrons and lattice towards thermal equilibrium. The temperature of the electron gas can be found, knowing that the specific heat of the electron gas is temperature dependent: $C_e = \gamma T_e$. If an energy of U_l is deposited by the laser in the electron gas, we can write:

$$U_l = \int_{T_i}^{T_e} \gamma T_e dT_e, \tag{5.17}$$

where T_i is initial temperature. We finally find for the peak electron temperature:

$$T_e = \sqrt{T_i^2 + \frac{2U_l}{\gamma}} \tag{5.18}$$

This equation together with Eq. (5.16) describes the change of the dielectric constant as function of the dissipated energy U_l in the electron gas. This dumped energy is a function of time: $U_l = U_l(t)$ and therefore $T_e = T_e(t)$, showing together with (5.16) that the dielectric constant is a function of time in the situation of an electron gas which is driven out of equilibrium. In principle it is possible now to find the pulse in the time domain by computing the convolution of the pulse with the response function with a time dependent dielectric constant. The time dependence of the dielectric constant is caused by the time dependence of the deposited energy of the laser pulse.

In our numerical calculation the reflection of the pulse is computed in small time steps as indicated in the block diagram Fig. 5.7. For each time step indicated with t_i, the rise in temperature of the electron gas can be found using the absorbed energy and Eq. (5.18). Using this temperature the changed dielectric constant simply follows from (5.16) giving a change in the the SPP resonance condition. With the new SPP response function we compute the convolution for this time step and we proceed in this fashion for every time step.

We performed two types of calculation. In one type we assumed that the electron gas thermalized infinitely fast. Experimentally this means that after thermalization, we are left with a hot electron gas, which can be described by a Fermi-Dirac distribution at a higher temperature than the lattice. In this

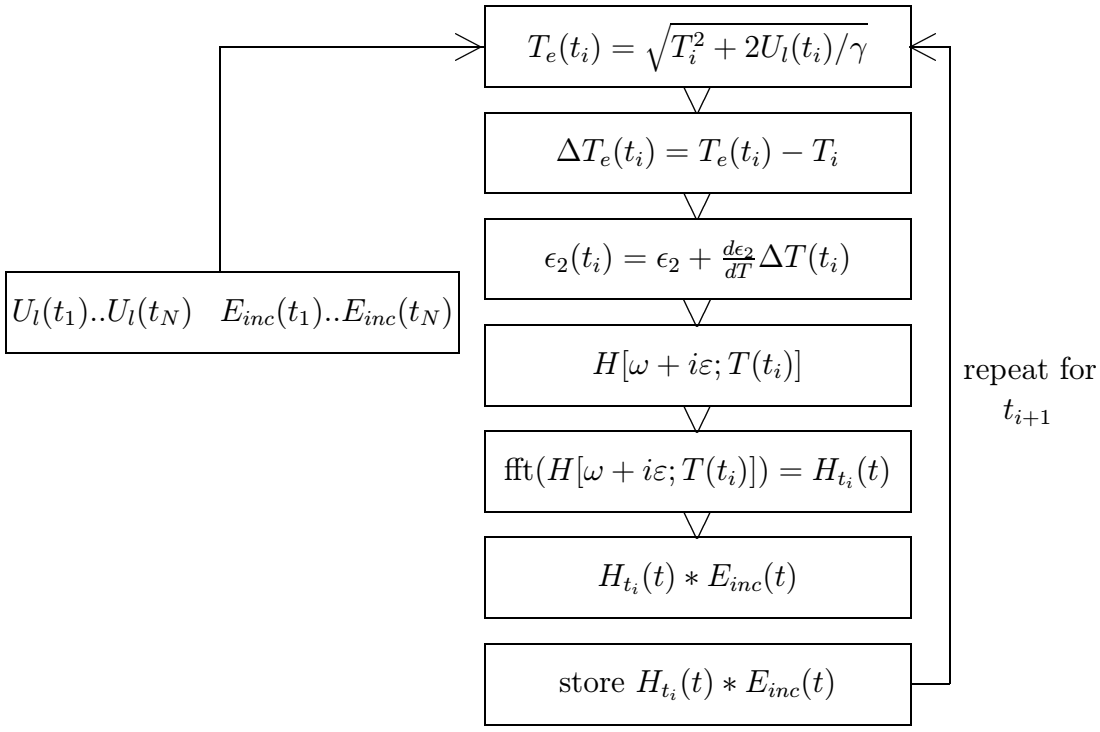

Figure 5.7: *Block diagram of our numerical calculations. In the numerical calculation the reflection of the pulse is performed in small time steps, indicated with t_i in this diagram. For each time step the rise in temperature of the electron gas due to absorption of light is stored in $T_e(t_i)$. The absorption of light is expressed in a deposited laser energy denoted by U_l (in Jm^-3). We assume that the change in the dielectric constant of the gold is proportional with the change in temperature of the electron gas $\Delta T_e(t_i)$. With this assumption we can calculate the dielectric constant and the response function of the SPP resonance at every time step in the frequency domain $H[\omega + i\varepsilon; T(t_i)]$. For every time step we transformed the response function to the time domain and calculated the convolution $H_{t_i}(t) * E_{inc}(t)$, where $E_{inc}(t)$ represents the incoming pulse. The convolution describes the reflected pulse.*

situation where the electron gas heats up no new resonant states are induced, as discussed above. This hot Fermi-Dirac distribution results in a change mainly in the real part of the dielectric constant of gold, similar to the results of Groeneveld [62]. For the real change of the dielectric constant we used a realistic value of $d\epsilon_r/dT = 8 \times 10^{-4} K^{-1}$. In the other type we assumed that the distribution of the electron gas is nonthermal within the pulse duration, due to the very slow thermalization. This very long thermalization time cor-

Figure 5.8: *Next page. (a) Results of our numerical calculations. The left plot is the pulse as function of time, with a dielectric constant which does not change in time and should be compared to the weak pulse in Fig. 5.6a. In the upper right plot we assumed that the dielectric constant changes due the rise of the temperature of the electron gas and that the thermalization is instantaneous which corresponds to a change in the real part of the dielectric constant. The lower right plot is the result with an infinitely slow thermalizing electron gas corresponding to an imaginary change of the dielectric constant. Qualitatively the latter result should compare to the strong pulse in Fig. 5.6b. (b) Deconvoluted simulations of the full response function* $H_t[\omega + i\varepsilon]$*. We have plotted the amplitude and the phase of the response function as a function of wavenumber for the pulse with a constant dielectric constant (dashed line) and a changing dielectric constant (solid line). This figure should compare directly with Fig. 5.6b.*

responds to the experimental situation where after excitation of the electrons new resonant interband transitions are induced which results in a change in the imaginary part of the dielectric constant. To describe this change in imaginary part we assume that it is proportional to the change of the temperature of a Fermi-Dirac distribution of the electron gas after dissipation of an energy U_l. To get reasonable agreement between the experimental and numerical results we used $d\epsilon_i/dT = 5.33K^{-1}$, which is surprisingly large.

The results of these two numerical simulations are shown in Fig. 5.8a where the pulse is shown as function of time. The left plot is the pulse after reflection from the Kretschmann geometry on SPPresonance conditions, with a constant dielectric constant. This plot must be compared to the weak pulse in the measurement (Fig. 5.6). The right upper plot is the situation where the electrons thermalize infinitely fast and the change is in the dielectric constant is real. We see that the change of the pulse form does not compare to the strong pulse in our measurements. The right lower plot is the situation for a an infinitely slow thermalizing electron gas and from comparison with our measurements we see a qualitative agreement. This indicates that the change in the dielectric constant is mainly imaginary, a change which can only be due to a non-equilibrium distribution of the electron gas. The latter result will be analyzed in more detail.

We have deconvoluted the numerical results similar to our experimental results, the results being shown in Fig. 5.8b. We have plotted the amplitude

a)

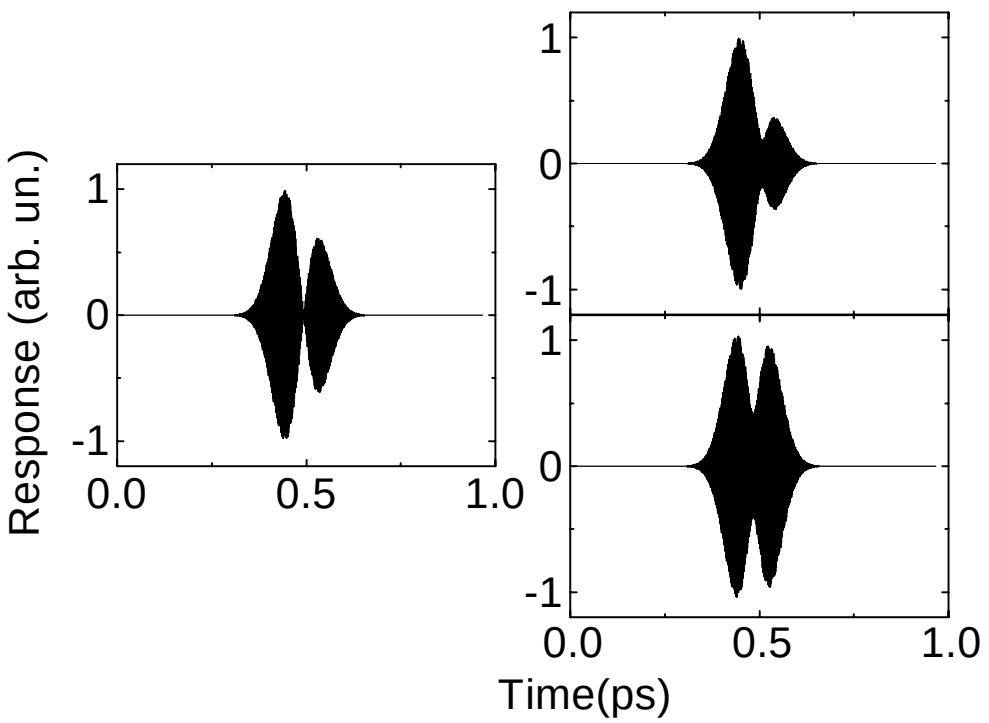
Response (arb. un.)
1
0
-1
0.0
0.5
1.0
Time(ps)

b)

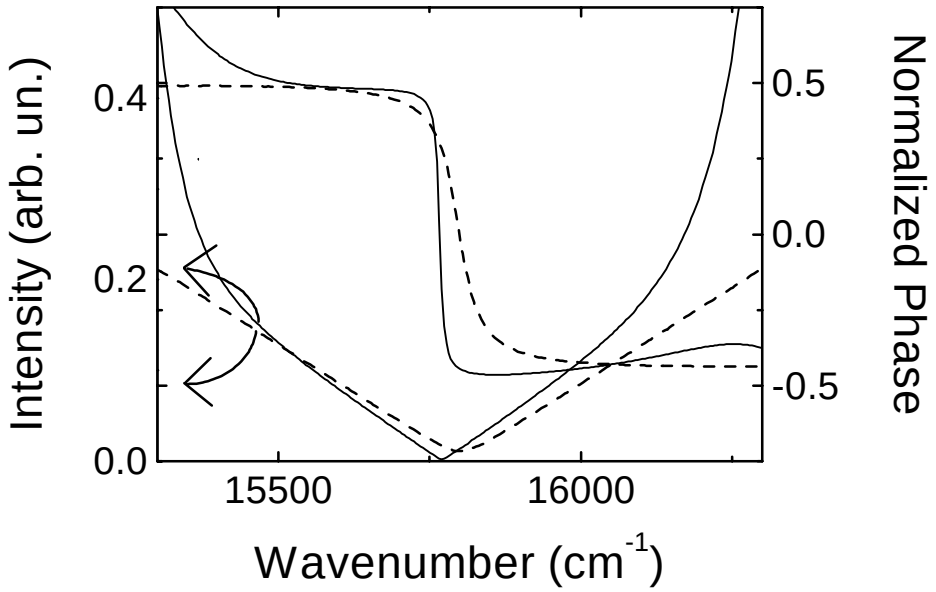
Intensity (arb. un.)
0.4
0.2
0.0
15500
16000
Wavenumber (cm-1)
0.5
0.0
-0.5
Normalized Phase

and phase as function of wavenumber of the full response function $H_{t_i}[\omega + i\varepsilon]$. This is done for both the weak (dashed line) and the strong pulse (solid line). Close inspection of the amplitude of the response function of the strong pulse shows a deviation from a straight line as observed in the response function of the weak pulse. In our experimentally obtained results we did not observe this deviation from a straight line in the amplitude, which is probably due the small bandwidth of the pulses used in the experiments. Close inspection of Fig. 5.8 shows that the deviations from linear behavior occur at approximately 500 cm^{-1} above or below the central frequency of the SPP resonance. From Fig. 5.6 we see that the total bandwidth of the laser corresponds to this number. Therefore we do not expect to see this deviation in our experimental results.

A point of great concern is the very large value of the change in the imaginary part of the dielectric constant. This value is four orders of magnitude larger than the value used by Groeneveld et al for the change in the real part of the dielectric constant. One might argue whether our extreme value for the change in the dielectric constant can be trusted. In the experiments by Groeneveld the contributions to the change of the dielectric constant are the tails of the dispersive part, however. We introduce new resonant states, which will drastically changes the value of the change in the dielectric constant. Another argument in favor of the large change could be that the contribution to the change in the dielectric constant is from two points in the zone scheme, whereas in the experiments of Groeneveld only one point contributed to the change.

The description of our measurements with a Fermi-Dirac distribution of the electron gas may also be the reason why a surprisingly large value for the change of the imaginary part of the dielectric constant has to be used to be able to get reasonable agreement with the experimental results. The large value suggests that the assumption of a Fermi-Dirac distribution of the electron gas is not correct and a nonthermal distribution has the be used, which confirms the results of Fann et al [63], who performed experiments on gold in a time resolved and energy resolved manner. In these experiments it was possible to measure directly the electron-energy distribution with a time resolution of approximately 200 fs, showing that the electrons did not thermalize at these timescales. The experimental work of Fann, clearly showed that the recorded spectra could not be described assuming a Fermi-Dirac distribution for very short times, which is clear evidence for a slow thermalization process from

a nonthermalized electron gas to a Fermi-Dirac distribution. In a later publication, calculations are presented based on a three-temperature model was assumed [64], which were used to describe the measurements. A temperature characterizing the thermal distribution of phonons, a temperature describing the thermal distribution of the electrons and a third temperature describing nonthermal distribution of hot electrons. It was shown, that this assumption properly accounted for the main features of the experiment.

Another point of concern is the shift of the central frequency of the SPP resonance. In the results of our numerical calculations we clearly see a shift to lower wavenumber. This shift is not confirmed convincingly by our experimental data.

5.5 Conclusions

We have experimentally studied the relaxation of a non-thermal electron distribution back to a thermalized electron gas in gold by comparing experimental results with numerical calculations. Using this comparison it has been shown that we can distinguish between a non-thermal and a hot thermalized electron gas. The change in the dielectric due to a hot thermal electron gas is due to Fermi level smearing and is real. A non-thermal electron gas induces new resonant states for interband transitions which gives a change in the imaginary part of the dielectric constant. Both changes shift the SPP resonance, but the shift due to Fermi level smearing is to lower wavenumber, whereas the induced resonant states shift the resonance to higher wavenumber. This mechanism makes it possible to distinguish between a thermal and a non-thermal electron gas by observing the shift.

The experimentally obtained results did not show a convincing shift of the SPP resonance. Furthermore, experimentally we did not found the typical deviation from the straight line near the resonance frequency as found from our numerical calculations. Further experiments are therefore needed to obtain convincing data confirming the numerically calculated shift.

Chapter 6

Light scattering by particles on a substrate

The subject of this chapter is to study the effect of the environment on the scattering properties of particles. Two type of experiments are performed: a continuous wave and a time-resolved measurement. The continuous wave type of experiment is performed on a sample consisting of a single particle on a substrate and the only disturbance of the scattering properties of the particle is by the substrate. The time-resolved measurement is performed on a 2D ordered sample. Here the influence on the scattering properties of the particles is by the surrounding particles and the substrate which supports the particle.

6.1 Introduction

Scattering of light by a particle can roughly be divided into three regimes. In this chapter we are interested in Mie scattering which is the intermediate regime between Rayleigh scattering and the geometrical optics scattering. Rayleigh scattering is the regime where the particle is much smaller than the wavelength of the light ($d/\lambda << 1$). The geometrical optics scattering regime, is the reversed situation of the Rayleigh limit, the particles are much larger than the wavelength of light ($d/\lambda >> 1$). For Mie scattering, the particles have a size in the order of the wavelength of the light that is scattered ($d/\lambda \approx 1$). The scattering properties of particles within this regime can be calculated analytically, known as Mie solutions [80]. The Mie solution describes the scattering problem of a single particle in a homogeneous medium and are given as

a series. Very recently, a comparison between experimental results and theory in the time domain for Mie scattering, has been reported [81].

In chapter 4 we found that time-resolved measurements of pulses through thin multiple-scattering slabs could not be described with transport theory. Experimentally we found a decrease in the diffusion coefficient of about 50 %. We argued that the decrease of the diffusion constant might be due to a reduction of the transport velocity and could be attributed to a position dependence of the scattering properties of the particles. The scattering properties are position dependent because these properties are not the properties of the particles, but of a particle within its surrounding. The subject of this chapter is to study experimentally the influence of nearby dielectric objects on the scattering properties of particles in the Mie regime.

Besides this interest, the measurements presented in this chapter are also of interest in near field optics. A well known example of near field optics is near-field optical microscopy. Normally in optics, one considers only the far field solutions. In the case of near-field optical microscopy, the field near the probe tip of the microscope which has a dimension typical in the order of the wavelength of the fields that are considered. In this sense, near-field optics has recently received considerable attention [82]. Also here we study effects on the near-field of a particle with dimensions of the order of the wavelength of the field.

We performed two types of experiments. In the first type of measurement we measure the angle dependent scattering of continuous wave light from a single particle on a substrate. In the second type of measurement we study the scattering of an ordered monolayer of monodisperse particles. The nearby objects in these experiments are other particles and a substrate supporting the particles. In these experiments an ultrashort pulse which has propagated through the ordered monolayer is recorded in a time-resolved fashion, employing the method described in chapter 3.

6.2 Scattering by a single particle on a substrate

6.2.1 Mie scattering, influence of substrate

The problem of calculating the scattering properties of a monochromatic plane wave by a spherical Mie particle in air is exactly solvable [43]. However, the

calculation is tedious. To get some insight in these calculations we discuss them very briefly and some important results. For details we refer to the book of van der Hulst [43] or Bohren [83]. The quintessence of the calculation is the expansion of the incoming plane wave in spherical harmonics. If the plane wave is expanded, the solution of the scattering problem can be found by applying the boundary conditions at the surface of the sphere. Important is the use of the spherical symmetry of the problem, as is the case for a particle in free space. The solution found from this calculation shows that the particles scatter light efficiently and anisotropically. A measure for the effectiveness of scattering is the cross section. The cross section of a particle is a virtual area perpendicular to the incoming beam through which the incoming flux is exactly equal to the total flux scattered by the particle. To show the effectiveness of this scattering we have plotted in Fig. 6.1 the cross sectionCross section of the particles as function of size parameter (kr), with r the radius of the particles and $k = 2\pi/\lambda$, the wavenumber of the scattered light in free space. The plotted cross section is scaled with the geometrical cross section, i.e. πr^2. We clearly see a strongly peaked resonant structure. Also clear from this picture is that the mean cross section is larger than the geometrical cross section, showing that the particle size seen by the light is much larger than the actual size of the particle.

When a plane interface is introduced near the scattering particle, the problem turns out to be much more difficult to deal with. For instance, the spherical symmetry of the problem, as used to obtain the Mie solution, does not hold anymore. Therefore, one has to rely on approximate solutions for some limiting cases [84, 85] or on numerical calculations.

6.2.2 Experiments and discussion of results

The Mie solutions show that the particles scatter light anisotropically. In this chapter we measure the anisotropic scattering of a particle on a substrate by recording an angular resolved scattering pattern. The obtained results will be compared with the Mie solutions.

The setup we used to obtain the angular resolved scattering pattern is tested by recording the scattering pattern from a multimode fiber (NRC FSV-10 single mode) in air. The fiber, with a diameter of 125 μm was stripped from its jacket. The refractive index of the fiber was measured before [87] and found to be 1.4603. In the experiments, we used an Ar^+ laser, operating single line at a wavelength of 514.7 nm. This beam is chopped with a frequency of 5 kHz

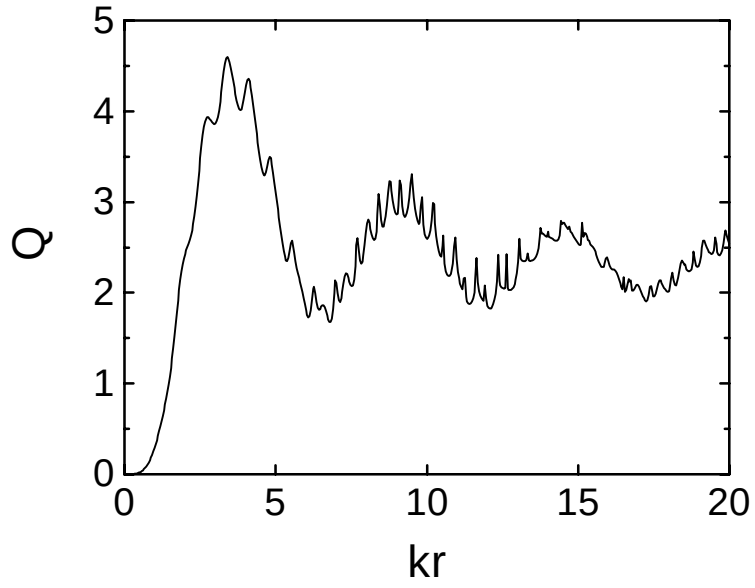

Figure 6.1: *Calculated cross section as function of size parameter using Mie theory. In the calculations an index of refraction of 1.59 is used (polystyrene). The cross section is normalized using the geometrical cross section.*

and is sent on the scatterer, and the scattered light is recorded as function of angle using a lock-in amplifier. The polarization of the Ar^+ was in the plane of scattering, the fiber was aligned perpendicular to the plane of scattering.

The result of a measurement is presented in Fig.6.2a, where the measured intensity (squares) is plotted as function of angle. The calculation of the scattering pattern by a cylinder is similar to the calculation of the scattering pattern by a Mie sphere. One difference, for instance, is in the symmetry of the problem. An extensive discussion about scattering of light by a cylinder is given in the book of Bohren [83], where an algorithm to calculate the pattern is also given. The result of a calculation based on this algorithm is also plotted in Fig. 6.2a (solid line), where the only free parameter is the diameter of the fiber. Both the calculated and measured intensity patterns are shown in Fig. 6.2a, showing that only slight deviations occur between the calculation and the measurement. For the diameter we found a value of 125.07 μm in excellent agreement with the value found in earlier experiments [87]. This measurement shows the reliability of the present setup in both the dynamic

range and angular resolving power. The differences between calculation and measurement might be due to deviations in the roundness of the fiber or the inhomogeneity of the refractive index of the fiber.

In the actual experiment a sample is prepared consisting of a single polystyrene particle (d=10 μm) on a quartz substrate. In the experiment the diameter of the beam was suppressed by a factor of 4 using a telescope. The suppression of the beam was introduced in order to get a high intensity. In the measurement the intensity of the scattered light is recorded as a function of angle. To test the reproducabilty of the method, the measurement was repeated. The results of these measurements are shown in Fig. 6.2b (circles and squares). We have tried to fit the recorded scattering pattern with Mie theory, the best result shown in this figure (solid line). Comparison of the calculated and measured scattering pattern shows that there are large differences as anticipated. Especially the peaks between 15 and 20 degrees show a large discrepancy. We conclude that the obtained results can not be described by Mie theory.

6.3 Scattering from a 2D array of Mie scatterers.

In this section we describe time-resolved measurements, which are performed employing the method described in chapter 3. We obtain information about the amplitude and phase of the response function describing the scattering properties of a 2D array consisting out of Mie particles on a substrate.

6.3.1 Theory of scattering by a 2D array

In this section we discuss scattering by a 2D array of Mie scatterers, similar to the formulation for X-ray scattering from 3D atomic crystals. This formulation of X-ray scattering can be found in many standard textbooks (see for instance [65]). We start with the description of the 2D lattice. Analogous to the Bravais lattice we define 2D lattice vectors:

$$\mathbf{R} = n_1\mathbf{r}_1 + n_2\mathbf{r}_2, \tag{6.1}$$

where n_i are integers. It will be clear that this vector $\mathbf{R}$ is an arbitrary step on the lattice for arbitrary n_i. The vectors $\mathbf{r}_i$ are the so called primitive vectors,

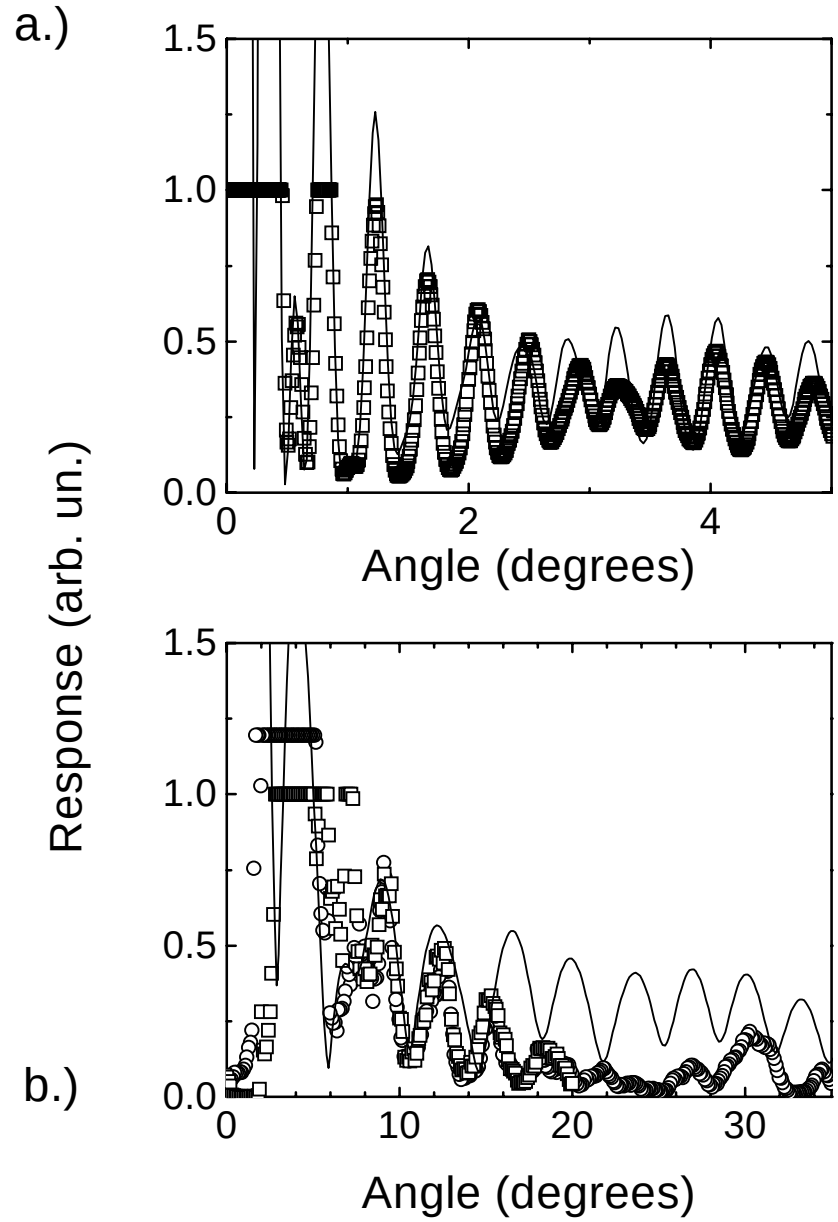

Figure 6.2: *(a) Measured angle-resolved scattering profile scattered by a multimode fiber with a thickness of 125 μm (squares) (p-polarized). The solid line in this figure is a Mie scattering profile for a cylinder with a diameter of 125.07 μm and an index of refraction of 1.4603 which is in excellent agreement with previous experiments [87]. (b) Measured angle-resolved scattering profile of a single scatterer with diameter of 10 μm made of polystyrene on a quarts substrate (squares and circles). The solid line is the best fit of a Mie scattering profile. Apparently the measured profile cannot be described by Mie scattering theory.*

which span up the lattice. Suppose a monochromatic wave is impinging on this lattice with wavevector $\mathbf{k}$ and scattered with wavevector $\mathbf{k}'$. Constructive interference will only occur if the von Laue condition is fulfilled:

$$(\mathbf{k} - \mathbf{k}') \cdot \mathbf{R} = 2\pi m, \tag{6.2}$$

where again $\mathbf{R}$ is a lattice vector, m an integer and $\mathbf{K} = \mathbf{k} - \mathbf{k}'$ is called the scattering vector.

The reciprocal lattice for these 2D ordered structures is defined analogous to the 3D atomic lattices and is characterized as the set of wavevectors $\mathbf{K}$ satisfying:

$$e^{i\mathbf{K}\cdot\mathbf{R}} = 1, \tag{6.3}$$

In this reciprocal lattice it is relatively easy to find the conditions for diffraction of a monochromatic wave. If we compare the von Laue condition with the definition of the reciprocal lattice we see that constructive interference only occurs if $\mathbf{K}$ is a vector of the reciprocal lattice, because exactly the wavevectors $\mathbf{K}$ defined by the von Laue condition (6.2) satisfy the definition of the reciprocal lattice (6.3). Using the definitions above, we find for the vectors $\mathbf{K}$ in the reciprocal lattice:

$$\mathbf{K} = h\mathbf{k}_1 + k\mathbf{k}_2 + \mathbf{k}_3, \tag{6.4}$$

where the integers h and k are the so called Miller indices, which identify a certain peak in the scattered intensity to a reciprocal lattice vector. The notation used for identifying a peak is done with the Miller indices and written as (hk). The difference with a 3D structure is in the vector $\mathbf{k}_3$, which defines lines extending to infinity perpendicular on the reciprocal lattice, through the point defined by the Miller indices.

A Bravais lattice is not enough to describe an array of scatterers. To complete the description a so called basis is needed. This basis is the unit that is repeated in space and is in our situation one spherical scatterer.

Approximately, the response function of our 2D array can be seen as a product of the scattering properties of the particles building up the 2D structure and the structure factor:

$$H^{(hk)}_{total}[\omega + i\varepsilon] = H_{Single}[\omega + i\varepsilon] H^{(hk)}_{Bravais}[\omega + i\varepsilon], \tag{6.5}$$

where $H_{Single}[\omega + i\varepsilon]$ is the response function describing the scattering properties of a single particle on a substrate and $H^{(hk)}_{Bravais}[\omega + i\varepsilon]$ the response function

describing the scattering by the structure as described above. This is a first example of a response function where we take outgoing wavevector into account. As shown in chapter 3 (Eq. (2.2)) the response function can be written as $H_{\mathbf{kk'}}$, where first subscript denotes the incoming wavevector and the second the outgoing wavevector. We consider the case where the the incoming direction is perpendicular to the plane of the 2D array. The wavevectors $\mathbf{kk'}$ are determined by the Miller indices (hk). The approximation we made to obtain (6.5) is in the scattering properties of the particles, for which we assumed that these properties are independent of the surrounding of the particles. The response function $H_{Single}[\omega + i\varepsilon]$ is given by the scattering properties of a single particle on a substrate.

6.3.2 Phase in a Bragg spot

The response function of a Bravais lattice $H^{(hk)}_{Bravais}[\omega + i\varepsilon]$ can be considered as the scattering from a two-dimensional grating. To calculate the response function, we will consider the amplitude and phase separately. We use the analogy with a grating to obtain an approximate expression for both the amplitude and phase in a Bragg spot. We consider a one-dimensional grating with a grating constant d and define analogous to the reciprocal lattice $\Lambda = 2\pi/d$. We assume that the diffraction occurs in the XY-plane and that the grating is located along the X-axes. Also here the condition for constructive interference is given by the von Laue condition:

$$\mathbf{K} \cdot \hat{\mathbf{x}}\, d = 2\pi m, \tag{6.6}$$

where again $\mathbf{K} = \mathbf{k} - \mathbf{k'}$ the scattering vector, $\hat{\mathbf{x}}$ a unit vector along the X-axes and m an integer giving the order of scattering which can be compared to the Miller indices in case of the 2D array. Also here constructive interference occurs only if the scattering vector $\mathbf{K}$ is a vector of the reciprocal lattice: $m\Lambda\hat{\mathbf{x}}$. From Eq. (6.6) the well known grating formula follows straightforwardly, which relates the angle of incidence of the light γ, the angle of scattering θ and the grating constant:

$$\sin\gamma + \sin\theta = \frac{m\lambda}{d}, \tag{6.7}$$

The origin of scattering from both the grating and 2D ordered structure is diffraction. In our experiments we study only first-order scattering peaks which corresponds with $(hk) = (01)$ in case of a 2D array and $m = 1$ for a one-dimensional grating. The amplitude and phase in the Bragg spot are recorded

employing the method described in chapter3. We approximate the phase in a Bragg spot of a 2D array by the phase found in literature for a grating [86]:

$$\arg H^{(01)}_{Bravais}[\omega + i\varepsilon] = -\frac{2\pi^2 bc(\omega - \omega_0)^2}{\omega_0^3 d^2 \cos^2\theta}, \tag{6.8}$$

where ω_0 is the central frequency of the incident pulse and b the slant distance from the grating. The amplitude of the response function $|H^{(01)}_{Bravais}[\omega + i\varepsilon]|$ describes the diffraction and attenuation of the beam. For our purpose it is sufficient to consider the attenuation as a constant as function of wavelength in the region of interest in our experiments. As we will show experimentally this approximation appears to be good approximation. So the phase $\arg|H^{(01)}_{Bravais}[\omega + i\varepsilon]|$ will be the only function of interest in our experiments. As can be seen from Eq. (6.8) the phase of a pulse scattered from the 2D structure or a grating depends linearly on the distance b. The physical origin of this phase or chirp is angular dispersion for which it was shown that the phase is mainly quadratic in frequency [86].

The sign of the phase expressed in Eq. (6.8) is opposite to the phase or chirp acquired due to propagation through optical components as shown in Eq. (5.9). This property of a grating can be used to compensate for the acquired chirp due to propagation through optical components. Using a grating pair, where the second grating is used to recollimate the beam, the acquired chirp can be compensated, by tuning the distance between the gratings. In the literature it is described how gratings can be used to compress ultrashort optical pulses [86]

One might wonder how it is possible to have a response function with an amplitude which is a constant as function of frequency and a phase which exhibits structure, without violating the Kramers-Kronig relations between amplitude and phase. However, the situation we described above is similar to the situation of the response function of the Gires-Tournois interferometer described in chapter 2, where we discussed the fact that these violations are due to the approximations made. Here the apparent violation of the Amplitude-Phase relations is due to the approximation of the amplitude by a constant as function of frequency.

6.3.3 Preparation of the samples

The samples used in these experiments consist of a hexaganol closed packed monolayer of monodisperse particles on a quarts substrate. The particles are

made of polystyrene ($n = 2.7$) with a diameter of 2.013 μm $\pm$ 1%.

A way of preparing samples of small particles with ordering over large distances is described in an article by Dushkin [88]. In this method a glass substrate is used which is cleaned by washing it with chromic acid and after that with water and soap. This is done very carefully to get a good wetting surface. After cleaning, a glass cylinder is mounted on the glass substrate, using wax. Typical sizes of the container made in this way are: diameter cylinder 10 mm, height cylinder 10 mm, thickness substrate 5 mm. This container is filled with a suspension, which contains 5% solids. The liquid of the suspension evaporates and there is always a thinner layer of fluid in the middle of the container than at the periphery of the container due to the subconcave meniscus. After some time in the middle of the container the particles touch the bottom of the container and a nucleation for crystal growth forms. It is believed that the particles attract each other due to an interface force [89] and crystal growth starts. The mechanism of transport of particles from the edge of the container is believed to happen by convective fluid flow [90]. In this way it was possible to grow 2D ordered structures of colloidal particles. The typical size of the structures varied in the order of 25 times the particle size squared (area) up to a 100 times the particle size. A sample consists after growing out of a polycrystalline monolayer.

6.3.4 Time-resolved measurements

The scattering of light from these samples only occurs in certain directions, known as Bragg spots as shown earlier. To be able to measure the transfer function of the sample we employed the method as described in chapter 3. The Mach-Zehnder interferometer was aligned in such a way that one of the double pulses is a Bragg spot scattered from the 2D ordered sampleand we record the autocorrelation function of the double pulse, where one of the pulses is scattered by 2D ordered sample.

A result of a measurement is shown in Fig. 6.3. We have plotted the recorded phase (circles) and amplitude (dashed line) of the response function (6.5). If we compare the measured spectrum of the Bragg spot with the spectrum of the laser (Fig. 3.3b), we see that the spectra coincide, showing that the approximation of a constant amplitude of the response function is valid within our wavelength interval. The solid line in this figure represents the theoretical phase of the response function (6.8). The parameters used are:

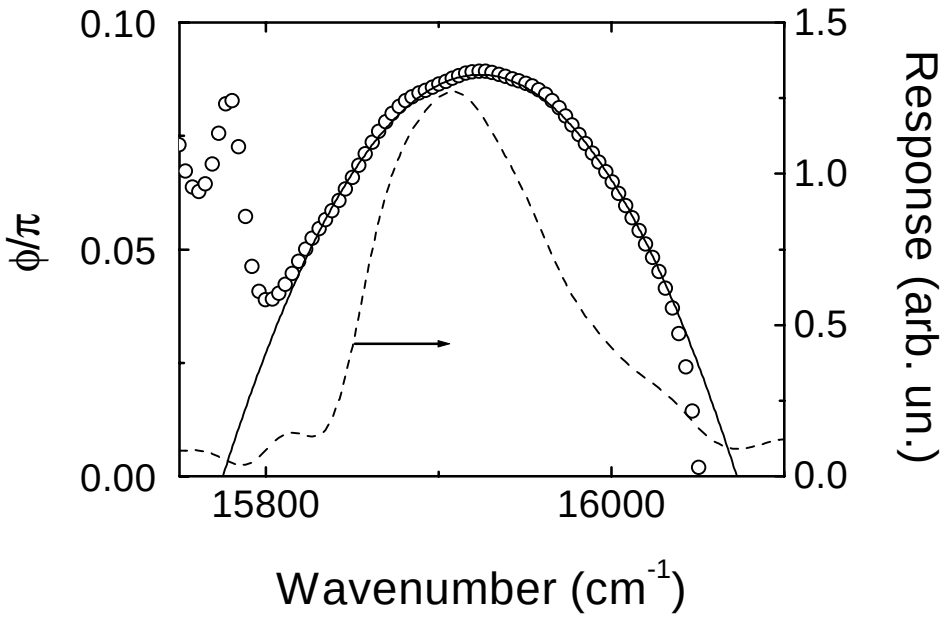

Figure 6.3: *Measurement of the amplitude (dashed line) and phase (circles) of the light scattered by a 2D ordered sample. The solid line in this figure is the phase of the response function (6.8) only. The errorbar is in the order of ten times the symbol size.*

$d = 2 \times 10^{-6}$, the diameter of the particles building up the 2D structure, and $b = 2$ m in reasonable agreement with our experimental situation. The calculated phase is in excellent agreement with the experimental results, suggesting that the response function $H_{Single}[\omega + i\varepsilon]$ does not contribute to the *total* response function (6.5). Unfortunately, this means that the deviation of the Mie scattering pattern induced by the substrate cannot be obtained from these measurements.

6.4 Discussion and conclusions

We performed two types of experiments to study the influence of a macroscopic dielectric object on the single scattering properties of monodisperse latex particles with a diameter in the order of the wavelength of the scattered light. In this scattering regime we expect strong the resonances in the scattering properties of the particles to be perturbed by the presence of nearby macroscopic

dielectric objects. These resonances can be studied by recording the scattered light. In one type of measurement we studied the stationary angle-resolved scattering of continuous wave laser light by a single particle on a substrate.

In the other type of experiment we studied the scattered light by a time-resolved measurement of the scattering of an ultrashort pulse. In both experiments the scattered light did not show the characteristics typical for light scattered by Mie particles. Unfortunately, from the time-resolved measurement no information could be gained about the influence of the surrounding of a particle on its scattering properties.

The angle resolved measurements demonstrates quantitatively that the scattering properties of a particles is largely influenced by the substrate. This is also a clear demonstration that the t-matrix, describing the scattering properties of a particle, is a quantity depending on the scatterer and on its surrounding. The influence of nearby dielectric objects on the scattering properties of particles of the size in the order of the wavelength of light is has recently received a lot of interest in near-field optics.

To make a quantitative comparison between the experimentally obtained results and theory is very difficult, the reason being that no theory is available for our specific experimental situation. The presented measurements in this chapter show that indeed the scattering properties are distorted by nearby objects and that more theory is needed to make quantitative predictions about these distortions.

Appendix A

Temperature effects

To be able to see any effects of the non-equilibrium distribution of the electrons, we had to focus the beam to get a large dissipation of energy in a small volume. One of the major problems with focusing is the heating of the gold film. In this appendix we present the results of an experimental study of these heating effects.

Earlier experiments performed on silver by Groeneveld et al. [62], were also done with a focused light beam. In these experiments two lenses are used, identical to the experiments we described in chapter 5. One of these lenses is used to focus the light, and the other is used to collect the reflected light. This focusing of the light beam has two major disadvantages, one of these is the large angular spread, due to which the reflection of the pulse has a spread around the resonant angle. A slit is used to select only those angles that are near the resonant angle to excite the SPP. The other problem is dissipation of energy which occurs in a small volume, and heats up of the sample and results in a change of the SPP resonance.

The experimental set up we used to study the heating effect is shown in Fig. A.1. The light beam from the CPM-laser is focused and collected as discussed above. The focal length of the focusing lens is 25.4 mm, the collecting lens has a focal length of 100 mm. With the spectrometer we measure the autocorrelation function of the reflected pulses at different light intensities. The detected intensity is integrated over long times compared to the timescales involved with electron dynamics as described in chapter 5, so we measure stationary properties. In one measurement we averaged over 256 scans, and the resolution of one scan was 0.25. The Fourier transforms of the autocorrelation function of two measurements at two different intensities are shown in Fig. A.2.

We clearly see that resonance frequency shifts to lower wavenumber for lower intensity.

This effect of shifting of the resonance frequency due to heating has been measured before by van Exter [74] and his results could be understood by considering two effects. The first effect was the change in density of the electron plasma, which has an effect on the plasma resonance frequency. This plasma resonance frequency is given by:

$$\omega_p = \sqrt{\frac{ne^2}{\epsilon_0 m}}, \tag{A.1}$$

where ω_p is the plasma resonance frequency, n the electron density, e the electron charge, and m the electron mass. Due to heating the lattice will expand, and a change in the plasmon resonance can be expected. The complete Drude contribution to the dielectric constant is given by:

$$\epsilon_{free}(\omega) = -\frac{\omega_p^2}{(\omega^2 + i\omega\Gamma)}, \tag{A.2}$$

where Γ is the damping rate of the plasmons due to electron-phonon scattering. This is the other parameter that changes due to heating and will be mainly due to a change in the phonon spectrum.

The calculation performed by van Exter was for silver. We repeated the calculation for gold. We start with the Drude contribution to the dielectric constant, which can be approximated:

$$\epsilon_{Drude}(\omega) = -\frac{\omega_p^2}{(\omega^2 + i\omega\Gamma)} = \frac{\omega_p^2}{\omega^2} + \frac{\omega_p^2\Gamma^2}{\omega^4} + i\frac{\omega_p^2\Gamma}{\omega^3}. \tag{A.3}$$

In this equation the real and imaginary parts are separated. The second term in the real part of this equation is small compared to the first term at visible wavelengths, and can therefore be neglected. With this assumption, the two temperature effects separate in:

$$\frac{d\epsilon}{dT} = \left(\frac{\partial\epsilon_r}{\partial n}\right)\frac{dn}{dT} + \left(\frac{\partial\epsilon_i}{\partial\Gamma}\right)\frac{d\Gamma}{dT}. \tag{A.4}$$

The first term in this equation is a pure expansion effect. This expansion is frustrated in lateral direction by the surrounding gold metal film. We calculated the change in the real part of the dielectric constant to be $2.7 \times 10^{-4} K^{-1}$. The second term in Eq. (A.4) is a pure heating effect. We estimated this effect, using the measurements done by Ujihara [75] to be $5.7 \times 10^{-4} K^{-1}$.

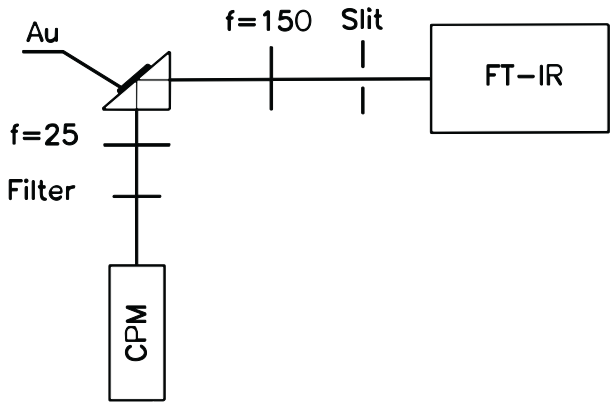

Figure A.1: *Experimental set up for measuring the heating of the sample caused by energy dissipation in the film. L:lens, S:slit, CPM: Colliding-Pulse Modelocked laser, FT-IR: Fourier-tranform Infrared Spectrometer. The focal length of lens 1 is 25.4 mm, the focal length of lens 2 is 100 mm.*

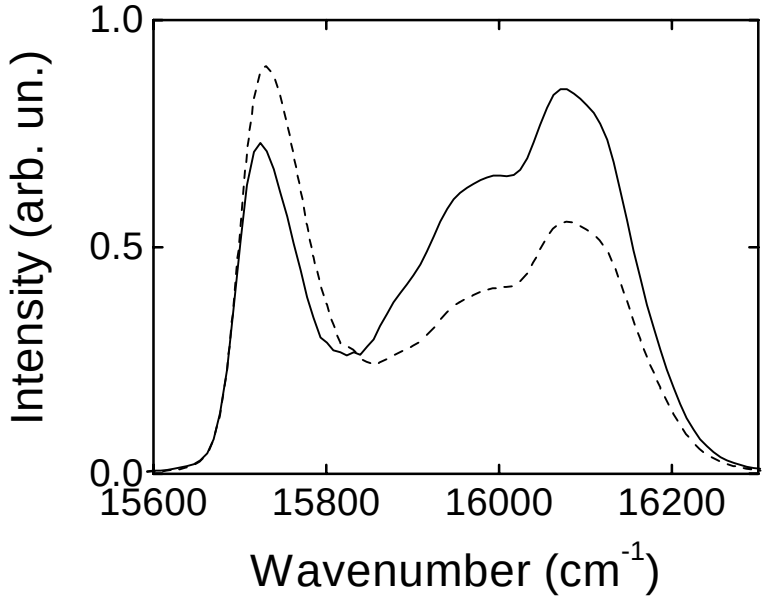

Figure A.2: *Power spectra of the reflected pulse of two measurements done at two different intensities. The solid line is measured with an intensity of 8 mW, the dashed line with 22 mW. We clearly see the shift of the SPP resonance frequency to lower wavenumber for lower intensity.*

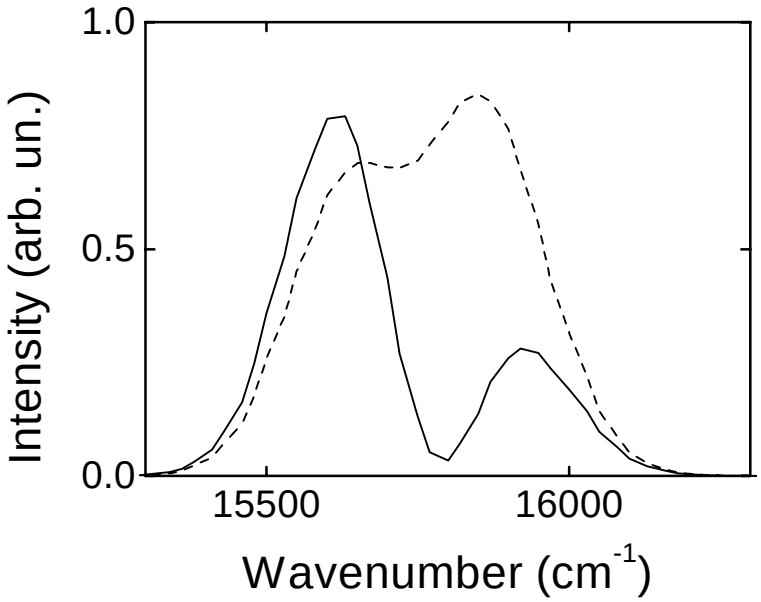

Figure A.3: *Calculated power spectrum of a reflected pulse at SPP resonance conditions. Two lines are shown: The solid line calculated for the gold film at room temperature* ($300K$) *and one dashed line which was calculated for a temperature rise of* $300K$. *We clearly see a shift of the resonance condition to lower wavenumber with increasing temperature.*

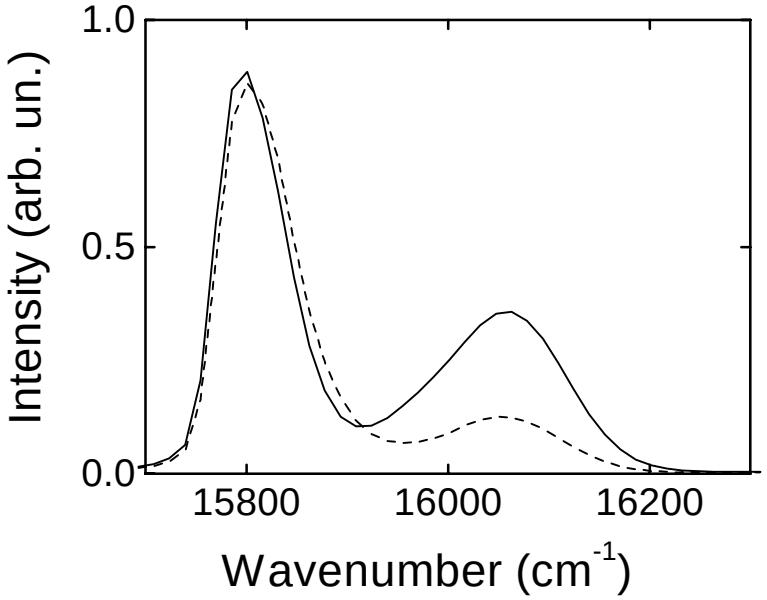

Figure A.4: *Experimentally obtained power spectra of reflected pulses. The pulses were reflected at SPP resonance conditions. The solid line was measured at room temperature, the dashed line is measured at* $600K$. *We clearly see a shift of the resonance condition to higher wavenumber with increasing temperature.*

With these results for the change of the dielectric constant with temperature we calculated the change in the resonance frequency for a temperature rise of $300K$. The result is plotted in Fig. A.3. From this plot we see that the SPP resonance frequency shifts to lower wavenumber with increasing temperature, opposite to the obtained experimental results.

To get more insight in this effect we performed some additional experiments, where the light beam was not focused on the film but we simply heated the gold film. One of the measurements was performed at room temperature and one where the film was heated approximately $300K$. Again we recorded an autocorrelation function of the reflected pulses at resonance with the SPP. We averaged over 256 scans, with a resolution of 0.25. The power spectra of these measurements are shown in Fig. A.4.

In this appendix we described two type of experiments. In one type we measured the SPP resonance, integrated over long times, at high light intensities. The other type is performed at low intensities, but here we heated the metal. Comparing the results of these two type of measurements shows that the SPP resonance changes due to heating. Furthermore these experiments show that high intensities the metal heats up, due to dissipation of energy. This heating results in a change of the SPP resonance. In contrast to experiments on silver, we could not interpret the heating effects with a simple model

Bibliography

[1] A.A. Michelson, 'Interference phenomena in a new form of refractometer', Phil. Mag. **5**, 236 (1882).

[2] A.A. Michelson, 'On the application of interference methods to astronomical measurements', Phil. Mag. **34**, 280 (1892).

[3] A.A. Michelson, *Light Waves and Their Uses* (University of Chicago Press, Chicago, 1902).

[4] R.Kronig, 'On the theory of dispersion of X-rays', J. Opt. Soc. Amer. **12**, 547 (1926).

[5] H.A. Kramers, *Estratto dagli Atti del Congresso Internazionale di Fisici Como* (Nicolo Zonichello, Bologna, 1927).

[6] R. Kronig, 'Algemeene theorie der diëlectrische en magnetische verliezen', Ned. Tijdschr. Natuurk. **9**, 402 (1942).

[7] M. Beck, I.A. Walmsley, and J.D. Kafka, 'Group Delay Measurements of Optical Components Near 800 nm', IEEE J. Quantum Electron. **27**, 2074 (1991).

[8] M. Born and E. Wolf, *Principles of Optics*, 6th ed. (Pergamon Oxford, 1986).

[9] *Image recovery: Theory and applications* H. Stark ed. (Academic Press, New York, 1987).

[10] K. Tamasaku, Y. Nakamura, and S. Uchida, 'Charge dynamics across the CuO_2 planes in $La_{2-x}Sr_xCuO_4$', Phys. Rev. Lett. **69**, 1455 (1992); C.C. Homes, T.Timusk, R. Liang, D.A. Bonn, and W.N. Hardy, 'Optical conductivity of c-axis oriented $YBa_2Cu_3O_6$.70: evidence for a Pseudogap', Phys. Rev. Lett. **71**, 1645 (1993); H.S. Somal, B.J. Feenstra, J.

Schützmann, Jea Hoon Kim, Z.H. Barber, V.H.M. Duijn, N.T. Hien, A.A. Menovsky, Mario Palumbo, and D. van der Marel, 'Grazing incidence infrared reflectivity of $La_{1.85}Sr_{0.15}CuO_4$ and NbN', Phys. Rev. Lett. **76**, 1525 (1996).

[11] Jae H. Kim, B.J. Feenstra, H.S. Somal, D van der Marel, Wen Y. Lee, A.M. Gerrits, and A. Wittlin, 'c-axis infrared response of $Tl_2Ba_2Ca_2Cu_3O_{10}$ studied by oblique-incidence polarized-reflectivity measurements', Phys. Rev. B **49**, 13065 (1994).

[12] M.H. Lee, O.I. Sindoni, 'Kramers-Kronig relations with logarithmic kernel and application to the phase spectrum in the Drude model', Phys. Rev. E **56**, 3891 (1997).

[13] D. Forster *Hydrodynamic Fluctuations, Broken Symmetry, and Correlation Functions* (W.A. Benjamin Inc., Massachusetts, 1975).

[14] D. Grischkowsky, C.-C. Chi, I.N. Duling, W.J. Gallagher, M.B. Ketchen and R. Sprik, 'Spectroscopy with Ultrashort Electrical Pulses' in *Laser Spectroscopy VIII*, W. Persson and S. Svanberg eds. (Springer-Verlag, New York, 1987).

[15] B. Harbecke, 'Application of Fourier's Allied Integrals to the Kramers-Kronig Transformation of Reflectance data', Appl. Phys. A **40**, 151 (1986). Note that in this article it is assumed that the transfer function is a nonzero function in the upper half frequency plane.

[16] N.G. van Kampen, 'S-matrix and Causality Condition I. Maxwell Field', Phys. Rev. **89**, 1072 (1953).

[17] John S. Toll, 'Causality and the Dispersion Relation: Logical Foundations', Phys. Rev. **104**, 1760 (1956).

[18] We consider the case that no absorption anomalies are present in our response functions. These anomalies would give rise to extra factors in Eq.2.17, also see [17].

[19] R. Nevanlinna, *Eindeutige Analytische Funktionen*, 2th ed. (Springer-Verlag Berlin 1953).

[20] D.Y. Smith, 'Dispersion relations for complex reflectivities', J. Opt. Soc. Am. **67**, 570 (1977).

[21] R.G. Newton, *Scattering theory of Waves and Particles*, 2th ed. (Springer-Verlag, Heidelberg 1982).

[22] A.A. Clifford, M.I. Duckels and B. Walker, 'Reflectance Phase-shift Dispersion Relations', J. Chem. Soc. (London) Faraday Trans. II **68**, 407 (1972).

[23] J. Chamberlain, 'Phase modulation in far infrared (submillimetre-wave) interferometers. I-mathematical formulation', Infrared Phys. **11**, 25 (1971).

[24] W.H. Knox, N.M. Pearson, K.D. Li, and C.A. Hirlimann, 'Interferometric measurements of femtosecond group delay in optical components', Opt. Lett. **13**, 574 (1988).

[25] A.E. Siegman, *Lasers* (University Science Books, California, 1986).

[26] M. Beck and I.A. Walmsley, 'Measurement of group delay with high temporal and spectral resolution', Opt. Lett. **15**, 492 (1990).

[27] K. Naganuma, K. Mogi, and H.Yamada, 'Group-delay measurement using the Fourier transform of an interferometric cross-correlation generated by white light', Opt. Lett. **15**, 393 (1990).

[28] K. Naganuma and Y. Sakai, 'Interferometric measurement of wavelength dispersion on femtosecond laser cavities', Opt. Lett. **19**, 487 (1994).

[29] K. Naganuma, 'Semiconductor laser cavity dispersion measurement based on interferometric cross-correlation of amplified spontaneous emission', Appl. Phys. Lett. **64**, 261 (1994).

[30] F. Schuurmans, Private communication.

[31] F. Stern, 'Elementary theory of the optical properties of solids', Solid State Phys. **15**, 299 (1963).

[32] R.H. Young, 'Validity of the Kramers-Kronig transformation used in reflection spectroscopy', J. Opt. Soc. Am. **67**, 520 (1977).

[33] W.H. Press, S.A. Teukolsky, W.T. Vetterling, B.P. Flannery, *Numerical Recipes in Fortran* (Cambridge University Press, Cambridge, 1992).

[34] P.W. Anderson, 'Absence of diffusion in certain random lattices', Phys. Rev. **109**, 1492 (1958).

[35] D.S. Wiersma, P. Bartolini, A. Lagendijk, R. Righini, 'Localization of light in a disordered medium', Nature **390**, 671 (1997).

[36] S. John, 'The localization of light and other classical waves in disordered media', Comments Condens. Matter Phys. **14**, 193 (1988).

[37] P. Sheng, *Introduction to Wave Scattering, Localization, and Mesoscopic Phenomena* (Academic Press, New York 1995).

[38] M.R. Hee, J.A.Izatt, J.M. Jacobson, and J.G. Fujimoto, E.A. Swanson, 'Femtosecond transillumination optical coherence tomography', Opt. Lett. **18**, 950 (1993).

[39] S. Chandrasekhar, *Radiative Transfer* (Dover, New York, 1960).

[40] A. Ishimaru, *Wave Propagation and Scattering in Random Media*, Vols. 1 and 2 (Academic, New York, 1978).

[41] J.M. Drake, A.Z. Genack, 'Observation of nonclassical optical diffusion', Phys. Rev. Lett. **63**, 259 (1989).

[42] M.B. van der Mark, M.P. van Albada, A. Lagendijk. 'Light scattering in strongly scattering media: multiple scattering and weak localization', Phys. Rev. B **37**, 3575 (1988).

[43] H.C. van de Hulst, *Multiple Light Scattering*, Vols. 1 and 2 (Academic, New York, 1980).

[44] A. Lagendijk, R. Vreeker, and P. de Vries, 'Influence of internal reflection on diffusive transport in strongly scattering media', Phys. Lett. A **136**, 81 (1989).

[45] J.X. Zhu, D.J. Pine, and D.A. Weitz, 'Internal reflection of diffusive light in random media', Phys. Rev. A **44**, 3948 (1991).

[46] D.J. Durian, 'Influence of boundary reflection and refraction on diffusive photon transport', Phys. Rev. E **50**, 587 (1994).

[47] L.Tang, A. Ishimaru, 'Theory of backscattering enhancement of random discrete isotropic scatterers based on the summation of all ladder and cyclical terms', J. Opt. Soc. Am. A **2**, 1331 (1985).

[48] T.R. Kirkpatrick, 'Localization of acoustic waves', Phys. Rev. B **31**, 5746 (1985).

[49] J.F. de Boer, *Optical fluctuations on the transmission and reflection of mesoscopic systems* (PhD thesis, Universiteit van Amsterdam, 1995).

[50] A. Lagendijk and B.A. van Tiggelen, 'Resonant multiple scattering of light', Phys. Rep. **270**, 143 (1996).

[51] P.N. den Outer and A. Lagendijk, 'Influence of the refractive index contrast on coherent backscattering', Opt. Comm. **103**, 169 (1993).

[52] J. Gómez Rivas, private communication.

[53] M.P. van Albada and A. Lagendijk, 'Observation of weak localization of light in a random medium', Phys. Rev. Lett. **55**, 2692 (1985); P.E. Wolf and G. Maret, 'Weak localization and coherent backscattering of photons in disordered media', Phys. Rev. Lett. **55**, 2696 (1985).

[54] K.M. Yoo, Feng Liu, R.R. Alfano, 'When does the Diffusion Approximation Fail to describe Photon transport in Random Media', Phys. Rev. Lett. **64**, 2647 (1990).

[55] Z.-Q. Zhang and Ping Sheng in: C.M. Soukoulis, editors, *Photonic Band Gap Materials*, Proceedings of the NATO Advanced Study Institute on Photonic Band Gap Materials, Elounda, Crete, Greece, June 18-30, 1995.

[56] Th.M. Nieuwenhuizen and J.M. Luck, 'Skin layer of diffusive media', Phys. Rev. E. **48**, 569 (1990).

[57] J. Hohlfeld, J.G. Muller, S.S. Wellershoff, E. Matthias, 'Time-resolved thermoreflectivity of thin gold films and its dependence on film thickness', Appl. Phys. B **64**, 387 (1997).

[58] C. Suarez, W.E. Bron, T.Juhasz, 'Dynamics and transport of electronic carriers in thin gold films', Phys Rev. Lett. **75**, 4536 (1995).

[59] G.L. Easley, 'Observation of nonequilibrium heating in Copper', Phys. Rev. Lett. **51**, 2140 (1983); 'Generation of nonequilibrium electron and lattice temperature in copper by picosecond laser pulses', Phys. Rev. B **33**, 2144 (1986).

[60] R.W. Schoenlein, W.Z. Lin, J.G. Fujimoto, and G.L. Easley, 'Femtosecond studies of nonequilibrium electronic processes in metals', Phys. Rev. Lett. **58**, 1680 (1987).

[61] H.E. Elasayed-Ali, T.B. Norris, M.A. Pessot, and G.A. Mourou, 'Time-resolved observation of electron-phonon relaxation in Copper', Phys. Rev. Lett. **58**, 1212 (1987).

[62] R.H.M. Groeneveld, R. Sprik, and A. Lagendijk, 'Ultrafast relaxation of electrons probed by surface plasmons at a thin silver film', Phys. Rev. Lett. **64**, 784 (1990); R.H.M. Groeneveld, R. Sprik, and A. Lagendijk, 'Effect of a nonthermal electron distribution on the electron-phonon energy relaxation process in noble metals', Phys. Rev. B **45**, 5079 (1992); R.H.M. Groeneveld, R.Sprik, and A. Lagendijk, 'Femtosecond spectroscopy of electron-phonon energy relaxation in Ag and Au', Phys. Rev. B **51**, 11433 (1995).

[63] W.S. Fann, R. Storz, H.W.K. Tom and J. Bokor, 'Direct measurement of nonequilibrium electron-energy distributions in subpicosecond laser-heated gold films', Phys. Rev. Lett. **68**, 2834 (1992).

[64] W.S. Fann, R. Storz, H.W.K. Tom, and J. Bokor, 'Electron thermalisation in gold', Phys. Rev. B **46**, 13592 (1992).

[65] N.W. Ashcroft and N.D. Mermin, *Solid State Physics* (Saunders College, Philadelphia 1976).

[66] D. Shoenberg, 'The Fermi surfaces of Copper, Silver, Gold. I. The De Haas-van Alphen effect', Phil. Trans. Roy. Soc. **255**, 85 (1962); D.J. Roaf, 'The Fermi surfaces of Copper, Silver, Gold. II. Calculation of The Fermi Surface', Phil. Trans. Roy. Soc. **255**, 135 (1962).

[67] R. Rosei and D.W. Lynch, 'Thermomodulation spectra of Al, Au, and Cu', Phys. Rev. B **5**, 3883 (1972).

[68] R. Rosei, F. Antonangeli, and U.M. Grossano, 'd bands position and width in gold from very low temperature thermomodulation measurements', Surf. Sci. **37**, 689 (1973).

[69] M.L. Theye, 'Investigation of the optical properties of Au by means of thin semi-transparent films', Phys. Rev B **2**, 3060 (1970).

[70] R.F. Wallis, G.I. Stegeman, *Electromagnetic surface excitations* (Springer, Berlin 1986).

[71] E. Kretschmann, 'Die Bestimmung optischer Konstanten von Metallen durch Anregung von Oberflächenplasmaschwingungen', Z. Physik **241**, 313 (1971).

[72] Schott catalog, Optical glass.

[73] J.C.M. Diels, J.J Fontaine, I.C. Micheal, F. Simoni, 'Control and measurement of ultrashort pulse shapes (in amplitude and phase) with femtosecond accuracy', Appl. Opt. **24**, 1270 (1985).

[74] M. van Exter, *Ultra-fast spectroscopy of vibrational excitations and surface plasmons* (PhD thesis, Universiteit van Amsterdam, Amsterdam 1988).

[75] K. Ujihara, 'Reflectivity of metals at high temperatures', J. Appl. Phys. **43**, 2376 (1972).

[76] N.E. Christensen and B.O. Seraphin, 'Relativistic band calculation and the optical properties of gold', Phys. Rev. B **4**, 3321 (1972).

[77] M. Guerrisi, R. Rosei, and P. Winsemius, 'Splitting of the interband absorption edge in Au', Phys. Rev. B **12**, 557 (1975).

[78] P. Winsemius, M. Guerissi, and R. Rosei, 'Splitting of the interband absorption edge in Au: temperature dependence', Phys. Rev. B **12**, 4570 (1975).

[79] R. Rosei, 'Temperature modulation of the optical transitions involving the Fermi surface in Ag: Theory', Phys. Rev. B. **10**, 474 (1974).

[80] G. Mie, 'Beitrage zur Optik trüber Medien speziell kolloidaler Metallösungen', Ann. Phys. **25**, 377 (1908).

[81] R.A. Cheville, R.W. McGowan, D. Grischowsky, 'Time resolved measurements which isolate the mechanisms responsible for terahertz glory scattering from dielectric spheres', Phys. Rev. Lett. **80**, 269 (1998).

[82] Ch. Fischer, D.W. Pohl, 'Observation of single-particle plasmons by near-field optical spectroscopy', Phys. Rev. Lett. **62**, 458 (1989).

[83] C.F. Bohren and D.R. Huffman, *Absorption and scattering of light by small particles* (John Wiley & Sons, New York, 1983).

[84] E. Fucile, P. Denti, F. Borghese, R. Saija, O.I. Sindoni, 'Optical properties of a sphere in the vicinity of a plane surface', J. Opt. Soc. Am. A **14**, 1505 (1997).

[85] P.A. Bobbert, J. Vlieger, 'Light scattering by a sphere on a substrate', Physica A **137**, 209 (1986).

[86] E.B. Treacy, 'Optical pulse compression with diffraction gratings', IEEE J. Quantum Electr. **5**, 454 (1969).

[87] M.B. van der Mark, *Propagation of light in disordered media: a search for Anderson localization* (PhD thesis, Universiteit van Amsterdam, 1990).

[88] C.D. Dushkin, H. Yoshimura and K. Nagayama, 'Nucleation and growth of two-dimensional colloidal crystals', Chem. Phys. Lett. **204**, 455 (1993).

[89] P.A. Kralchevsky, V.N Paunov, I.B. Ivanov and K. Nagayama, 'Cappilary meniscus interaction between colloidal particles attached to a liquid-fluid interface', J. Colloid Interface Sci. **151**, 79 (1992).

[90] N.D. Denkov, O.D. Velev, P.A. Kralchevsky, I.B. Ivanov, H. Yoshimura and K. Nagayama, 'Mechanism of formation of two-dimensional crystals from latex particles on substrates', Langmuir **8**, 3183 (1992).

Summary

The subject of this thesis concerns time-resolved spectroscopy on ultrashort time scales. The properties we consider in this thesis are the dynamics of an electron gas and the time resolved propagation of light through a disordered strongly scattering medium.

To be able to study the fore mentioned effects, one has to know how the light interacts with the system which is studied. This interaction is described by the response function of the system. In case of interferometers, one usually calls the response function the transfer function. This transfer function describes the scattering of light from the interferometer and is a complex valued function. In chapter 2 we discuss transfer functions from a general point of view. Transfer functions should obey a Kramers-Kronig relation, enabling one to calculate the real part form the imaginary part of the transfer function and vice versa. To see whether a Kramers-Kronig relation exist for a transfer function, it is sufficient for a transfer function to be analytic. In chapter 2 we study the analyticity of transfer functions of interferometers. It is shown that if one uses the Fourier-Laplace transform to calculate the transfer function in the frequency domain, the tranfer function is analytic and a Kramers-Kronig relation can be formulated. In the literature it was recognized that problems can occur if one tries to formulate Kramers-Kronig relations between amplitude and phase. We show that if we formulate the proper transfer function this transfer function obeys a modified amplitude-phase relation.

In chapter 3, we present a novel method to determine the full transfer function of a system, based on measuring the interferometric cross-correlation function between a pulse propagated through the system and an undistorted reference pulse. The method is demonstrated experimentally by measuring the complex-valued transfer function of an etalon in transmission. The experimentally obtained results are compared with the calculated transfer function and are found to be in excellent agreement. Furthermore we show that the time resolution of the method is about one order of magnitude better than the pulse duration of the pulses used in the experiments.

The extremely high time-resolution of the novel method makes it sufficient to study the time-resolved propagation through multiple scattering media as we describe in chapter 4. Important parameters which characterize the multiple scattering medium are the thickness of the medium L and the average

path length between two scattering events ℓ. The coefficient L/ℓ defines the optical thickness of the multiple scattering medium. An exact description of the propagation of light through these multiple scattering media is to difficult. Therefore, in this field it is customary to describe the transport of light through multiple scattering media with a diffusion equation, which is shown to be correct for optically thick media ($L/\ell >> 1$). For optically thin media it is expected that diffusion breaks down. Up to now optical experiments to study the time-resolved propagation through multiple scattering media in the visible regime of the electromagnetic spectrum have been performed for optically thick media ($L/\ell >> 1$), the reason being that no methods were available having time-resolution sufficient to study optically thin media. The novel method we introduced in chapter 3 has a time-resolution sufficient to study optically thin samples ($L/\ell \sim 1$). The experiments we performed mainly concern the question whether or not diffusion theory is also applicable for these optically thin media and we show that the diffusion approximation clearly breaks down for the dynamic measurements. We also performed stationary measurements. In these measurements the time integrated total transmission is recorded. Contrary to the dynamic measurements these results could be described with standard diffusion theory. We tried to interpret the experimentally obtained results with theory that goes beyond the diffusion description.

In chapter 5 we describe experiments performed to study the electronic relaxation processes in gold. Usually these type of experiments are performed using an optical pump-probe measurement. Commonly used theories to describe the relaxation dynamics of the electrons assumed that after excitation of electrons, electron-electron collisions maintain an equilibrium within the electron gas. However, strong evidence that this equilibrium was not established was obtained using pump-probe experiments. Due to the finite time-resolution of an optical pump-probe experiment, the initial relaxation processes, which is the interval where we expect to see large deviations from the equilibrium of the electron gas, are difficult to resolve. Using the new method we were able to study this time interval. Efficient excitation of electrons and sensitive detection of the changing reflectivity properties of the gold film were achieved by employing the surface-plasmon polariton resonance at the metal interface. Essential to be able to analyze this type of measurement is a consistent modelling of the influence of the excitation of hot electrons by the leading part of the pulse on the relectivity properties during the trailing part. We performed numerical calculations to model these phenomena, showing that due

to the nonthermal distribution of the electron gas the resonance frequency of the surface-plasmon polariton shifts. The experimentally obtained results did not show a convincing shift of the resonance.

In the final chapter we present measurements of the scattering properties of particles on a substrate. The particles we study have a diameter in the order of the wavelength of light. The scattering properties of these particles in a homogeneous surrounding are described by exact Mie theory. However, in a non-homogeneous surrounding no theory is available. There are two reasons to study the scattering properties of a particle near a surface. In the first place, the measurements clearly show that the scattering properties of light by a particle are influenced by its surrounding. A proper formulation of the scattering properties of a particle in a finite geometry may serve as an explanation for the break down of diffusion for thin samples as described in chapter 4. Due to the finite geometry a large influence on the scattering properties of the particles is expected. The other reason is the analogy with near field optics. The system of a particle near a surface is a system similar to a STM probe tip near a surface. We performed two types of experiments: a measurement on a single scatterer on a substrate and a measurement on a lattice of scatterers. The measurements showed strong deviations from Mie theory.

For further reading we refer to the following articles:

Chapter 2: Rik H.J. Kop, Pedro de Vries, Rudolf Sprik and Ad Lagendijk, Kramers-Kronig relations for an interferometer, Optics Communications **138**, page 118-129 (1997).

Chapter 3: Rik H.J. Kop and Rudolf Sprik, Phase-Sensitive interferometry with ultrashort optical pulses, Review of Scientific Instruments **66**, page 5459-5463 (1995).

Chapter 4: Rik H.J. Kop, Pedro de Vries, Rudolf Sprik and Ad Lagendijk, Observation of Anomalous Transport of Strongly Scattered Light in Thin Disordered Slabs, Physical Review Letters **79**, page 4369-4372 (1997).

Index

Dankwoord

Een wetenschapper is in de ogen van veel buitenstaanders een eenling die solitair te werk gaat, om zijn doel, dat alleen hij begrijpt, na te streven. Wetenschap is voor die mensen dan ook een solitaire bezigheid. Ik heb ruim vijf jaren deel uitgemaakt van het wetenschappelijke wereldje en kan zeggen dat die mensen een heel klein beetje gelijk hebben. Wetenschap is soms solitair. Op het moment van het uitvoeren van een experiment bijvoorbeeld is het zeer eenzaam. Alleen wachten, tot diep in de nacht en kijken of hetgeen dat je verwachte inderdaad het resultaat is. Maar zij hebben een klein beetje gelijk. Want veel belangrijker is dat wetenschap teamwork is. Vele mensen dragen bij aan het uiteindelijke resultaat. In directe of indirecte zin. In dit dankwoord wil ik al diegenen bedanken die direct of indirect bij hebben gedragen aan dit proefschrift.

Ik wil beginnen met het danken van mijn promotor Ad Lagendijk. Ik ben Ad veel dank verschuldigd voor het vertrouwen dat hij mij heeft gegeven om te mogen promoveren in zijn groep. Vervolgens wil ik mijn copromotor Rudolf Sprik bedanken. Ook Rudolf wil ik bedanken voor het vertrouwen in mij en verder voor de altijd weer nieuwe ideeen over hoe het verder moest als ik vast zat. Gerard Wegdam bedank ik omdat hij altijd bereid was om mijn problemen op wetenschappelijk gebied aan te horen. Daarop werd dan meestal geantwoord met een waterval aan ideen waar steevast “de es van ka” (ook wel $S(k)$) in voorkwam. Het was voor mij dan de kunst om daar het juiste uit op te pikken. Gerard bedankt voor de onuitputtelijke stroom van woorden.

Vervolgens wil ik de Turbo Boost van mijn promotie, Pedro de Vries, bedanken voor de enorme inbreng in de totstandkoming van mijn proefschrift. Pedro was mijn kamergenoot gedurende de laatste twee jaren van mijn promotie. Mede hierdoor, meer bovenal door de enorme gedrevenheid en nieuwsgierigheid heeft Pedro een enorme bijdrage geleverd aan twee hoofdstukken uit dit proefschrift.

In een brainstormsessie op de kamer van Ad heeft Bart van Tiggelen enorm geholpen door voor het bord gewapend met een stift een afleiding te geven van uitdrukking die onze resultaten een stap dichter bij het gewenste resultaat bracht. Bedankt daarvoor Bart.

Een onuitputtelijke bron van verfrissende ideeen, al dan niet wetenschappelijk, waren de leden van de groep. Johannes de Boer, Peter Den Outer, Ron Kroon, Mark Kroon, Jom Luiten, Mischa Megens, Allard Mosk, Pepijn Pinkse, Irwan Setija, Jaime Gomez Rivaz, Michiel Thijssen, Dirk Riese, Mark

van Rossum, Frank Schuurmans, Gijs van Soest, Willem Vos, Martijn Wubs, Judith Wijnhoven, alsmede 'lotgenoot' (Corsica) David van Coevorden, bedankt!!

Wim Koops is een hoofdstuk apart. Wim bedankt voor de steun op technisch gebied en de hand en spandiensten. Maar ook voor de steun, als ik het ergens moeilijk had dat meer valt samen te vatten als "wetenschap van het leven". Je was altijd weer een gewillig oor als ik het ergens over wilde hebben. Nogmaals bedankt.

Mijn ouders, mijn broers en zus wil ik bedanken voor hun begrip dat ik hen gevraagd heb. Pa en Ma ik weet dat het vaak niet altijd even simpel was, maar dit is het dan. Beter laat dan nooit!

Geerte, het is niet altijd van een leien dakje gegaan, maar zonder jou had ik de hoop allang opgegeven!

Rik